Development of New Approaches for Understanding and Optimizing Antisolvent Crystallization Processes

Corin Mack

Supervisor: Prof. Joop H. ter Horst

Prof. Jan Sefcik

EPSRC Future Manufacturing Research Hub in Continuous Manufacture and Crystallisation

Thesis submitted in satisfaction with the requirements of the Strathclyde Institute of Pharmacy and Biomedical Sciences at the University of Strathclyde for the Degree of Doctor of Philosophy.

April 2022

Declaration

I declare that the work in this thesis is entirely my own work and has not been submitted previously to this or any other university. There the work of others is utilized, this is acknowledged and cited in the proper manner.

Corin Mack

Date

Dedication

To everyone that helped me get to this to the finish line.

Acknowledgements

Firstly, I would like to thank Prof. Joop H. ter Horst for being an amazing supervisor. He helped and encouraged me to broaden my field of knowledge by trying out different aspects of the crystallisation field within the lab, while also helping me to focus in and get the most out of my work; I know it was not easy but we got there! It was a pleasure to socialise with yourself and share the field at weekly 5-a-side's (no matter which side we are on). I would also like to thank you for helping me with starting my career in the pharmaceutical industry, spending the time to look over my presentation and giving me some hints and tips.

I would also like to thank Prof. Jan Sefcik for his in-depth discussions and input from the regular meetings. It was always enlightening to discuss different aspects that had not been thought of and to get your valuable input from the beginning.

I would also like to extend a special thank you to Johannes Hoffmann and Dr. Lennart Ramakers PhD. During my masters they were a massive help to understand and learn what was going on and how best to proceed. In doing so helping to me to produce a good piece of work and obtain the requirements for my PhD with Joop. This help continued during my PhD and was an incredible during my first year. As well as this you were always up for post-work drinks which sometimes was a god send.

There are far too many people to name but I would like to say a massive thank you to everyone within CMAC over the last four years. All the laughs and discussions we had in the lab and the offices helped me both with my work and on a social aspect. Especially those late night Exploding Kitten games….excellent find by Russell Miller.

I would also like to thank my flatmate and friend Michael Miller. Honestly, I can't say enough! Between helping with my job interview, to reviewing work for me, to the pub nights celebrating whatever was the flavour that week. There really are far too many instances to name. Thank You!!

Finally I'd like to thank my family, and especially mum. You helped me to keep going, supplying nice food along the way. I really cannot repay you enough for everything you guys have done for me throughout the years to get to this point both professionally and personally.

List of Publications

1. Febra SA, Bernet T, **Mack C**, et al. Extending the SAFT-γ Mie approach to model benzoic acid, diphenylamine, and mefenamic acid: Solubility prediction and experimental measurement. *Fluid Phase Equilib*. 2021;540:113002. doi:10.1016/j.fluid.2021.113002.
2. **Mack C**, Hoffmann J, Sefcik J, ter Horst J.H. Accurate Phase Diagrams for the Basic Design of Antisolvent Crystallization Processes. Crystal Growth and Design (*In preparation*)
3. **Mack C**, Sefcik J, ter Horst J.H. Activity Coefficients in Phase Diagrams for Antisolvent Crystallization. (*In preparation*)

Abstract

As more and more complex molecules find their way to the market, alongside the increasing demand for pharmaceuticals, the need for development and improvement of key process steps is crucial. By reducing the time and amount of drug substance used up during each phase in the crystallisation development process, pharmaceuticals can be delivered to patients faster. To achieve our aim, three contributions have been made, looking at both single and multicomponent systems for solvent selection protocols alongside the development and application of a model equation to accurately describe antisolvent phase diagrams. Initially solubility and activity coefficient models were applied to different solute-solvent systems. In doing so, both the Margules and Wilson models showed accurate modelling capability with the experimental activity coefficients. Due to the parameters of the Wilson model, interactions between the solute-solvent molecules can be quantified. This information about molecular interaction from specific functional groups, allow solvent selection protocols to be engineered towards specific solvent systems. From the investigation of single solvent systems, antisolvent systems were investigated. By using compounds like those observed in industry such as salts and highly hydrophobic compounds, coupled with a temperature variation method, a generic model equation was developed encompassing the general trend observed by antisolvent phase diagrams systems for both synergistic and non-synergistic systems. This model allowed the prediction and optimization of key process characteristics such as yield and productivity at different temperature and antisolvent fractions, so identifying specific antisolvent fractions and temperatures where processes provide the most optimal results. The final contribution integrates the previous observations and techniques, revealing how well the Wilson model can describe antisolvent phase diagrams, while providing insight into the molecular interactions that dictate synergistic antisolvent phase diagrams. Although the multicomponent Wilson model was not able to describe synergistic relationships, the binary model was able to describe the systems at individual antisolvent fractions. From the binary equation, the interaction parameters at individual

antisolvent fractions showed variation in non-ideality as the antisolvent fraction increases, identifying that the interaction parameters between the solute-solvent-antisolvent required are not static and change as the component content changes. From these variations, interpretations of how antisolvent phase diagrams behave is established with regards to molecular interactions occurring with the systems. From each of these contributions, an aspect of crystallization processes was encompassed, identifying either different strategies or developing methodologies which can help reduce the need for time-consuming studies. In doing so allowing a greater pace for getting drugs to patients

Table of Contents

List of Figures

List of Tables

Nomenclature

μ_i	Chemical potential of a species
μ_i^0	Chemical potential of an ideal systems
$\Delta\mu$	The difference in chemical potential between two different states
T	temperature
R	Gas constant
f_i	Fugacity of a species
f_i^0	Fugacity at an ideal system
a	activity
x	Mol fraction
x^{id}	Ideal mol fraction
γ	Activity coefficient
P	Pressure
P_{tp}	Pressure at the triple-point
ΔH_{tp}	Heat of fusion at the triple point
T_{tp}	Temperature at the triple point
ΔC_p	Specific heat capacity
V_m	Molecular volume
ΔH_f	Heat of fusion
ΔS_f	Entropy of fusion
ΔH_d	Heat of dissolution
ΔS_d	Entropy of dissolution
T_m	Melting temperature of a substance
K_a	Reaction constant
λ	Buchowski-Ksaizaczak constant for self -association of solutes
h	Buchowski-Ksaizaczak constant for the enthalpy of dissolution for a system

V_i^L	Molecular volume for a subcooled liquid solute
δ	Solubility parameter
ϕ	Volume fraction
Δu	Enthalpy of vaporization
v	Molar volume of a specific component
V^E	Excess volume
H^E	Excess enthalpy
S^E	Excess entropy
G^E	Excess free energy
G	Free energy
G^{id}	Free energy of a component at an ideal state
ΔG_{mix}	Free energy of mixing
A_{21}/A_{12}	Adjustable parameters
i,j	Subscript defining a specific component
$n_{i,j}$	Number of molecules of a specific component surrounding a specific component
$N_{i,j}$	Total number of molecules of a specific component
Ω	Weighting factor
$\Lambda_{ij}/\Lambda_{ji}$	Interaction parameter between unlike molecules
$\lambda_{ij}/\lambda_{ji}$	Interaction energy parameters between two dissimilar molecules
S	Supersaturation
C	concentration
c*	Solubility
x_{AS}	Antisolvent mass fraction
θ	Angle of diffraction
$\lambda_{\text{x-ray}}$	Wavelength of x-rays used for XRPD
d	Distance between crystal layers

m	mass
M	Molar mass
A/B	Van't Hoff adjustable parameters
C/D	Van Laar adjustable parameters
σ	Relative standard deviation
x^{pred}	Predicted mol fraction from
CV	Coefficient of variation
$SD_{\Delta Hf}$	Standard deviations for the heat of fusion
F_s	Feed of the saturated solution
F_{AS}	Feed of the antisolvent
F_p	Feed of the product
P	Productivity
L	Loss
ρ_{Slurry}	Slurry density
Y	Yield
τ	Residence time
V	Volume
$x_{AS,mol}$	Mole fraction of the antisolvent presence

Chapter 1: Introduction

The development of new pharmaceutical products is a very time consuming and costly venture to undertake, accompanied by a low probability of success. In recent years, the average cost of bringing a drug to the market is close to $1 billion[1]. More than 40% of all new chemical entities are practically insoluble[2]. The solubility of a drug is one of the major factors dictating its possible bioavailability, as it is one the important parameters for delivering the API (active pharmaceutical ingredient) to the patient at the required blood concentration level[2].

In the later stages of process development, the solubility of the drug candidate is required to determine the optimal processes for purification, washing and formulation. The drug candidate is screened in several solvent types (polar, non-polar, apolar protic) to determine the best solvent or solvent mixture. In many cases, the solvent choice is not just based on solubility but also on other critical attributes and guidelines. Toxicity is a major factor influencing the use of specific solvents, with the ICH guidelines[3] outlining the amount of residual solvent that is allowed to remain in a API post isolation. As solvents have no therapeutic benefit to patients, it is advised residual solvents are minimised. Within industry, Class 2 or 3 solvents are ideal as they exhibit the highest tolerance levels with class 1 solvents to be avoided at all costs unless proper justification is provided[3].

A schematic of different crystallization process types is provided in Figure 1-1. Different process types are based on the solubility of the drug candidate. Systems with good solubility and a high temperature dependence are ideal candidates for cooling or antisolvent crystallisation. If no temperature dependence is observed evaporative crystallisation, is the preferred route. Crystallisation of a poorly soluble drug candidate is preferably done by utilising precipitation crystallization. Melt crystallization is used for the ultra purification of a compound to achieve purities of up to 99.999%. In providing highly pure material, compounds are melted and crystallized. This differs from the other methods of crystallization which is commonly a one-cycle process. Due to the

energy requirements if this process it is only utilised when ultra purification is required[4].

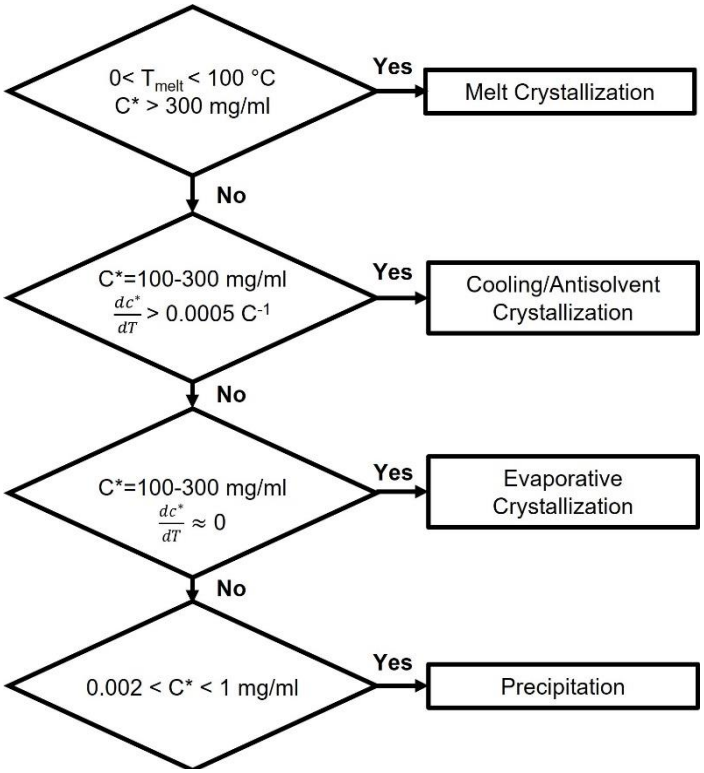

Figure 1-1: Diagram for the selection of crystallization methods based off solubility[5].

The emergence of computational methods for solubility modelling such as SAFT[6] and COSMO-RS[7,8] have enabled solvent screenings to be performed at a much smaller scale. By utilising group contribution methods, they can obtain solubilities in large number of solvents without having to measure them individually. Although they require some experimental data to obtain interaction parameters between functional groups.

1.1 Solubility

Within the pharmaceutical industry, virtually all crystallization processes involve solutions, with the properties of these solution dictating the development, design and control of these processes. A solution is a mixture of two or more components in a homogeneous form: solid, liquid or gas. Typically, solutions consist of different combinations of solids and liquids, with crystallization being the optimal technique utilised in order to separate both constituents, in doing so

obtaining a pure form of either component. Solubility is the term given to the maximum amount of a solute able to be dissolved in a specific solvent or solvent mixture in order to make a saturated solution, at a specific temperature and pressure.

1.1.1. Fugacity, ideal Solubility and Activity Coefficient

For a solution to be saturated, its solid and liquid phases must be in equilibrium with one another, therefore the chemical potential μ of the solute in the solid phase is the same as that of the liquid phase:

$$\mu_{i,solid} = \mu_{i,liquid} \qquad 1$$

The chemical potential of a substance is related to its activity by:

$$\mu_i(T) = \mu_i^0 + RT\ln\left(\frac{f_i}{f_i^0}\right) \qquad 2$$

With μ_i^0 and f_i^0 representing the chemical potential and fugacity of an ideal system.

So:

$$\mu_i - \mu_i^0 = RTln\left(\frac{f_i}{f_i^0}\right) \qquad 3$$

The activity of a substance can also be referred from the thermodynamic function fugacity f where:

$$a_i = \frac{f^i}{f^0} \qquad 4$$

Using equation 3 provides a more convenient method to describe the solubility of an organic solute in various solvents. Fugacity is the "corrected pressure" and reduces to this pressure when the solution is ideal, with this pressure coming from the relationship with temperature to the triple point between solid, liquid and gas phases. An ideal system exists when there are no interactions between the components and so the system behaves as would be expected from the equations of state.

For phases in equilibrium:

$$f_{i,solid} = f_{i,solution} \quad (5)$$

Equation 5 can then be written to the form for the solid $f_{2,solid}$:

$$f_{2,solid} = \gamma_2 x_2 f_2^0 \quad (6)$$

Or

$$x_2 = \frac{f_{2,solid}}{\gamma_2 f_2^0} \quad (7)$$

Where γ_2 is the activity coefficient of the solid at a specific mole fraction x_2 at standard state fugacity f_2^0. Equation 7 is the general equation for the solubility of a solute in a solvent, with its magnitude dependent on the activity coefficient and the fugacity ratio. The standard state fugacity is the fugacity of a pure solid in a sub-cooled liquid state. So by assuming that both the solid and sub cooled liquid have vapour pressures and that each component is chemically similar so having a $\gamma_2 = 1$, Equation 7 can be written into the form:

$$x_2 = \frac{P^s_{2,Solid\ Solute}}{P^s_{2,subcooled\ liquid\ solute}} \quad (8)$$

From Equation 8, as the only components influencing the ideal solubility is the tendency of the solute to go from one phase to another with no other influences such as the choice of solvent. It also shows that structural differences in the pure components will alter the ideal solubility.

The general equation for the fugacity ratio is[9]:

$$\ln\left(\frac{f_2}{f_{2,subcooled\ liquid\ solute}}\right) = \frac{\Delta H_{tp}}{R}\left(\frac{1}{T_{tp}} - \frac{1}{T}\right) - \frac{\Delta C_p}{R}\left(\ln\frac{T_{tp}}{T} - \frac{T_{tp}}{T} + 1\right) - \frac{\Delta V}{RT}(P - P_{tp}) \quad (9)$$

Where ΔH_{tp} represents the enthalpy change from the state change at the triple point temperature T_{tp}, with the change in heat capacity and volume between these two phases represented by ΔC_p and ΔV respectively. R, T and P represent the universal gas constant, temperature and pressure. As the triple point temperature and so enthalpy change at this temperature are unknown in most cases, these terms are replaced with the heat of fusion ΔH_f and melting point T_m of the substance. By substituting Equation 9 into Equation 7, the most general

form of the solubility equation is produced, often referred to as the Hildebrand equation:

$$x_2 = \frac{1}{\gamma_2}\exp\left(\frac{\Delta H_f}{R}\left(\frac{1}{T_m}-\frac{1}{T}\right)-\frac{\Delta C_p}{R}\left(\ln\frac{T_m}{T}-\frac{T_m}{T}+1\right)-\frac{\Delta V}{RT}(P-P_m)\right) \quad 10$$

In most situation, the heat capacity and pressure terms are dropped due to being negligible in magnitude to the enthalpy of fusion leaving:

$$x_2 = \frac{1}{\gamma_2}\exp\left(\frac{\Delta H_f}{R}\left(\frac{1}{T_m}-\frac{1}{T}\right)\right) \quad 11$$

1.2 Solubility Correlation Modelling

1.2.1 Van 't Hoff

The equilibrium constant K is a value at which after a certain time elapsed, no further change of a systems state is expected at a given tempetrure or pressure. It is related to the rate of the forward and backward reactions towards reaching equilibria. It is described by the equation[10]:

$$K = \frac{[Products]}{[Reactants]} \quad 12$$

Where the [Products] and [Reactants] relate to the concentration of the product and reactants at equilibrium at a specific temperature. There is an infinite amount of equilibrium constants possible but only one at a given temperature[10]. The van't Hoff equation relates the change in equilibrium constant of a system when undergoing a change in state (solid to liquid) due to temperature T. In many cases, the van 't Hoff equation is written as Equation 13, as it assumes that $\gamma_2 = 1$:

$$\ln x = \frac{\Delta H_f}{R}\left(\frac{1}{T_m}-\frac{1}{T}\right) \quad 13$$

Where x is the mole fraction of the solute, with a heat of fusion ΔH_f in J/mol and melting temperature T_m, dissolved in the solvent at a specific temperature T.

A fit of $\ln x$ vs $\frac{1}{T}$ would give a linear fit in the form:

$$\ln x = m\frac{1}{T} + c \qquad 14$$

With its slope m describing the change in enthalpy of the system across all temperatures $\frac{\Delta H_f}{R}$ and the intercept c describing the change in molar entropy across that same temperature range $\frac{\Delta S_f}{R}$. In most cases, systems do not exhibit an ideal behavior and so $\gamma_2 \neq 1$ and the enthalpy ΔH_d and entropy ΔS_d of dissolution must be taken into account using:

$$\ln x = -\frac{\Delta H_d}{RT} + \frac{\Delta S_d}{R} \qquad 15$$

1.2.2 Apelblat Equation

The Apelblat equation is an effective thermodynamic model for correlating and extrapolating experimental solubility:

$$\ln x = a + \frac{b}{T} + c\ln(T) \qquad 16$$

With the empirical constants a and b accounting for the effect of the enthalpy of dissolution on the mole fraction, and c accounting for differences in heat capacity of the solid and liquefied solute at the solution temperature T.

1.2.3 Buchowski-Ksaizaczak Equation

Buchowski proposed another two-parameter model as an extension to the Van't Hoff equation to extrapolate experimental solubility data at specific temperatures:

$$\ln\left(1 + \frac{\lambda(1-x)}{x}\right) = \lambda h\left(\frac{1}{T} - \frac{1}{T_m}\right) \qquad 17$$

From equation 17, the parameters λ and h are obtained from the regression of experimental data, with λ referring to the self-association of solute molecules within a specific system and h detailing the enthalpy of dissolution for the system. Buchowski stated that deviations from λ = 1 signify the non-ideal behaviour of a system, the model accounts for the different molecular interactions and their resulting energies associated with mixing process during the dissolution process at specific temperature T.

The application of these models is widely carried out within the literature[11–14], for both single solvent and mixed solvent systems, with the equations providing good agreement with the experimental data.

1.3 Activity Coefficient Modelling

1.3.1 Raoult's Law and its expression with Activity Coefficients

Raoult's law relates the partial pressure of a component with the mole fraction of that component assuming an ideal system. This assumption in Raoult's law means that the intermolecular forces acting between dissimilar molecules is the same as those acting on like molecules. For systems that have identical physical properties this holds true, with even similar components behaving similarly as described by Raoult's Law. Although for gas systems Raoult's law holds true due to the low interaction between gas molecules, in liquid systems interactions between molecules are strong. These strong interactions give rise to either positive or negative deviations from ideality and so Raoult's law. Negative deviations are consistent with strong interactions between dissimilar molecules whereas positive deviations are consistent with weak interactions between dissimilar molecules and the more interactions between like molecules dominate.

Due to these interactions between molecules causing non-ideal behaviours, a modified Raoult's law was introduced utilising activity coefficients γ[15]:

$$y_i P = x_i \gamma_i P_i^{sat} \qquad 18$$

Where P_i^{sat} is the pressure at the saturation temperaure and y_i and x_i represent the mole fraction of the component in the vapour and liquid phase respectively. Activity coefficients provide a way of relating the non-ideal behaviours of a system observed experimentally back to the ideal nature as outlined by Raoult's Law, so providing a way to identify what interactions are occurring within a system. When $\gamma = 1$ there are no deviations from ideality and so observe Raoult's Law. When negative deviations from Raoult's law are observed, $\gamma < 1$ and the reciprocal is observed for positive deviations[15].

1.3.2 Regular Solution Theory

Unlike in electrolyte systems, solute-solvent interactions are due to dispersion, electrostatic (polarity) and chemical forces (hydrogen bonding) acting on the molecules. Organic solutes and solvents are classed as either polar or non-polar, although within these there are ranges of polarity. It is these interaction between solute-solvent molecules which produce non-ideality in a system where $\gamma \neq 1$. For a system a when $\gamma < 1$, polar interactions are dominating between dissimilar molecules according to Raoult's Law which results in higher solubilities than ideal. The opposite can be said for non-polar or polar-non-polar systems where $\gamma \geq 1$ as they do not tend to have as strong interactions compared to the hydrogen bonding of polar systems, so exhibiting solubilities close to or lower than ideal.

A common way of predicting activity coefficients is from regular solution theory:

$$\ln \gamma_i = \frac{V_i^L(\delta_j - \delta_i)^2 \phi_j^2}{RT} \qquad 19$$

Where V_i^L and δ_i represent the molar volume and solubility parameter for a subcooled liquid solute. δ_j and ϕ_j represent the solvents solubility parameter and volume fraction respectively, with defined as:

$$\phi_j = \frac{x_j V_j^L}{x_j V_j^L + x_i V_i^L} \qquad 20$$

The solubility parameters for each component are defined from the relationship:

$$\delta_i = \left(\frac{\Delta u_i}{v_i}\right)^{\frac{1}{2}} \qquad 21$$

$$\delta_j = \left(\frac{\Delta u_j}{v_j}\right)^{\frac{1}{2}} \qquad 22$$

Where Δu represents the enthalpy of vaporization for component *i* or *j*, with a molar volume *v*.

Although common, regular solution theory does not work well when predicting systems, which are experiencing polar interactions. As the method was

developed to describe systems with no excess entropy, change in volume on mixing or a non-zero enthalpy, it always predicts systems to have a $\gamma > 1$.

1.3.3 Excess Gibbs Free Energy

The deviation of a property from its ideal solution value is regarded as the excess property. Generically the excess property is written using the symbol M^E where M corresponds to the property in question, written in the form:

$$M^E = M - M^{is} = M - \sum_i x_i M_i \qquad 23$$

Where M and M^{is} represent the measured and ideal value of the property respectively, and the combination $x_i M_i$ relates to the partial molar value.

Properties looked at in terms of deviation from ideality are volume V^E, enthalpy H^E and entropy S^E, with Gibbs free energy G^E being accessible through:

$$G^E = H^E - TS^E \qquad 24$$

Where T corresponds to the temperature in Kelvin. It can also be calculated similarly from Equation 24 although in this case, the partial molar Gibbs energies are considered to be the chemical potential of the system:

$$\begin{aligned} G^E = G - G^{is} &= \left(G - \sum_i x_i G_i\right) - \left(G^{is} - \sum_i x_i G_i\right) \\ &= \Delta G_{mix} - RT \sum_i x_i \ln x_i \end{aligned} \qquad 25$$

Where ΔG_{mix} is the free energy of mixing. By incorporating Equation 6 and 7 the free energy of mixing is related to the activity coefficient in the form:

$$\Delta G_{mix} = RT \sum_i x_i \ln(x_i \gamma_i) \qquad 26$$

Incorporating this into Equation 25 yields excess free energy equation relating it directly to activity coefficients:

$$G^E = RT \sum_i x_i \ln(\gamma_i) \qquad 27$$

From Equation 27, it is noted that when the activity of a system is ideal, there is no excess free energy.

1.3.3.1 Margules

Many Gibbs free energy models can be rewritten into the form:

$$\frac{G^E}{RT} = x_1 x_2 (B_{12} + C_{12}(x_1 - x_2) + D_{12}(x_1 - x_2)^2 + \cdots) \qquad 28$$

Where G^E is the excess free energy observed between the mixing of two components of mole fraction x_1 and x_2 respectively. The Margules equation has a one-parameter and two-parameter model although the one-parameter model insufficiently estimates activity coefficients across the whole composition range. The two-parameter was designed to adjust the magnitude and skewness of the predictions towards the experimental data.

The two-parameter Margules model[16] is a simplified version of Equation 28:

$$\frac{G^E}{RT} = x_1 x_2 (A_{21} x_1 + A_{12} x_2) \qquad 29$$

Where $A_{21} = B_{12} + C_{12}$ and $A_{12} = B_{12} + C_{12}$ and $D_{12} = 0$. When activity coefficients are inserted into Equation 17 with mathematical regression the two-parameter Margules equation is obtained to describe activity coefficients of the components in a system:

$$\ln y_1 = x_2^2 (A_{12} + 2(A_{21} - A_{12}) x_1) \qquad 30$$

$$\ln y_2 = x_1^2 (A_{21} + 2(A_{12} - A_{21}) x_2) \qquad 31$$

Where A_{12} and A_{21} are the adjustable parameters obtained from fitting Equation 30 and 31 to experimental data.

1.3.3.2 Van Laar

From the work of Van der Waals equation of state, Van Laar found that the parameters were not accurate enough in predicting excess energy in mixing, and so requiring empirical data to properly predict the activity of a system[17]. He simplified the equation by defining an arbitrary parameter to represent the final term in the equation, as well as rearranging to obtain only two adjustable parameters:

$$\frac{G^E}{RT} = \frac{A_{12}A_{21}x_1x_2}{(x_1A_{12} + x_2A_{21})} \quad 32$$

A_{12} and A_{21} represent the adjustable parameters to describe interaction between the dissimilar molecules present. By differentiating Equation 16 and using the product rule, the following equations give expressions for the van Laar equation describing activity coefficients:

$$\ln \gamma_1 = \frac{A_{12}}{\left(1 + \frac{A_{12}x_1}{A_{21}x_2}\right)^2} \quad 33$$

$$\ln \gamma_2 = \frac{A_{21}}{\left(1 + \frac{A_{21}x_2}{A_{12}x_1}\right)^2} \quad 34$$

Where γ_i represents the activity coefficient for each component. The adjustable parameters can be obtained by fitting the equation to a range of values at different temperatures.

1.3.4 Local Composition Theory

A major assumption of regular solution theory is that there are no interactions between the molecules in the solution. Although in some cases, the interaction of molecules in a mixture is strongly correlated to the mixture composition. In these instances, the idea of local compositions of molecules grouped together can vary significantly from that of the bulk composition. Specific interactions, like that of hydrogen bonding between two molecules and polarity similarities, can lead to the occurrence of local compositions forming within a bulk and so breaking down the quadratic mixing rules due to energetic interactions leading to non-randomness between the molecules in the bulk . Because of the lack of ability to measure the local composition of molecules within systems, as opposed to that of the bulk compositions, the theory is purely a mental concept, which somewhat arbitrary assumes similarities between local compositions to that of bulk compositions[18]. The local compositions within systems cannot be accurately measured and defined, therefore disagreements within the literature remain.

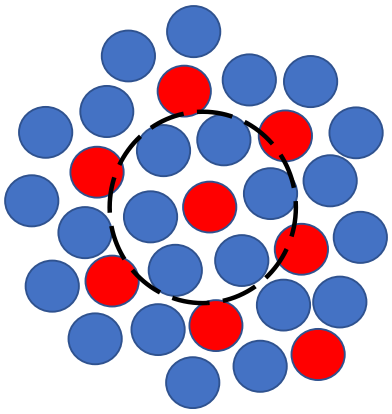

Figure 1-2: Visual representation of the local composition of molecules around a central molecule (red).

Considering a binary mixture with molecules A and B, we can define the local composition of the molecules immediately surrounding A:

$$x_{BA} = \frac{n_B}{N_A} \qquad 35$$

$$x_{AA} = \frac{n_A}{N_A} \qquad 36$$

With n_A and n_B being the number of A and B molecules around A respectively, and N_A the total number of molecules around A.

With the local mole balance being that:

$$x_{AA} + x_{BA} = 1 \qquad 37$$

It can be assumed that there is some weighting factor Ω relative to the overall compositions within the system:

$$\frac{x_{BA}}{x_{AA}} = \frac{x_B}{x_A}\Omega_{BA} \qquad 38$$

With $\Omega_{BA} = 1$ meaning that's the solution is random.

By rearranging equation 36 and substituting it into 35:

$$x_{AA}\left(1 + \frac{x_B}{x_A}\Omega_{BA}\right) = 1 \qquad 39$$

This equation is rearranged to give an expression for x_{AA} and subbed into a previously arranged form to obtain an expression for the local composition of molecules around A:

$$x_{BA} = \frac{x_B \Omega_{BA}}{x_A + x_B \Omega_{BA}} \qquad 40$$

A similar method can be used to obtain an expression for the surrounding A molecules around the central molecule B x_{AB}:

$$x_{AB} = \frac{x_A \Omega_{AB}}{x_B + x_A \Omega_{AB}} \qquad 41$$

1.3.5 Wilson Equation

1.3.5.1 Binary Equation

Following on from the work of Flory-Higgins, Wilson proposed the following binary equation to describe activity coefficients, accounting for the differences in both molecular size and intermolecular forces between molecules[16]:

$$ln\,\gamma_j = -ln(x_j + \Lambda_{ji} x_i) - x_i \left(\frac{\Lambda_{ij}}{x_i + \Lambda_{ij} x_j} - \frac{\Lambda_{ji}}{x_j + \Lambda_{ji} x_i} \right) \qquad 42$$

Where the subscripts *i* and *j* represent two different types of molecules with the system. Λ_{ij} and Λ_{ji} represent the interaction parameter between unlike molecules and can be further defined through:

$$\Lambda_{ij} = \frac{v_j}{v_i} exp\left(-\frac{\lambda_{ij} - \lambda_{ii}}{RT} \right) \qquad 43$$

$$\Lambda_{ji} = \frac{v_i}{v_j} exp\left(-\frac{\lambda_{ji} - \lambda_{jj}}{RT} \right) \qquad 44$$

With λ_{ij} and its reciprocal λ_{ji} representing the constant interaction energies between two unlike molecules within a system, along with R and T representing the molar gas constant and temperature (K) respectively. There are studies that show slight deviation in λ_{ij} and λ_{ji} due to temperature variations although general practice has shown these variations are neglected due to the variations being small in comparison to the effect of temperature of the exponential terms in equation 43 and 44.

In terms of separation process design, whether in the petrochemical or pharmaceutical industry, the binary Wilson equation has been widely

applied[15,19,20]. The interaction energy constants are used for process separation design stages, with these interaction parameters stored in the databases like the Dortmund Database. Within the crystallization space, Wilsons equation is regularly applied for solubility study on a specific API within certain solvents, with the interaction parameters between the API and solvent determined along with the predicted mole fraction *x* from the Wilson equation. This is correlated against the experimental mole fractions to interpret the accuracy of the interaction parameters and the accuracy of the data to thermodynamic principles. Although what is not commonly interpreted further is the quantitative value of the interaction parameters, with other means such as solvation theory applied instead. Utilising Raoult's law, $\Lambda_{ij} < 1$ signified a positive (+ve) deviation from Raoult's law and so inferring that there was strong interaction between like molecules within a system. Whereas $\Lambda_{ij} > 1$ identified that interaction between unlike molecules from such forces as hydrogen bonding through a negative (–ve) deviation from Raoult's Law[16]. VLE data with the Wilson equation has been used to predict the water activity in foodstuffs as a function of moisture content. In doing so, it showed good ability to predict the phase equilibria, while also noting the interaction parameters obtained from them can be used to give insight into the molecular interactions of sugars and water[14].

1.3.5.2 Multicomponent Equation

Wilson also presented a multicomponent equation, containing obtainable interaction parameters up to the number of components in the system *N*.

$$\ln \gamma_k = 1 - \ln\left(\sum_{j=1}^{N} x_j \Lambda_{kj}\right) - \sum_{i=1}^{N}\left(\frac{x_i \Lambda_{ik}}{\sum_{j=1}^{N} x_j \Lambda_{ij}}\right) \qquad 45$$

Wilson neglected ternary interaction parameters instead assuming a pseudo-binary mixture. The application of the multicomponent equation in predicting isothermal VLE data for both three- and four-component systems showed good results for systems containing aliphatic, aromatic and cyclic hydrocarbons and a polar solvent[20]. Although the model has not been applied to solute-solvent-solvent a modified version has been applied to polymer-polymer aqueous two-

phase liquid systems finding it to be reliable for the correlation of LLE phase diagrams with different polymer molecular weights[21].

1.4 Crystallization

Crystallization is a separation and purification technique, used to obtain highly pure crystalline material from a homogeneous mixture of two or more species. Crystallization is the most common technique utilized within the fine chemical industry for post synthesis product removal and purification. Due to the importance of particle properties on both downstream processing and performance criteria, it is also used for particle engineering purposes. The most common method of crystallization is by temperature modulation, where the temperature of a crystallizing system is slowly altered to obtain crystals of desirable qualities. This method is widely applied to both academic and industrial scenarios due to the strong control that can be maintained on the crystallizing system.

1.4.1 Driving force of Crystallization

For any system, a state of equilibrium is met when the Gibbs free energy is at its lowest. For crystallization, the driving force is described as the difference in chemical potentials between a solution and that of the corresponding solution in a saturated state. In a state of equilibrium, a crystallizing solution is in a saturated state and is described by the following:

$$\mu_{liquid,eq} = \mu_{solid} \qquad 46$$

Where $\mu_{liquid,eq}$ and μ_{solid} denote the chemical potentials of the crystallizing compound in the solution and the solid respectively. From a state of equilibrium, when a system experiences an external force that changes its conditions, whether it be from temperature, pressure or the addition of another chemical species such as another solvent, a change in chemical potential also occurs. This change in chemical potential is described by the following equation

$$\Delta\mu = \mu_{liquid} - \mu_{liquid,eq} = \mu_{liquid} - \mu_{solid} \qquad 47$$

Where the chemical potential of the crystallizing solution is now larger than that of the equilibrium state. This difference in chemical potential between the two

states is regarded as supersaturation, which represents the thermodynamic driving force for crystallization.

When there is a positive difference between these two states crystallization is thermodynamically feasible. When a solution has a negative chemical potential, the system is regarded as undersaturated where dissolution from a solid to a liquid phase is likely to occur.

The chemical potential of a system μ and that of its saturated state μ_{eq} can be described by Equation 2 where:

$$\mu = \mu_0 + RTln(a) \qquad 48$$

$$\mu_{eq} = \mu_0 + RTln(a_{eq}) \qquad 49$$

Where μ_0 is the standard potential, a and a_{eq} is the activity of the crystallising solution and the activity of the corresponding solution at its saturated state respectively. R and T refer to the universal gas constant and temperature respectively.

Both equations can be combined to express the dimensionless driving force for a neutral solute:

$$\Delta\mu = RT\ln\left(\frac{a}{a_{eq}}\right) = RTlnS \qquad 50$$

Where C and c_{eq} represent the concentration and equilibrium concentration of the solute in the system. S represents the supersaturation of the system, with the supersaturation being the driving force of crystallization.

1.5 Polymorphism

Polymorphism is defined to as the ability of a compound to crystallize in more than one distinct crystal species. Polymorphism can exist in a number of states[22]: Amorphous[23], true polymorphs, solvates and hydrates (pseudo-polymorphs) and salts[24]. Pure polymorphs make up nearly half of all known polymorphs, with the next being solvates[22].

True polymorphs are compounds which exhibit long range order (LRO) although differ in their packing arrangements within the crystal lattice, with no other

chemical entities present[25]. Polymorphs exhibit different physiochemical properties between one another such as solubility and bioavailability. This difference in solubility plays an important role in pharmaceutical products, as it is directly related to the bioavailability of the API. A prime example of this is Ritonavir, which a more stable and less soluble polymorphic form appeared, and it was no longer possible to manufacture the original product. Therefore, it had to be recalled and reformulated for this new stable form at elevated cost and time[26].

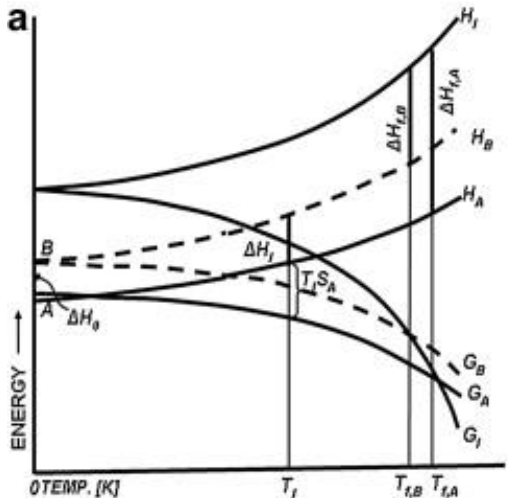

Figure 1-3: Energy/temperature diagrams of a monotropic system[27].

The Gibbs free energy of formation *G* for a polymorph is a measure of their stability, with the polymorph with the lowest energy considered the most stable with the lowest solubility at specific temperature as shown from G_A from Figure 1-3. Polymorphs with higher free energies G_B and enthalpy of formation H_B are metastable and exhibit higher solubilities. Transformation of the metastable to the stable form is thermodynamically possible as nature tends towards the lowest free energy of a system, although kinetic factors affect how quickly this transformation will take place. Solvents are well known to aid the transformation to the stable polymorph through solution-mediated transformation[28,29]. Controlling the nucleation of polymorphs has been widely researched due to industrial significance. Single and mixed solvent systems[30] as well as additives[31] have been utilised to promote the nucleation of a specific polymorph. Concomitant nucleation of polymorphs is a common problem with the solubilities

of either polymorph so close to one another they simultaneously nucleate[32]. Much research has been undertaken on these types of systems due to their complexity and possible burden within an industrial enviroment[13,33,34]. Computational methods have been utilised in order to investigate and predict the nucleation of systems where concomitant nucleation is observed. Such work found that the interfacial energy is a major factor when studying concomitant nucleation and devised an approach to predict the overall interfacial energy between clusters and the solution[35].

1.6 Cooling Crystallization

Due to the high temperature dependence of many compounds, the application of cooling crystallization as a separation procedure of a solute is the most common. As tight temperature control is easily achievable, controlling the supersaturation generated by the cooling is also easy. Due to the extremely common occurrence of systems which high temperature-dependence, a standard 'rule of thumb' was established by Black[36] who concluded that for every 10 °C increase in temperature, the solubility of a substance doubles. The nucleation of metastable polymorphs is more likely to occur in systems where poor control is been implemented, especially when both stable and metastable polymorphs known to crystallise concomitantly within very small temperature ranges[32,33]. As well as polymorph control, the control of particle attributes is possible through seeding procedures with good cooling crystallization control[37]. As primary nucleation occurs at higher supersaturations and is stochastic in nature, small particles will nucleate while larger crystals continue to grow. Therefore, the size distributions of a crystallization process reliant on primary nucleation is not reproducible between batches, resulting in large particle size distributions in the final product. Therefore, using seeding procedures with strong control avoids unwanted primary nucleation, with desupersaturation coming from secondary nucleation and subsequent growth of particles. Unlike primary nucleation, secondary nucleation occurs from the attrition of seed crystals generating other crystals which subsequently grow. Therefore the appearance of unwanted polymorphs is significantly reduced as well as stronger size control of crystals is possible.

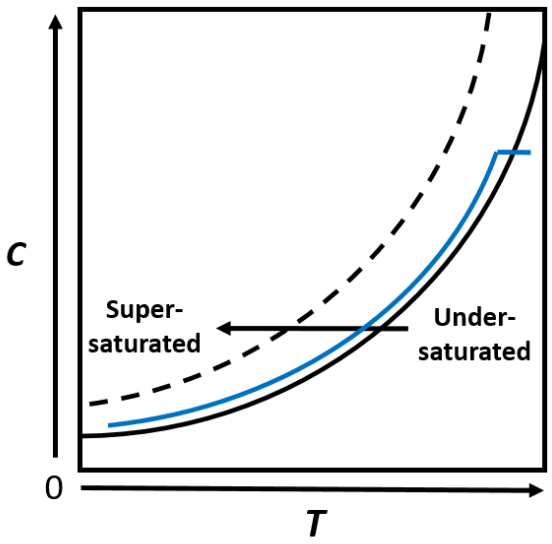

Figure 1-4: Typical representation of a cooling crystallization phase diagram. The solid black line represents the solubility of a compound as a function of temperature, with the metastable zone (MSZ) represented by the dashed line. At a constant C, the solution goes from undersaturated to a supersaturated state with respect to the solute when the temperature of the system is altered. The blue line represents the typical desupersaturation path observed on the addition of seeds when added to a slightly supersaturated state.

Figure 1-4 represents the typical binary phase diagram used for the application of cooling crystallization. As the temperature is reduced, the solubility of the dissolved solute reduces in accordance with Equation 12. This causes the system to become supersaturated and so crystallization becomes thermodynamically feasible according to Equation 47. The closer the system is pushed towards the metastable zone limit (MSZ) with no change in concentration, the more likely unwanted primary nucleation is to occur. The addition of seeds removes this uncertainty when moving closer to the MSZ limit. For seeded cooling systems, the undersaturated solution is cooled slightly in order to create a small supersaturation. At this point, seed crystals of the desired crystal form are added. As soon as they are added, desupersaturation occurs. Zhang *et al.* proposed a method utilising a modified Mullin-Nyvlt equation to optimise the cooling strategy and subsequent seed loading with FBRM monitoring. From these results, they were able to propose a strategy for seeding that could be used to guide batch

crystallization processes[38]. The use of simulation has also been applied to seeded crystallizations employing cooling crystallization, it was able to design a seed recipe in order to obtain the desired yield and product size distributions of β- L-Glutamic acid[39].

Construction of cooling crystallization phase diagrams are typically done using isothermal slurring experiments at different temperatures and utilising Equation 1. This is followed by either HPLC or gravimetric analysis to determine the concentration of the solute in the liquid phase[40,41]. Although this method is highly accurate due to the qualitative method applied to them, experiments can take considerable time and product to obtain accurate results at multiple temperatures in replicates. The use of polythermal transmissivity methods are also commonly employed with systems like the Crystal16 reactor, were known concentrations of solid is slurried while being subjected to increasing temperatures. At a certain temperature, the solids present are completely dissolved following Equation 1[42–44].

1.7 Antisolvent Addition Crystallization

The use of antisolvent crystallization as a separation method is of great importance to the pharmaceutical industry. High yields of sparingly soluble solids with high added value can be obtained, although this method is poorly understood in comparison to cooling crystallizations[45]. Antisolvent crystallization involves the addition of a solvent in which the solute has very little solubility into a homogenous solution.

Going from an undersaturated solution, the addition of an antisolvent reduces the solubility of the solute significantly towards zero so creating a supersaturated solution as presented in Figure 1-5. Due to the addition of another solvent, the system is diluted and so the overall concentration is reduced. This dilution follows a linear path towards the solubility of the solute in the antisolvent, as represented by the dashed line. At a specific antisolvent fraction and supersaturation (red arrow), the solute moves from the liquid to the solid phase with the concentration being reduced by nucleation and subsequent growth (green arrow) towards equilibrium. Unlike cooling crystallization, the amount of

solids that can be obtained is highly dependent on the extent of dilution the system has experienced before crystallization.

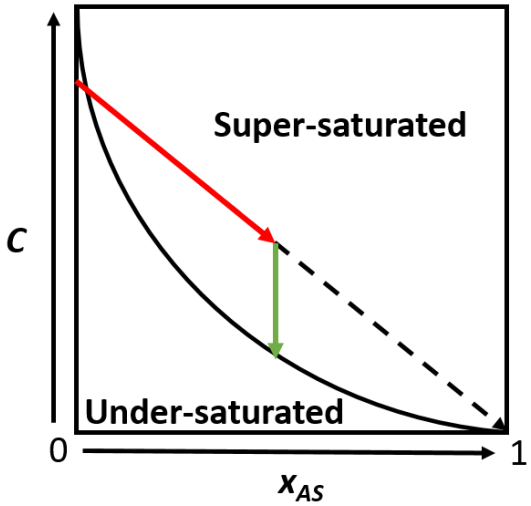

Figure 1-5: Typical representation of an antisolvent phase diagram. The solid black line represents the solubility as a function of antisolvent fraction x_{AS}. The dashed line represents the dilution line, going toward the solubility of the solvent added.

Antisolvent crystallization is highly effective in obtaining high yields due to the low solubility of the solute in the final antisolvent amount and is commonly used after a cooling crystallisation to remove remaining solids from the solvent. It has been widely applied to the crystallization of sugars due to their high solubility even at low temperatures[46,47]. For temperature sensitive materials, antisolvent crystallization is used as it can be performed at lower temperatures. Chang *et al.* used antisolvent crystallisation combined with FBRM analysis for the isolation of RDX, a highly explosive material, in acetone-water systems[48]. High supersaturations can be obtained from antisolvent crystallisations due to the sharp decrease in solubility, allowing metastable polymorphs to be identified[49]. For this reason, antisolvent crystallisation is routinely used as a method to explore the polymorphic landscape during polymorph screening[50]. For o-aminobenzoic acid, at S > 1.8 the metastable polymorph Form II nucleates singularly , with the stable form nucleating on its own at S ≤ 1.2[34]. Between these regions, both Form I and Form II nucleated concomitantly.

Due to the high supersaturations generated, primary nucleation occurring is highly likely especially at the addition point. Particle size distributions are a key process variable that must be controlled for downstream processing so both this and the polymorphic form must be controlled for batch-to-batch reproducibility[45]. Utilising mathematical modelling, optimisation of antisolvent crystallisation has been enabled for different systems as well as different reactor types[51,52]. Population Balance Modelling is widely used for the optimization of crystallising systems, being employed for both cooling and antisolvent systems. Mostafa *et al.* applied the same method alongside experimental validation to determine optimal antisolvent crystallization strategies to arrive at both solubility and kinetic sub-models. By doing this, they were able to conclude that models which utilise growth rate parameter as function of antisolvent fraction are optimal for the modelling of antisolvent crystallisations based on population balance modelling[53].

As with cooling crystallisation, the development of antisolvent phase diagrams is commonly done through slurring experiments, instead varying the antisolvent to solvent ratio. Similarly, this provides highly precise solubility values due to the sensitivity of the analytical method although is highly product intensive and time-consuming. Ter Horst proposed a method utilising the polythermal method by determining the solubility curve of Lorazepam at different ethanol-water volume/weight fractions[54]. From these, he was able to model the change in mole fraction as a function of antisolvent fraction and predict the antisolvent phase diagram at temperatures covered within the model in accordance with the Van't Hoff equation. Methods utilising PAT such as UV has also been used.

1.8 Hybrid Cooling-Antisolvent

In recent years, the applications of combined cooling and antisolvent have been investigated due the higher yields that can be obtained. The system can be monitored through PAT allowing advanced feedback control[51]. Maintaining a tight PSD is regularly used as the optimizing parameter for these systems. Nagy presented both a model-based control strategy and model-free approach to optimise a hybrid cooling-antisolvent crystallisation of lovastatin in acetone-

water. Using population balance modelling, superior control over the crystal size distribution is possible while also achieving higher yields when applying both systems concurrently[55]. Barik *et al.* utilised population balance modelling and applied it using the ACADO toolkit function within MATLAB, to design and optimise the crystallisation of acetyl salicylic acid (ASA) in ethanol-water systems for both single and multi-objectives. They applied it to cooling, antisolvent and a combination of the two, optimizing for both number average crystal size and weight mean size[57]. The utilization of models allows fewer experiments to be carried out for these systems but are subject to the validation from the experimental results. As well as tight PSD, polymorphic control must also be maintained. A combined cooling-antisolvent crystallisation of acetylsalicylic acid (ASA) showed that polymorphic form can be controlled and productivity enhanced while also reducing fines commonly generated from antisolvent crystallisations. Using FT-IR, the system was optimized for time and temperature while minimising nucleated crystals. In doing so the optimal trajectory for the process to follow was plotted and agreed with the experimental results. The supersaturation was able to be maintained at a low enough value to keep desupersaturation due to growth only[58]. Similar studies have also been carried out on sugars[47], and identifying optimal regions for obtaining specific polymorphs[59].

1.9 Benefits of Continuous Crystallization

The push from regulatory authorities to adopt a quality-by-design approach (QbD) for enhanced quality and reduced variability between batches, a common problem for batch crystallization. Continuous crystallization has been demonstrated to provide enhanced reliability of critical product attributes due to the steady-state conditions, as well as being able to recycle output streams to maximize the overall yield. The use of steady-state conditions in a continuous crystallization setup also showed applicability to produce co-crystals[60] as well as obtain the desired enantiomer[61]. It was determined that the supersaturation found to be the most important variable to control. Continuous crystallization has been demonstrated using both single, multi-stage and plug flow reactors[62–64]. In

recent years, the FDA has shown support for the application of continuous crystallization to the development of pharmaceuticals although some aspects such as variation control and the quantity of product manufactured must be ensured to be consistent[65].

1.10 Thesis Aim & Chapter Objectives

With the demand for pharmaceuticals continually increasing along with the increasing value of many drug substances, there is a need for development and improvement of key process steps. By reducing the time and amount of drug substance used up during each phase in the crystallisation development process, pharmaceuticals can be delivered to patients faster. Therefore, the aim of this thesis is to outline new methods and improve existing methodologies relating to the crystallisation design and optimization in complex multicomponent systems. Each chapter sets out to tackle a key question, with these research topics being directly linked back to the overarching aim of the thesis.

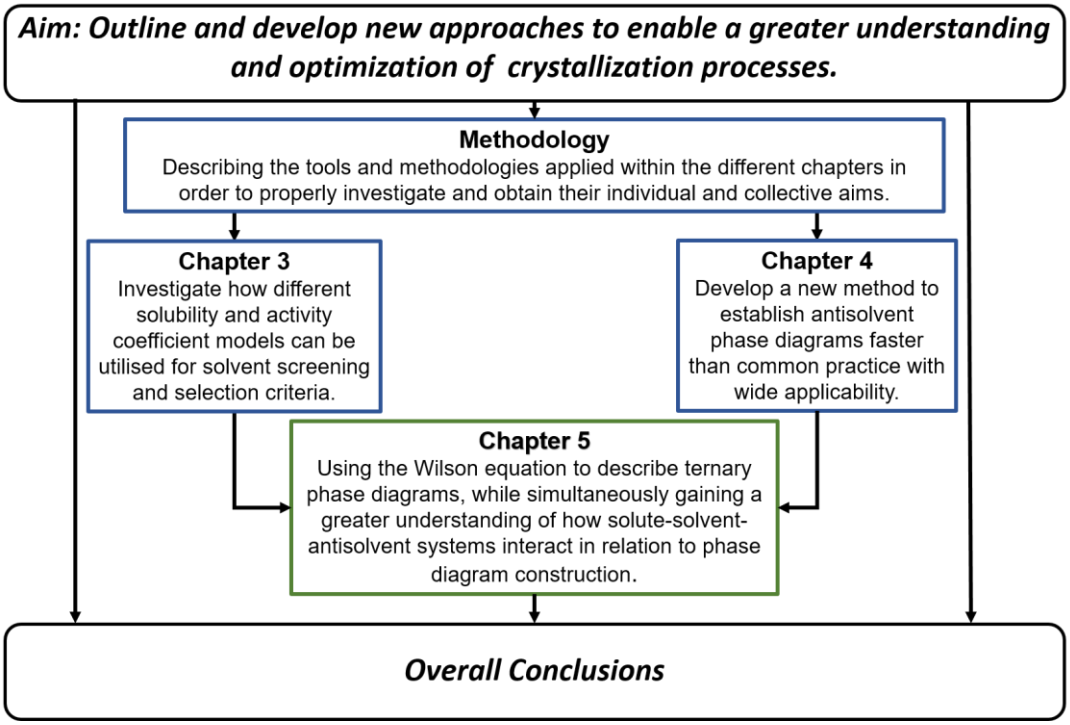

Figure 1-6: Schematic of the methodology and experimental chapters enclosed within this thesis, along with a brief description of the aim and objective for each of those sections.

Chapter 3: *Solubility and Thermodynamic Correlation of Benzoic Acid, Diphenylamine, Mefenamic Acid and Lovastatin in several solvents*

Solvent selection for the design of crystallisation processes is a time-consuming task, utilising a large number of solvents and a large amount of API material to optimise the selection process. Different solvent types will interact differently with a given API, changing the temperature dependence and optimal process operation conditions. Thermodynamic models provide quantitative as well as qualitative information on how a system behaves, providing details on the thermodynamic length scale which can often be translated into molecular interactions behaviour in process solutions. Therefore, in chapter 3, the objective is to determine the role that different solubility and activity coefficient models can play in solvent screening and selection of process criteria. To do this, the solubility of several APIs is measured at varying temperatures in a number of solvents. The experimental solubility data is used to compare various solubility models, including activity coefficient models. The latter allow a description of non-ideal behaviour which, through their fitted parameters, provide information on the specific interactions between solution components. The interaction parameters help identify which solvent types produce the required solute-solvent interactions for favourable solvent screening results.

Chapter 4*: Method for Accurately Establishing Antisolvent Phase Diagrams*

The determination of a phase diagram to use in crystallization design, optimization and control is still too time consuming and product heavy, especially in complex multicomponent mixtures. A structured approach towards valuable phase diagram data would allow to save time and compound. Therefore, in chapter 4 we investigate if antisolvent crystallization phase diagrams, can be determined more efficiently than standard practices. The objective of this chapter is to develop and establish a method to accurately determine antisolvent phase diagrams, validated by applying it to multiple system types. For this, we use clear point temperature measurements in commercially available equipment that allows measuring multiple samples simultaneously. The experimentally measured set of clear point temperatures for compositions in the complex

multicomponent system are used in their entirety to construct an empirical thermodynamic model to describe the variation of solubility as a function of antisolvent fraction and temperature, which subsequently allows antisolvent crystallization process design, operation and control.

***Chapter 5**: Activity Coefficients in Phase Diagrams of Antisolvent Crystallization*

The antisolvent crystallization processes heavily rely on the thermodynamic non-ideal nature of the antisolvent dependent solubility, dictating its applicability as a process option. Non-empirical activity coefficient models such as the Wilson model assume that the local concentration around a molecule is different from the bulk concentration due to the difference in interaction of the component molecules in the solution. The use of this model thus gives suggestions about the molecular interactions between solute-solvent-antisolvent. Therefore, in chapter 5 the objective is to determine to what extent the Wilson model can be used to describe ternary phase diagrams for antisolvent crystallization and to obtain molecular information of the interacting components in solutions. This is done for the system of the API Lovastatin in various solvents with water as the antisolvent. First, the ideal solubility of Lovastatin is described and discussed. Then, activity coefficients of the systems are determined as a function of temperature and composition by measuring Lovastatin solubility. Finally, the Wilson model for activity coefficients is fitted to the acquired experimental data to obtain interaction parameters for each solvent-water system of Lovastatin. The interaction parameters are investigated on their ability to provide information on the molecular level in ternary systems for antisolvent crystallization.

1.11 References

1. Wouters OJ, McKee M, Luyten J. Estimated Research and Development Investment Needed to Bring a New Medicine to Market, 2009-2018. *JAMA - J Am Med Assoc*. 2020;323(9):844-853. doi:10.1001/jama.2020.1166
2. Savjani KT, Gajjar AK, Savjani JK. Drug Solubility: Importance and Enhancement Techniques. *ISRN Pharm*. 2012;2012(100 mL):1-10. doi:10.5402/2012/195727

3. Committee for Human Medicinal Products. ICH guideline Q3C (R5) on impurities: Guideline for Residual Solvents. *Int Conf Harmon Tech Requir Regist Pharm Hum Use*. 2015;44(October 2002):24.

4. Lewis A, Seckler M, Kramer H, Rosmalen G. Melt Crystallisation. In: *Industrial Crystallization: Fundamentals and Applications*. ; 2015:261-281.

5. Lewis A, Kramer H, Seckler M. Thermodynamics, Crystallzation Methods and Supersaturation. In: *Industrial Crystallization: Fundamentals and Applications*. ; 2015:1-25.

6. Spyriouni T, Krokidis X, Economou IG. Thermodynamics of pharmaceuticals: Prediction of solubility in pure and mixed solvents with PC-SAFT. *Fluid Phase Equilib*. 2011;302(1-2):331-337. doi:10.1016/j.fluid.2010.08.029

7. Loschen C, Klamt A. Solubility prediction, solvate and cocrystal screening as tools for rational crystal engineering. *J Pharm Pharmacol*. 2015;67(6):803-811. doi:10.1111/jphp.12376

8. Tung HH, Tabora J, Variankaval N, Bakken D, Chen CC. Prediction of pharmaceutical solubility via NRTL-SAC and COSMO-SAC. *J Pharm Sci*. 2008;97(5):1813-1820. doi:10.1002/jps.21032

9. Myerson AS, Erdemir D, Lee AY. Thermodynamic Concepts and Ideal Solubility. In: *Handbook of Industrial Crystallization*. ; 2019:1-31.

10. Zumdahl S. The Equilibrium Constant. In: *Chemistry*. 5th ed. Houghton Mifflin; 1999:578-620.

11. Xu R, Huang C. Solubility Modeling and Solution Thermodynamics of 4-Amino-2,6-Dimethoxypyrimidine in Cosolvent Mixtures of Methanol, Ethanol, Isopropanol, and N, N-Dimethylformamide + Water. *J Chem Eng Data*. 2018;63(11):4234-4240. doi:10.1021/acs.jced.8b00719

12. Zhao H, Xu H, Yang Z, Li R. Solubility of 3,4-dichloronitrobenzene in methanol, ethanol, and liquid mixtures (methanol + water, ethanol + water): Experimental measurement and thermodynamic modeling. *J Chem Eng Data*. 2013;58(11):3061-3068. doi:10.1021/je400507u

13. Jia L, Yin Q. Insights into the mechanism of concomitant nucleation of form II and ethanol solvate of spironolactone in cooling crystallization †. 2018:9697-9706. doi:10.1039/c7ra13094e

14. Yang Y, Tang W, Li X, et al. Solubility of Benzoin in Six Monosolvents and in Some Binary Solvent Mixtures at Various Temperatures. *J Chem Eng Data*. 2017;62(10):3071-3083. doi:10.1021/acs.jced.7b00238

15. Gmehling J, Kleiber M. *Vapor-Liquid Equilibrium and Physical Properties for Distillation*.; 2014. doi:10.1016/B978-0-12-386547-2.00002-8

16. Seader JD, Henley E, Roper DK. *Seperation Process Principles-Chemical and Biochemical Operations*. 3rd ed. John Wiley & Sons, Inc.; 2011.

17. Smith JM, Ness HC Van, Abbot MM, Swihart MT. *Introduction to Chemical Engineering Thermodynamics Eight Edition*.; 2018.

18. Abbot M, Berthold J, de Loos T. *Models for Thermodynamic and Phase Equilibria Calculations*. 1st ed. (Sandler S, ed.).; 1994.

19. Vagenas GK, Marinos-Kouris D. Use of the Wilson equation for the prediction of the sorptional equilibrium of sugar-based foodstuffs. *Fluid Phase Equilib*. 1992;78(C):191-207. doi:10.1016/0378-3812(92)87034-K

20. Dojcanský J, Bafrncová S, Surový J. Application of the Wilson Equation with Binary Parameters to the Prediction of the Isothermal Vapour-Liquid Equilibrium Data of Ternary and Quaternary Systems in the Assessment of the Polar Solvent in Extractive Distillation. 2001;55(2):71-74.

21. Sadeghi R. Extension of the Wilson model to multicomponent polymer solutions: Applications to polymer-polymer aqueous two-phase systems. *J Chem Thermodyn*. 2005;37(1):55-60. doi:10.1016/j.jct.2004.08.007

22. von Raumer M, Hilfiker R. A Short Introduction to Polymorphism and Solid-State Development. In: *Polymorphism in the Pharmaceutuical Industr: Solid Form and Drug Development*. 1st ed. ; 2019:1-23.

23. Vrani E. Amorphous Pharmaeutical Solids. *Bosn J Basic Med Sci*. 2004;4(3):35-39.

24. Aitipamula S, Banerjee R, Bansal AK, et al. Polymorphs, salts, and

cocrystals: What's in a name? *Cryst Growth Des*. 2012;12(5):2147-2152. doi:10.1021/cg3002948

25. Lewis A, Seckler M, Kramer H, Rosmalen G. Polymorphism. In: *Industrial Crystallization: Fundamentals and Applications*. ; 2015:303-319.

26. Cruz-Cabeza AJ, Reutzel-Edens SM, Bernstein J. Facts and fictions about polymorphism. *Chem Soc Rev*. 2015;44(23):8619-8635. doi:10.1039/c5cs00227c

27. Lee EH. A practical guide to pharmaceutical polymorph screening & selection. *Asian J Pharm Sci*. 2014;9(4):163-175. doi:10.1016/j.ajps.2014.05.002

28. Cesur S, Gokbel S. Crystallization of mefenamic acid and polymorphs. *Cryst Res Technol*. 2008;43(7):720-728. doi:10.1002/crat.200711119

29. Ferrari ES, Davey RJ, Cross WI, Gillon AL, Towler CS. Crystallization in polymorphic systems: The solution-mediated transformation of β to α glycine. *Cryst Growth Des*. 2003;3(1):53-60. doi:10.1021/cg025561b

30. Padrela L, Zeglinski J, Ryan KM. Insight into the Role of Additives in Controlling Polymorphic Outcome: A CO2-Antisolvent Crystallization Process of Carbamazepine. *Cryst Growth Des*. 2017;17(9):4544-4553. doi:10.1021/acs.cgd.7b00163

31. Kulkarni SA, McGarrity ES, Meekes H, Ter Horst JH. Isonicotinamide self-association: The link between solvent and polymorph nucleation. *Chem Commun*. 2012;48(41):4983-4985. doi:10.1039/c2cc18025a

32. Joel Bernstein, Roger J. Davey, Jan-Olav Henck. Concomitant Polymorphs. *Angew Chemie Int Ed*. 1999;38(23):2440-3461. doi:10.1002/(SICI)1521-3773(19991203)38:23<3440::AID-ANIE3440>3.0.CO;2

33. Teychené S, Biscans B. Nucleation kinetics of polymorphs: Induction period and interfacial energy measurements. *Cryst Growth Des*. 2008;8(4):1133-1139. doi:10.1021/cg0609320

34. Jiang S, Horst JH, Jansens PJ. Concomitant Polymorphism of o-Aminobenzoic Acid in Antisolvent Crystallization. *Cryst Growth Des*.

2008;8(1):37-43.

35. ter Horst JH, Kramer HJM, Jansens PJ. A New Molecular Modeling Approach To Predict Concomitant Nucleation of Polymorphs. *Cryst Growth Des*. 2002;2(5):351-356.

36. Black S, Muller F, Fielding M. A Practical Approach for Using Solubility to Design Cooling Crystallisations. *Org Process Res Dev*. 2009;13:1315-1321.

37. Lewis A, Seckler M, Kramer H. Batch Crystallisation. In: *Industrial Crystallization*. ; 2015:178-191.

38. Zhang D, Liu L, Xu S, Du S, Dong W, Gong J. Optimization of cooling strategy and seeding by FBRM analysis of batch crystallization. *J Cryst Growth*. 2018;486:1-9. doi:10.1016/j.jcrysgro.2017.12.046

39. Zhang F, Liu T, Chen W, Ma CY, Wang XZ. Seed Recipe Design for Batch Cooling Crystallization with Application to l -Glutamic Acid. *Ind Eng Chem Res*. 2019;58(8):3175-3187. doi:10.1021/acs.iecr.8b06006

40. Pinho SP, Macedo EA. Solubility of NaCl, NaBr, and KCl in water, methanol, ethanol, and their mixed solvents. *J Chem Eng Data*. 2005;50(1):29-32. doi:10.1021/je049922y

41. Svärd M, Nordström FL, Jasnobulka T, Rasmuson ÅC. Thermodynamics and nucleation kinetics of m-aminobenzoic acid polymorphs. *Cryst Growth Des*. 2010;10(1):195-204. doi:10.1021/cg900850u

42. Mullin J. Ideal and Non-ideal Solutions. In: *Nucleation*. 4th ed. ; 2001:98-100.

43. Bhamidi V, Kenis PJA, Zukoski CF. Probability of Nucleation in a Metastable Zone : Cooling Crystallization and Polythermal Method. doi:10.1021/acs.cgd.7b00875

44. Lenka M, Sarkar D. Determination of metastable zone width, induction period and primary nucleation kinetics for cooling crystallization of L-asparaginenohydrate. *J Cryst Growth*. 2014;408:85-90. doi:10.1016/j.jcrysgro.2014.09.027

45. Karpinski P, Baldyga J. Precipitation Processes. In: *Handbook of Industrial*

Crystallization. 3rd ed. ; 2019:217-265.

46. Macedo EA. Solubility of amino acids, sugars, and proteins. *Pure Appl Chem*. 2005;77(3):559-568. doi:10.1351/pac200577030559

47. Giulietti M, Bernardo A. Crystallization by Antisolvent Addition and Cooling. *Cryst - Sci Technol*. 2012. doi:10.5772/50328

48. Chang J, Wang J, Diao Y, Wang W, Chen Q, Yu Z. Study on the solubility characteristic of the antisolvent crystallization of RDX. *J Phase Equilibria Diffus*. 2011;32(3):206-211. doi:10.1007/s11669-011-9872-3

49. Hansen TB, Qu H. Formation of Piroxicam Polymorphism in Solution Crystallization : E ff ect and Interplay of Operation Parameters. 2015. doi:10.1021/acs.cgd.5b01016

50. Hilfiker R, Blatter F, Szelagiewicz M. Screening for Polymorphs,Hydrates and Solvates. In: Hilfiker R, von Raumer M, eds. *Polymorphism in the Pharmaceutuical Industr: Solid Form and Drug Development*. 1st ed. ; 2019:241-256.

51. Lee S, Lee CH, Kim WS. Anti-solvent crystallization of L-threonine in Taylor crystallizers and MSMPR crystallizer: Effect of fluid dynamic motions on crystal size, shape, and recovery. *J Cryst Growth*. 2017;469:119-127. doi:10.1016/j.jcrysgro.2016.08.021

52. Ferguson S, Morris G, Hao H, Barrett M, Glennon B. Characterization of the anti-solvent batch, plug flow and MSMPR crystallization of benzoic acid. *Chem Eng Sci*. 2013;104:44-54. doi:10.1016/j.ces.2013.09.006

53. Mostafa Nowee S, Abbas A, Romagnoli JA. Antisolvent crystallization: Model identification, experimental validation and dynamic simulation. *Chem Eng Sci*. 2008;63(22):5457-5467. doi:10.1016/j.ces.2008.08.003

54. Vellema J, Hunfeld NGM, Van Den Akker HEA, Ter Horst JH. Avoiding crystallization of lorazepam during infusion. *Eur J Pharm Sci*. 2011;44(5):621-626. doi:10.1016/j.ejps.2011.10.010

55. Nagy ZK, Fujiwara M, Braatz RD. Modelling and control of combined cooling and antisolvent crystallization processes. *J Process Control*.

2008;18(9):856-864. doi:10.1016/j.jprocont.2008.06.002

56. Braatz RD. Advanced control of crystallization processes. *Annu Rev Control*. 2002;26 I:87-99. doi:10.1016/S1367-5788(02)80016-5

57. Barik K, Prusti P, Mohapatra SS. Single- and multi-objective optimisation for a combined cooling and antisolvent semi-batch crystallisation process with an ACADO toolkit. *Indian Chem Eng*. 2020;62(3):287-300. doi:10.1080/00194506.2019.1677511

58. Lindenberg C, Krättli M, Cornel J, Mazzoti M, Brozio J. Design and optimization of a combined cooling/antisolvent crystallization process. *Cryst Growth Des*. 2009;9(2):1124-1136. doi:10.1021/cg800934h

59. Holaň J, Skořepová E, Heraud L, et al. Polymorphic Crystallization and Structural Aspects of Agomelatine Metastable Form X Prepared by Combined Antisolvent/Cooling Process. *Org Process Res Dev*. 2016;20(1):33-43. doi:10.1021/acs.oprd.5b00241

60. Zhang D, Xu S, Du S, Wang J, Gong J. Progress of Pharmaceutical Continuous Crystallization. *Engineering*. 2017;3(3):354-364. doi:10.1016/J.ENG.2017.03.023

61. Galan K, Eicke MJ, Elsner MP, Lorenz H, Seidel-Morgenstern A. Continuous preferential crystallization of chiral molecules in single and coupled mixed-suspension mixed-product-removal crystallizers. *Cryst Growth Des*. 2015;15(4):1808-1818. doi:10.1021/cg501854g

62. Pawar N, Agrawal S, Methekar R. Continuous Antisolvent Crystallization of α-Lactose Monohydrate: Impact of Process Parameters, Kinetic Estimation, and Dynamic Analysis. *Org Process Res Dev*. 2019;23(11):2394-2404. doi:10.1021/acs.oprd.9b00301

63. Sultana M, Jensen KF. Microfluidic continuous seeded crystallization: Extraction of growth kinetics and impact of impurity on morphology. *Cryst Growth Des*. 2012;12(12):6260-6266. doi:10.1021/cg301538y

64. Lawton S, Steele G, Shering P, Zhao L, Laird I, Ni XW. Continuous crystallization of pharmaceuticals using a continuous oscillatory baffled

crystallizer. *Org Process Res Dev*. 2009;13(6):1357-1363. doi:10.1021/op900237x

65. Likozar B, Orehek J. Continuous Crystallization Processes in Pharmaceutical Manufacturing : A Review. 2021. doi:10.1021/acs.oprd.0c00398

66. Gong J, Tang W. Nucleation. *Pharm Cryst Sci Eng*. 2018:47-88. doi:10.1002/9781119046233.ch2

67. Sheikholeslamzadeh E, Rohani S. Solubility prediction of pharmaceutical and chemical compounds in pure and mixed solvents using predictive models. *Ind Eng Chem Res*. 2012;51(1):464-473. doi:10.1021/ie201344k

68. Lewis R, Evans W. Solutions and Solubility. *Chemistry (Easton)*. 2018:173-193. doi:10.1057/978-1-137-61037-9_11

69. Mane MB, Shinde SN. Vapor Liquid Equilibria: a Review. *Sci Revs Chem Commun*. 2012;2(2):158-171. www.sadgurupublications.com.

70. De Souza B, Keshavarz L, Steendam RRE, et al. Solubility Measurement and Thermodynamic Modeling of N-(4-Methylphenyl- Z-3-chloro-2-(phenylthio)propenamide in 12 Pure Solvents at Temperatures Ranging from 278.15 to 318.15 K. *J Chem Eng Data*. 2018;63(5):1419-1428. doi:10.1021/acs.jced.7b01011

71. Reus MA, Van Der Heijden AEDM, Ter Horst JH. Solubility Determination from Clear Points upon Solvent Addition. *Org Process Res Dev*. 2015;19(8):1004-1011. doi:10.1021/acs.oprd.5b00156

72. Brittain HG. Vibrational spectroscopic studies of cocrystals and salts. 2. The benzylamine-benzoic acid system. *Cryst Growth Des*. 2009;9(8):3497-3503. doi:10.1021/cg9001972

73. Surov AO, Terekhova I V., Bauer-Brandl A, Perlovich GL. Thermodynamic and structural aspects of some fenamate molecular crystals. *Cryst Growth Des*. 2009;9(7):3265-3272. doi:10.1021/cg900002q

74. Temperini MLA, Petrilli HM, Constantino VRL. Mefenamic Acid Anti-In fl ammatory Drug: Probing Its Polymorphs by Vibrational (IR and Raman)

and Solid-State NMR Spectroscopies. 2014. doi:10.1021/jp500988k

75. Kato F, Otsuka M, Matsuda Y. Kinetic study of the transformation of mefenamic acid polymorphs in various solvents and under high humidity conditions. 2006;321:18-26. doi:10.1016/j.ijpharm.2006.04.020

76. Febra SA, Bernet T, Mack C, et al. Extending the SAFT-γ Mie approach to model benzoic acid, diphenylamine, and mefenamic acid: Solubility prediction and experimental measurement. *Fluid Phase Equilib*. 2021;540:113002. doi:10.1016/j.fluid.2021.113002

77. Granberg RA, Rasmuson ÅC. Solubility of paracetamol in pure solvents. *J Chem Eng Data*. 1999;44(6):1391-1395. doi:10.1021/je990124v

78. Sun H, Gong JB, Wang JK. Solubility of Lovastatin in acetone, methanol, ethanol, ethyl acetate, and butyl acetate between 283 K and 323 K. *J Chem Eng Data*. 2005;50(4):1389-1391. doi:10.1021/je0500781

79. Mudalip SKA, Bakar MRA, Jamal P, Adam F. Prediction of Mefenamic Acid Solubility and Molecular Interaction Energies in Di ff erent Classes of Organic Solvents and Water. *Ind Eng Chem Res*. 2018. doi:10.1021/acs.iecr.8b02722

80. Wan Y, He H, Zhang P, et al. Solid-liquid equilibrium solubility and thermodynamic properties of cis-5-norbornene-endo-2,3-dicarboxylic anhydride in fourteen pure solvents and three binary solvents at various temperatures. *J Mol Liq*. 2020;297:111396. doi:10.1016/j.molliq.2019.111396

81. Shayanfar A, Velaga S, Jouyban A. Fluid Phase Equilibria Solubility of carbamazepine , nicotinamide and carbamazepine – nicotinamide cocrystal in ethanol – water mixtures. *Fluid Phase Equilib*. 2014;363:97-105. doi:10.1016/j.fluid.2013.11.024

82. Elliot JR, Lira CT. Introduction to Multicomponent Systems. In: *Introductory Chemical Engineering Thermodynamics*. ; 2012:369-411.

83. Gothard FA, Codrea Clobanu MF, Breban DG, Bucur CI, Sorescu G V. Predicting the Parameters in the Wilson Equations for Activity Coefficients

in Binary Hydrocarbon Systems. *Ind Eng Chem Process Des Dev*. 1976;15(2):333-337. doi:10.1021/i260058a020

84. Hristova M, Donchev T, Kolev D, Baloch I, Georgiev H. Parameter'S Estimate in Wilson Equation. *Int Electron J Pure Appl Math*. 2015;7(3). doi:10.12732/iejpam.v9i1.4

85. Nti-Gyabaah J, Chmielowski R, Chan V, Chiew YC. Solubility of lovastatin in a family of six alcohols: Ethanol, 1-propanol, 1-butanol, 1-pentanol, 1-hexanol, and 1-octanol. *Int J Pharm*. 2008;359(1-2):111-117. doi:10.1016/j.ijpharm.2008.03.046

86. ter Horst JH, Schmidt C, Ulrich J. Fundamentals of Industrial Crystallization. In: *Handbook of Crystal Growth*. ; 2015:1317-1346.

87. Wichianphong N, Charoenchaitrakool M. Journal of Industrial and Engineering Chemistry Statistical optimization for production of mefenamic acid – nicotinamide cocrystals using gas anti-solvent (GAS) process. *J Ind Eng Chem*. 2018;62:375-382. doi:10.1016/j.jiec.2018.01.017

88. Sun H, Wang J. Solubility of lovastatin in acetone + water solvent mixtures. *J Chem Eng Data*. 2008;53(6):1335-1337. doi:10.1021/je800063d

89. Acree WE. Comments on "Solubility and Dissolution Thermodynamic Data of Cefpiramide in Pure Solvents and Binary Solvents." *J Solution Chem*. 2018;47(1):198-200. doi:10.1007/s10953-018-0714-3

90. Pramanik R, Bagchi S. Studies on solvation interaction: Solubility of a betaine dye and a ketocyanine dye in homogeneous and heterogeneous media. *Indian J Chem - Sect A Inorganic, Phys Theor Anal Chem*. 2002;41(8):1580-1587.

91. Ruidiaz MA, Delgado DR, Martínez F, Marcus Y. Solubility and preferential solvation of sulfadiazine in 1,4-dioxane+water solvent mixtures. *Fluid Phase Equilib*. 2010;299(2):259-265. doi:10.1016/j.fluid.2010.09.027

92. Ter Horst JH, Deij MA, Cains PW. Discovering New Co-Crystals. *Cryst Growth Des*. 2009;9(3):1531-1537.

93. Yoshida MI, Oliveira MA, Gomes ECL, Mussel WN, Castro W V., Soares CD V.

Thermal characterization of lovastatin in pharmaceutical formulations. *J Therm Anal Calorim*. 2011;106(3):657-664. doi:10.1007/s10973-011-1510-0

94. Sullivan RA, Davey RJ, Sadiq G, et al. Revealing the roles of desolvation and molecular self-assembly in crystal nucleation from solution: Benzoic and p -aminobenzoic acids. *Cryst Growth Des*. 2014;14(5):2689-2696. doi:10.1021/cg500441g

95. Shayanfar A, Fakhree MAA, Acree WE, Jouyban A. Solubility of lamotrigine, diazepam, and clonazepam in ethanol + water mixtures at 298.15 K. *J Chem Eng Data*. 2009;54(3):1107-1109. doi:10.1021/je8007827

96. Kongsamai P. Seperation of DL-Asparagine Enantiomers Using Crystallization Inhibitors. 2017.

97. Romero S, Escalera B, Bustamante P. Solubility behavior of polymorphs I and II of mefenamic acid in solvent mixtures. 1999;178:193-202.

98. Mack C, Hoffmann J, Sefcik J, ter Horst JH. Phase Diagram Determination and Process Development for Continuous Antisolvent Crystallizations. *Crystals*. 2022;12(8).

99. Black S, Dang L, Liu C, Wei H. On the measurement of solubility. *Org Process Res Dev*. 2013;17(3):486-492. doi:10.1021/op300336n

100. Zhang D, Xu S, Du S, Wang J, Gong J. Progress of Pharmaceutical Continuous Crystallization. *Engineering*. 2017;3(3):354-364. doi:10.1016/J.ENG.2017.03.023

101. Bustamante P, Navarro J, Romero S, Escalera B. Thermodynamic origin of the solubility profile of drugs showing one or two maxima against the polarity of aqueous and nonaqueous mixtures: Niflumic acid and caffeine. *J Pharm Sci*. 2002;91(3):874-883. doi:10.1002/jps.10076

102. Granberg RA, Rasmuson AC. Solubility of paracetamol in binary and ternary mixtures of water plus acetone plus toluene. *J Chem Eng Data*. 2000;45(3):478-483. doi:10.1021/je990272l

103. Pacheco DP, Martínez F. Thermodynamic analysis of the solubility of

naproxen in ethanol + water cosolvent mixtures. *Phys Chem Liq*. 2007;45(5):581-595. doi:10.1080/00319100701313862

104. Wang L, Yang W, Song Y, Gu Y. Solubility Measurement, Correlation, and Molecular Interactions of 3-Methyl-6-nitroindazole in Different Neat Solvents and Mixed Solvents from T = 278.15 to 328.15 K. *J Chem Eng Data*. 2019;64(8):3260-3269. doi:10.1021/acs.jced.8b01256
105. Li X, Chen J, Chen G, Zhao H. Solubility modelling, solution thermodynamics and preferential solvation of hymecromone in binary solvent mixtures of: N, N -dimethylformamide + methanol, ethanol or n -propanol. *RSC Adv*. 2017;7(73):46378-46387. doi:10.1039/c7ra07587a
106. Sato S, Hata T, Tsujita Y. The structure of monacolin K, C24H36O5. *Acta Cryst*. 1984;40(1):195-198.
107. Turner TD, Hatcher LE, Wilson CC, Roberts KJ. Habit Modification of the Active Pharmaceutical Ingredient Lovastatin Through a Predictive Solvent Selection Approach. *J Pharm Sci*. 2019;108(5):1779-1787. doi:10.1016/j.xphs.2018.12.012
108. Naik JB, Mokale V. Preparation of Freeze-dried Solid Dispersion Powder using Mannitol to Enhance Solubility of Lovastatin and Development of Sustained Release Tablet Dosage Form. *Columbia Int Publ Am J Pharm Sci Nanotechnol*. 2014;1(1):11-26. doi:10.13140/2.1.4312.5769
109. Mikhail SZ, Kimel WR. Densities and Viscosities of Methanol-Water Mixtures. *J Chem Eng Data*. 1961;6(4):533-537. doi:10.1021/je60011a015
110. Perry RH, Green D. Densities of Aquous Organic Mixtures. In: *Perry's Chemical Engineers Handbook*. 7th ed. ; 1997:109-117. https://www.handymath.com/cgi-bin/isopropanolwghtvoltble5.cgi?submit=Entry.
111. Washburn EW. *International Critical Tables of Numerical Data of Physics, Chemistry, and Technology*. Vol 3. 1st ed. New York; 1930.
112. Thomas KT, McAllister RA. Densities of liquid-acetone-water solutions up to their normal boiling points. *AIChE J*. 1957;3(2):161-164.

doi:10.1002/aic.690030206

113. Asghar SZ, Jouyban A, Martinez F, Rahimpour E. Solubility of naproxen in ternary mixtures of {ethanol + propylene glycol + water} at various temperatures: Data correlation and thermodynamic analysis. *J Mol Liq*. 2018;268:517-522. doi:10.1016/j.molliq.2018.07.082

114. Abbott M, Prausnitz J. Modelling the Excess Gibbs Energy. In: *Models for Thermodynamic and Phase Equilibria Calculations*. ; 1994:1-87.

115. Anslyn E, Dougherty D. Binding Forces. In: Murzdek J, ed. *Modern Physical Organic Chemistry*. 1st ed. ; 2006:168-177.

116. Editor G, Mccoustra M, Vendrell O, et al. Water–methanol mixtures: topology of hydrogen bonded network. *Phys Chem Chem Phys*. 2008;(10):5004-5011. doi:10.1039/b812223g

117. Yang B, Cao X, Lang H, Wang S, Sun C. Study on hydrogen bonding network in aqueous methanol solution by Raman spectroscopy. *Spectrochim Acta Part A Mol Biomol Spectrosc*. 2020;225:117488. doi:10.1016/j.saa.2019.117488

118. Valavi M, Svärd M, Rasmuson ÅC. Improving Estimates of the Crystallization Driving Force: Investigation into the Dependence on Temperature and Composition of Activity Coefficients in Solution. *Cryst Growth Des*. 2016;16(12):6951-6960. doi:10.1021/acs.cgd.6b01137

Chapter 2: Methodology

In this work, a number of experimental and analytical tools are implemented in order to reach the desired objective in each chapter. As the accuracy of the experimental findings are highly dependent on the analytical tools implemented as well as the techniques, understanding how these tools and techniques can be effectively utilised is important in determining its applicability.

Therefore, this chapter looks at providing some theoretical background to the experimental techniques alongside the off-line and in-line analytical tools implemented used throughout the thesis. For all analytical tools detailed in this section and used throughout the thesis, the standard SOP provided by the facility was followed. For the techniques utilised were no SOP is provided, the systematic steps taken and considerations taken when conducting such techniques is laid out.

2.1 Differential Scanning Calorimetry Analysis (DSC)

For any new compound, determination of specific thermodynamic properties is a first step in the characterization process. By measuring the thermal properties of a substance, a connection between temperature and its physical properties enable the determination of the enthalpy of fusion for that specific substance. DSC enables this, using only a small amount of material (<5mg) to provide large amounts of experimental data.

The 'Heat-Flux' method is the most used type of DSC analysis. The method relies on measuring the difference in heat flow observed between two crucibles: one containing a known sample and the other a blank reference. By placing both samples within a furnace, both experience the same heat flow from the furnace as it linearly increases in temperature. At a specific temperature, the sample will undergo either an exothermic or an endothermic reaction, displaying either a positive or a negative shift away from the baseline respectively as has been represented in Figure 2-1. This is due to the heat flow having to be increased or reduced in order to keep the energy input $\boldsymbol{E}$ the same as the reference sample. After a certain time, the shift moves back to the baseline as the heat flow readjusts back to the reference sample. Using the differences in heat flows measured

between the sample and reference, information about the thermal and so physical properties of the substance is determined.

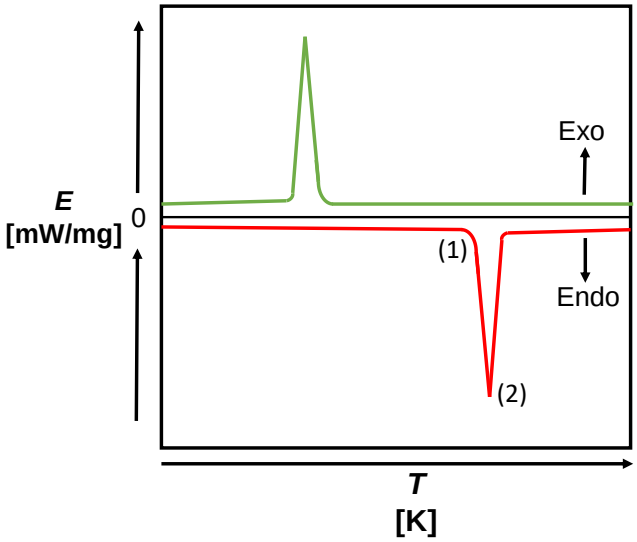

Figure 2-1: Visual representation of a DSC thermogram for booth heating and cooling cycles. (1) and (2) represent the melting onset and the point at which the sample has been fully melted respectively.

These exothermic or endothermic reactions correspond directly to the recrystallization or melting of the measured sample respectively. Therefore, these reactions provide a unique fingerprint to the thermal and physical properties of the compound. In Figure 2-1, (1) represents the point at which the measured sample begins to melt within the crucible and provides the exact melting point T_m of the compound, with the change in heat flow quickly falling down to (2) where the sample has fully melted. From there the heat flow re-adjusts back to the base with no further reduction in heat flow required with the sample already fully melted. The extent at which this heat flow varied provides the energy of its intermolecular bonding between the molecules, with larger variances showing larger bond strength. Therefore, by looking at the area under the observed peak, the enthalpy of fusion ΔH_f of the compound is determined. Both the T_m and ΔH_f provide unique knowledge specific to the binding energy of the molecules, with these specific qualities used exclusively in thermodynamic principles such as the Van't Hoff equation, to describe the behaviour of the molecule under certain conditions such as solubility calculations.

2.2 X-ray Powder Diffraction

XRPD is regarded as the main fingerprint technique for identifying the presence and purity of an API. As most APIs have a unique crystal lattice and so unique powder diffraction pattern, the presence of impurities and other crystal structures such as polymorphs are accurately identified within powder samples, and so the overall purity of the sample with the desired product is determined.

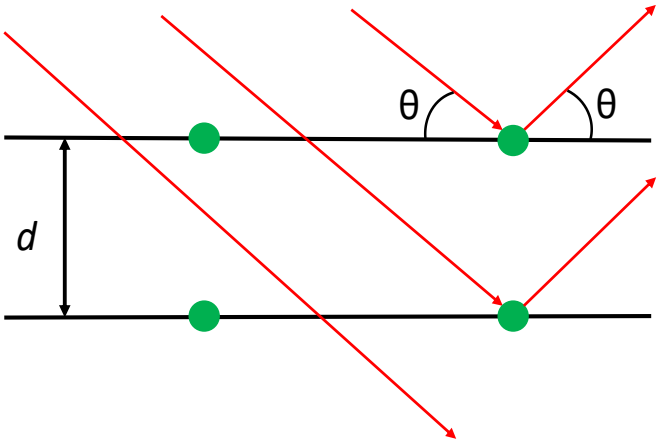

Figure 2-2: Visual representation of x-rays (red line) passing through and being diffracted by atoms (green dots) within a crystal lattice.

When x-ray radiation strikes the atoms on surface of a crystal surface, partial scattering of the rays is observed with other rays passing through the crystal as observed in Figure 2-2. As crystals have their atoms arranged periodically within each crystal layer, diffraction will provide unique knowledge of the atomic arrangement within the crystal structure. As long as the material measured sample is crystalline in nature with periodic atomic structures, diffraction will occur unlike in amorphous materials. If diffracted rays of two different layers within the crystal are constructive in nature, a peak at a specific angle is observed in the sample diffraction pattern, whereas if they are destructive no peak in the pattern will be observed. According to Braggs Law, peaks will only be observed if:

$$sin\theta = \frac{n\lambda}{2d} \qquad 51$$

Where θ is the angle of diffraction observed by the x-rays of a specific wavelength λ with the layers between the crystal layers d. The observed intensity of a peak in the diffraction pattern is also important in determining the atomic configuration of the molecules on each plane. This peak amplitude is determined by two main factors:

1. Where the atoms are on each atomic plane within the crystal structure.
2. The type of atoms present on those atomic planes.

The larger the intensity of each peak, the more rays have been diffracted in a particular direction and so provides exact coordinates of the atomic configuration in the crystal structure. These exact coordinates then determine the atomic configuration.

2.3 Solubility Measurement Procedure

A known amount of the compound was weighed into a 1.5 ml HPLC vial. A solvent mixture of a specific antisolvent fraction was weighed into a glass beaker and stirred. Once adequately mixed, 1ml of the prepared solvent mixture was pipetted into the pre-weighed vial containing the compound. The vial was then reweighed in order to accurately determine the exact composition of the sample.

The Crystal16 Multiple Reactor (Technobis, Netherlands) was used to determine the saturation temperature for each prepared sample: 16 vials of differing concentrations, all under stirred suspensions conditions, resulting in 16 clear point temperature determinations in 1 day. Saturation temperatures are obtained using a light transmission method, utilising the passage of light through a small vessel. When solids are present in the vial, the transmission of light through the vial is hindered by the particles, in the absence of particles the light passes unhindered.

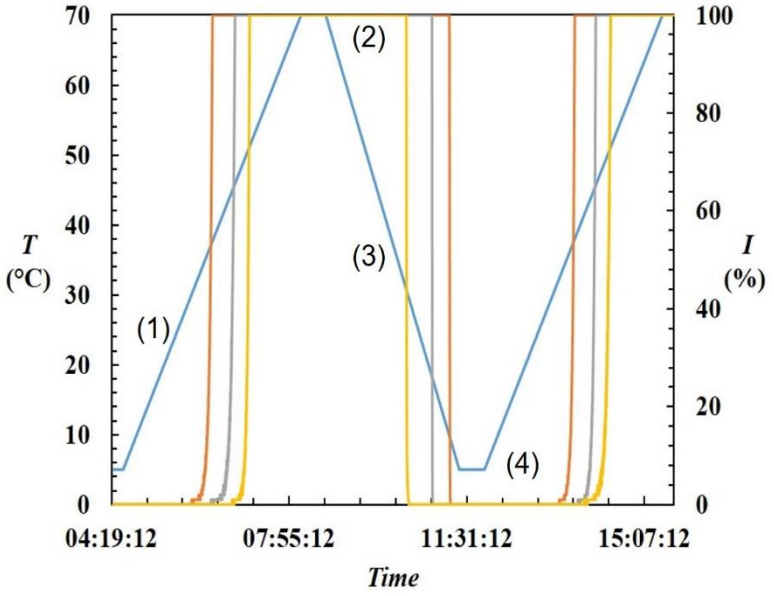

Figure 2-3: Graphical Representation of the technique used to obtain the saturation temperatures of differing concentrations of solute. The solid blue line represents the temperature variation experienced by the solution in the vials, with the solid vertical lines indicating a change in transmissivity as solute particles dissolve. The vertical lines designate the dissolution of different solutions of increasing concentration, with higher concentrations dissolving at higher temperatures. The numbers represent the different stages of the heating and cooling cycles: (1) the dissolution of solutions of increasing concentration at a slow heating rate for clear point determination; (2) hold step to ensure complete dissolution with subsequent tune step ensuring accurate cloud and clear point determinations in following steps; (3) the slow cooling of the solutions to induce recrystallization, with solid lines indicating the presence of solid particles due to reduced transmissivity; (4) the subsequent heating step in order to obtain different measurements of the same concentration for accuracy.

Due to the production methods generally applied to solutes before distributing, the solute must first be fully dissolved in the solvent before any appropriate readings can be made. To do this, a fast-heating rate is applied (1 or 2 °C/min) up to a set point temperature whereby indicating whether or not the concentration

of solids present in the solution can be adequately dissolved at the set maximum temperature. Once known, the maximum set point temperature is adjusted accordingly. Following on from this, a hold step of 30 minutes is applied, represented by (2) in Figure 2-3, in order to ensure complete dissolution of the solids. After the allocated time at which the temperature is held, a tune step is carried out. By carrying out this step, the transmission of light at which a clear solution is present in the vial is registered for subsequent heating and cooling cycles to ensure accuracy. Following this a cooling step (3) is applied at a rate of 0.3 °C/min to a set temperature and held here for a predetermined period (4), depending on the size of the metastable zone width (MSZW). The rate used is dependent on the size of the metastable zone, with slower rates allowing smaller MSZ and so more likelihood of recrystallization during the cooling ramp. By cooling the vial, the solubility of the solute in the solution decreases. At some temperature, the solute crystallizes out of solution. This increase in solid particles in the vial reduces the amount of light passing through the vessel, reducing the transmissivity from 100% indicating the presence of crystallized particles. Once all vials have recrystallized, a slow heating rate (0.2 or 0.3 °C/min) is applied as represented in (1) of Figure 2-3. This allows accurate measurements to be obtained within a sufficiently small timescale. The clear point temperature for a specific concentration is denoted at which temperature upon heating the transmissivity of light through the vial reaches 100%, indicating all particles dissolved. Once a solution is dissolved initially it is visually checked to ensure solids are dissolved. In doing so, also checking for issues which could cause discrepancies between results, such as crowning. Crowning is when solids gather around vial walls above the solvent level during stirring, this removing them from the dissolving slurry. This will reduce the clear point temperature so reducing accuracy of results. If this is observed, the headspace between the solvent level and top of the vial is reduced on subsequent runs. For accuracy, subsequent heating and cooling cycles were performed until 3/4 different measurements have been recorded. The average of the clear point temperatures is taken as the saturation temperature for the composition in the vial. In doing so, the experimental error of the method is identified as well as any other instances

(polymorphism) is identified due to significant changes in clear point. Clear point values with a variation greater than 1 °C per run between other values were discounted and runs repeated. The temperatures at which the solutions are held is dependent on the boiling and freezing point of the solvents used.

Chapter 3: Solubility and Thermodynamic Correlation of Benzoic Acid, Diphenylamine, Mefenamic Acid and Lovastatin in Several Solvents

Corin Mack[1], Stephanie Urwin[1], Carlos Moreno[1] Jan Sefcik[2], Joop H. ter Horst[1,3]

1. University of Strathclyde, EPSRC Centre for Innovative Manufacturing in Continuous Manufacturing and Crystallization (CMAC), Strathclyde Institute of Pharmacy and Biomedical Sciences, Technology and Innovation Centre, 99 George Street, Glasgow G1 1RD, United Kingdom3. Laboratoire Sciences et Méthodes Séparatives, Université de Rouen Normandie, Place Emile Blondel, 76821 Mont Saint Aignan Cedex, France

3.1 Abstract

Solubilities in a large number of solvents are required for solvent selections targeting the optimization of the crystallization processes. This requires the consumption of large amounts of the active pharmaceutical ingredient in the early stages of process and product development. In this study, the solubilities of 4 model compounds (Benzoic Acid, Diphenylamine, Mefenamic Acid and Lovastatin) in a number of solvents were obtained using the temperature variation method. Solubility correlations (Van't Hoff, Apelblat and Buchowski-Ksaizaczak) and thermodynamic activity coefficient models (Margules, Van Laar and Wilson) were applied to the measured solubilities. All systems showed good correlation between the measured and predicted values, with the Wilson equation being the most accurate. The application of these models enables a better understanding of the interactions between solute-solvent molecules, with the Wilson interaction parameters providing information on the strength of interactions between molecules. The results show that negative Wilson parameters are distinctive of strong solute-solvent molecules and so have a negative deviation from ideality. This negative deviation is indicative of higher solubility. The applicability of models to solvent selection protocols is possible using the regressed coefficients with interactions dictated by specific functional groups.

3.2 Introduction

Within the pharmaceutical and fine chemical industry, crystallization is used as key separation and purification operation to produce a crystalline product of nearly 100% purity[5,66]. For the successful optimization of a crystallization process, a key step required is that of the solvent selection[67]. This requires an extensive number of experimental solubilities to be obtained for the chosen API, which can lead to large amount of valuable product lost as well as significantly influencing the time to market. For this process to be undertaken properly, the solubility of the API must be determined in a large variety of solvent types, ensuring the most effective API-solvent interactions for the obtaining of maximum process yield.

Activity coefficient analysis provides an effective method to further understand the interactions within a system, providing knowledge about how the system behaves in the presence of a specific solvent type[68]. By utilizing the thermal properties of a solute, the activity coefficient of an API in a solvent at a specific temperature is enabled, indicating the degree of non-ideality observed by the system. Thermodynamic modelling of the extent of non-ideality has been widely utilized in the chemical industry, using the obtained model parameters to design processes for the separation of two solvents within distillation columns[18,69]. Similar methods have also been applied for the design of crystallization systems with De Souza et al. using a similar method to provide valuable thermodynamic information for the advancement of an optimized synthetic process[70]. Although the method of applying thermodynamic equations to provide parameters for crystallisation modelling is well investigated, thermodynamic models also provide information on the molecular interactions between components. These interactions are directly related to the difference in solubility of a compound when comparing different solvent systems. The meaning of the extrapolated parameters with regards to molecular interactions is not dissected.

In this chapter, the objective is to investigate how different solubility and activity models can effectively be utilised to describe the solubility data in such a way that they provide information about the molecular interactions in a system. The

information gained from this type of analysis can be used to dictate and enhance solvent screening and selection procedures. The solubility behaviour of Mefenamic Acid (MFA), Benzoic acid (BA), Diphenylamine (DPA) and Lovastatin (LOV) in a variety of different solvent types (aprotic polar, protic apolar and protic polar) are determined and analysed. The activity coefficients of each solute-solvent pair are determined using the ideal solubility obtained from thermal analysis techniques. Using six thermodynamic models to describe and correlate the solubility and activity coefficients for each API-solvent pair enables an improved understanding of the interactions taking place between the solute and solvent molecules.

The experimental results obtained from this study was applied to SAFT-gamma Mie solubility modelling. In doing so, the solubility of Mefenamic Acid Form I was predicted, with this being previously unavailable due to the polymorphic transformation to the metastable Form II at higher temperatures.

3.3 Materials and Methodology

3.3.1 Materials

The compounds used for this study represent functional group interactions which are required for solubility modelling by SAFT-gamma Mie as well as compounds which are commonly observed in industry. Benzoic Acid (BA, 99%), Mefenamic acid (MFA, 98%) and Diphenylamine (DPA, 98%) were supplied by Sigma Aldrich (MerkKGaA, Germany), with the polymorphic forms supplied all being of their stable form. Lovastatin (LOV, 99%) was provided by Molekula The solvents used are listed in Table 3-1.

Table 3-1 - The solvents used within this study with their molecular weights (MW). The solvent acronym is used throughout the paper.

Solvent	Acronym	Purity [%]	MW [g/mol)	Supplier
Ethanol	EtOH	99	46.1	VWR
Propan-1-ol	PrOH	99	60.1	VWR
Propan-2-ol	IPA	99		VWR
Butan-1-ol	BuOH	99	74.1	VWR
Butan-2-ol	2-BuOH	99		VWR
Pentan-2-ol	PeOH	99	88.2	VWR
Acetone	AcO	99	58.1	VWR
Ethyl Acetate	EtAc	99	88.1	VWR
Propyl Acetate	PrAc	99	102.1	VWR
Butyl Acetate	BuAc	99	116.2	VWR
Iso-Butyl Acetate	IBA	99		VWR
2-Butanone	2-BuO	99	72.1	VWR
2-Heptanone	2-HepO	99	114.2	VWR
2-Methyl-1-Propanol	2M1P	99	74.1	VWR
3-Methyl-1-Butanol	2M1B	99	88.1	VWR
1,2-Dimethylcyclohexane	1,2-DMCH	98	112.1	Sigma-Aldrich
Dimethylformaldehyde	DMF	99	73.1	VWR
Methyl isoButyl Ketone	MIBK	98	110.2	VWR

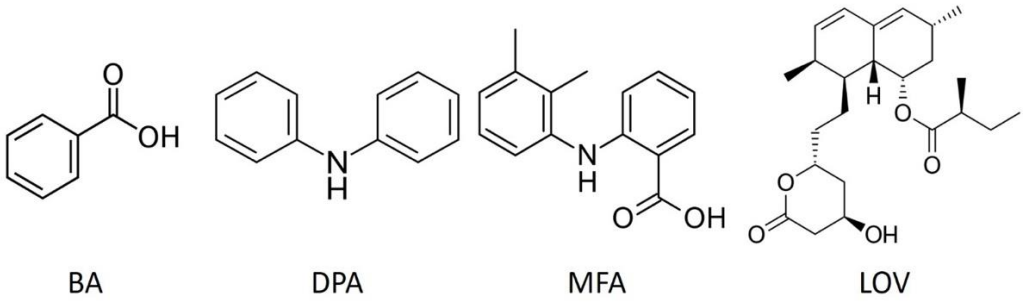

Figure 3-1: From left to right the model compounds Benzoic Acid (BA, MW=112.1g/mol), Diphenylamine (DPA, MW=169.2 g/mol) and Mefenamic Acid (MFA, MW=241.3 g/mol).

3.3.2 Solubility

Sample Preparation. A known amount of one of the crystalline materials was weighed into a 1.5 ml HPLC vial. 1 ml of a specific solvent was then pipetted into this pre-weighed vial containing the solid material and stirrer bar. This created a slurry of a specific concentration to be dissolved. The vial was then reweighed in

order to determine the exact mass of solvent added and therefore the exact molar composition of the solution being measured, with a balance error of 0.01 mg. Due to extremely high solubility of model compound in specific solvents, the amount of solvent added was reduced in some cases where the solubility is extremely high in the solvent system. For instance, with DPA in the acetate solvents.

The model compounds were not purified further. The solids were milled in order to create a fine powder for easy initial dissolution in the solubility measurement. This had no impact on polymorphic form.

The mol fraction *x* for each compound in the solvent can be calculated using the following expression:

$$x = \frac{{}^{m_2}/_{M_2}}{{}^{m_1}/_{M_1} + {}^{m_2}/_{M_2}} \qquad 52$$

Where m_1 and m_2 represent the mass of solvent and solid compound, respectively, and M_1 and M_2 are the specific molecular weights for the solvent and solid compound, respectively.

Solubility Measurement. The Crystal16 Multiple Reactor (Technobis Crystallization Systems, The Netherlands) was used to determine the saturation temperature for each prepared sample, similarly to the method utilized by Reus et al[71]. When solids are present in the vial, the transmission of light through the vial is hindered by the stirring suspension, whereas in the absence of particles the light passes unhindered. To dissolve the particles in the stirred (700-1000 rpm) suspension, a heating rate of 0.2 °C/min was applied up to a pre-set high temperature. Higher stirring speeds were used for systems where a high solid amount was present to promote dissolution. By cooling the solution (0.4 °C/min) to a pre-set low temperature, the solubility of the solute in the solution decreases and at some point, the sample recrystallized. Temperature was kept constant for 30 minutes at both the pre-set high and low temperatures to ensure adequate dissolution and recrystallization. For accuracy, three temperature cycles were performed, with an initial dissolution and recrystallization step for all samples

obtaining representative clear points. In all three temperature cycles the clear point temperature was determined as the temperature at which the transmission of light reached 100% compared to the calibrated transmission of the clear solution at the pre-set high temperature in the initial dissolution cycle. The average of the clear point temperatures was taken as the saturation temperature for the composition in the vial. To save measurement time the pre-set high and low temperatures were automatically adjusted using the clear and cloud point from the preceding cycle.

3.3.3 Solid Product Analysis

DSC. Differential Scanning Calorimetry (Polyma DSC 214, Netzsch) was carried out to determine the melting temperature T_m and heat of fusion ΔH_f for BA, DPA, MFA and LOV. A small amount (<5mg) of a specific compound is weighed into a metal DSC pan and sealed. A heating rate of 10 K/min from 298K up to 498K was used. The onset of the endotherm was taken as the melting temperature and the integrated endotherm was taken as the heat of fusion of the measured compound. In order to assess variation in melting temperature and heat of fusion measurements, 30 samples were measured resulting in an average and standard deviation value for each compound.

XRPD. X-ray powder diffraction (Bruker D8 Advance II, USA) was used to determine the polymorphic form of the supplied BA, DPA and MFA alongside the impact on purity of BA after grinding. The XRPD spectra was analysed over a 2θ range of 4 to 35° with a rate of 0.017°/sec.

3.4 Results

3.4.1 Solid Product and Thermal Sensitivity Analysis

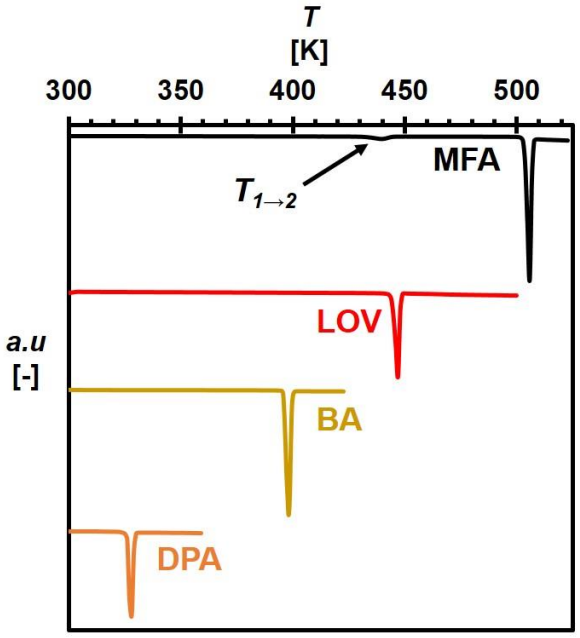

Figure 3-2: Typical DSC thermograms for all model compound used.

Table 3-2: The average heat of fusion ΔH_f and melting temperature T_m for LOV, DPA and BA from DSC measurements at 10 K/min, accompanied by the standard deviation of these measurements (N = 30).

Compound	T_m [K]	ΔH_f [kJ/mol]
LOV	443.7 ± 0.3	38.8 ± 2.1
DPA	326.17 ± 0.04	15.8 ± 0.4
BA	395.98 ± 0.04	18.6 ± 0.4

Typical results from the thermal analysis by Differential Scanning Calorimetry of DPA, MFA, BA and LOV are presented in Figure 3-2. All systems except MFA show a single endotherm with the average onset melting temperature T_m and heat of fusion ΔH_f presented in *Table 3-2*. From these systems, LOV observed the highest ΔH_f of 38.8 kJ/mol and T_m of 444 K, with it followed by BA at 18.6 kJ/mol and 396

K respectively. DPA has lowest ΔH_f and T_m at 15.8 kJ/mol and 326 K respectively The obtained values are similar to those from literature[67,72,73]. For MFA, a small solid phase transition is present at around $T_{1\rightarrow2}$ = 438 K as shown in Figure 3-2. This is the transition of the stable form 1 to the metastable form 2, as MFA is known to be polymorphic, undergoing a transition at higher temperatures in both dry air and in DMF[74,75]. Due to the polymorphic transition of MFA, heats of fusion and melting temperatures for the stable form 1 could not be obtained.

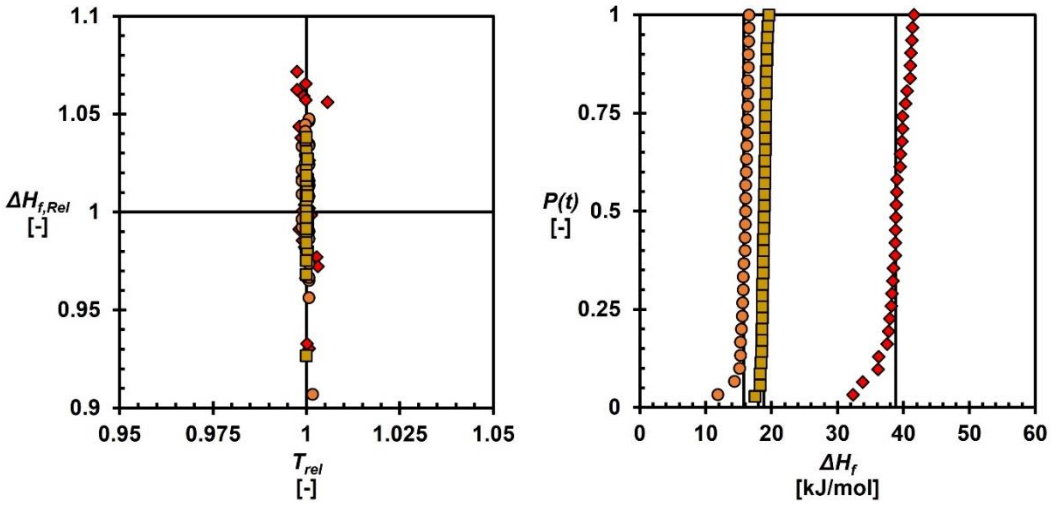

Figure 3-3: Variation in the characteristic values of heat of fusion ΔH_f and melting temperature T_m from DSC analysis for LOV (♦), DPA (●) and BA (■). For each compound 30 DSC measurements were performed. Left: The measurement values relative to the average heat of fusion and average melting temperature. Right: the probability distribution $P(\Delta H_f)$ for each compound. The solid black lines represent the average for each variable.

The 30 DSC measurements of DPA, BA and LOV show the variation in melting temperature T_m and heat of fusion ΔH_f. Figure 3-3 (left) shows the measured values relative to the average values of heat of fusion and melting temperature, where a value of 1 thus would indicate that the measurement value is equal to the average one. The variation in the melting temperature T_m of all these compounds is substantially less than 1°C, which is less than 0.5% of the average melting temperature in absolute temperature. The heat of fusion ΔH_f of DPA, BA and LOV, however, shows a larger variation having a standard deviation of 2.2% for BA and

2.5% for DPA to 5.2% for LOV. It is noted that the larger deviations mainly occur in the lower values as can be seen by the tail at small probabilities $P(\Delta H_f)$. These deviations generally come from a combination of inaccuracies such as small sample weight and peak integration. The obtained values of melting temperature and heat of fusion will be used to determine the ideal solubilities of these compounds

3.4.2 Experimental Solubility

Figure 3-4 shows the experimental solubility for each compound in the different solvents. The solubility of BA in each solvent from high to low at 30 °C is: DMF > EtOH > AcO > 2-BuO > PrOH > 2-BuOH > BuOH > 2M1P > 3M1B > 2-HepO > 1,2-DMCH. BA is significantly more soluble in DMF than in the other solvents at 1.56 g/g at 30 °C (0.003 K^{-1}). On the other hand, in 1,2-DMCH the solubility is significantly lower than the other solvents at only 0.019 g/g at the same temperature. All other solvents are similar in solvation effectiveness, showing solubilities of 0.29 to 0.6 g/g. A typical solubility in these solvents is that in 2-HepO, which is 0.29 g/g at 30 °C. At the same temperature, BA in the other ketones AcO and 2-BuO shows a larger solubility to that of the other solvents except EtOH with 0.57 g/g and 0.46 g/g respectively. EtOH shows the highest solubility of all alcohols and ketones at 0.64 g/g at 30 °C.

When comparing the results observed for DPA with those of BA, DPA is much more soluble in all solvents used, with it being significantly more soluble in the ketones than any other solvent groups. The order of DPA solubility at 30 °C is: AcO > 2-ButO > 2-HepO > EtOH > PrOH > 2-BuOH > 1-BuOH > 3M1B > 2M1P > 1,2-DMCH. Similar to BA, DPA in 1,2-DMCH has the lowest measured solubility of 0.31 g/g at 30 °C followed by 2M1P and 3M1P at 0.39 g/g and 0.41 g/g, respectively. The solvent AcO shows the highest solubility of 5.3 g/g at 30 °C, followed by its fellow ketones of 2-BuO and 2-HepO at 3.9 g/g and 2.4 g/g, respectively, at 30 °C. DPA in EtOH again shows the highest solubility of all alcohols at 1.2 g/g at 30 °C (0.0033 K^{-1}) followed by PrOH and 1-BuOH at 0.75 g/g and 0.58 g/g, respectively, at the same saturation temperature. When comparing to BA, the solubility of DPA in all alcohol solvents almost doubles.

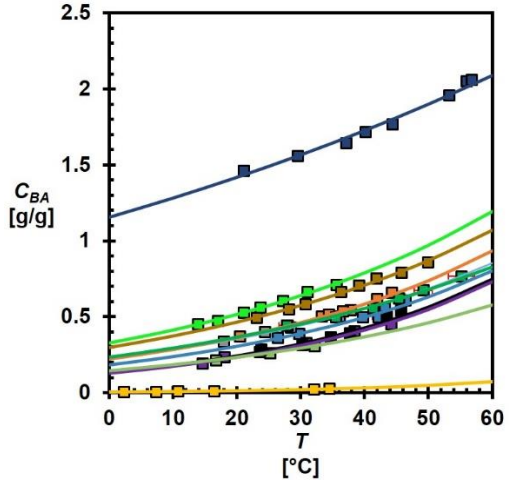
C_{BA} [g/g]
2.5
2
1.5
1
0.5
0
0 10 20 30 40 50 60
T [°C]

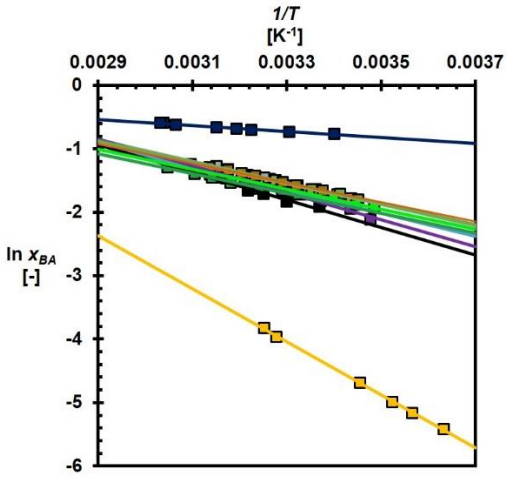
1/T [K-1]
0.0029 0.0031 0.0033 0.0035 0.0037
ln x_{BA} [-]
0
-1
-2
-3
-4
-5
-6

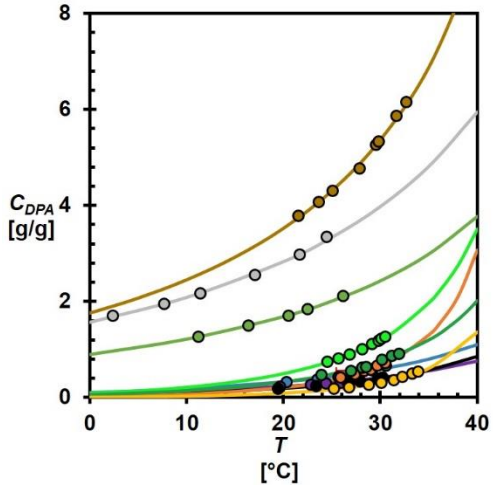
C_{DPA} [g/g]
8
6
4
2
0
0 10 20 30 40
T [°C]

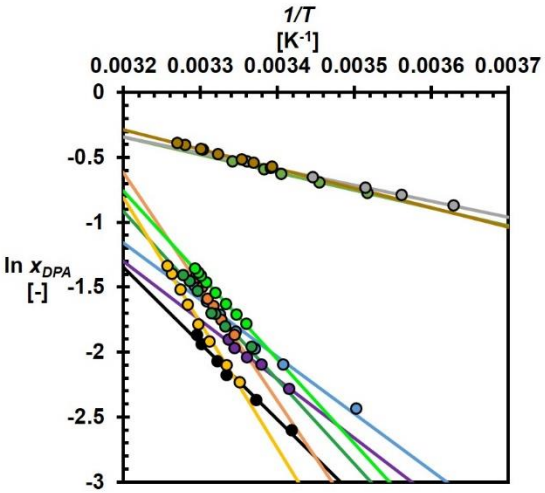
1/T [K-1]
0.0032 0.0033 0.0034 0.0035 0.0036 0.0037
ln x_{DPA} [-]
0
-0.5
-1
-1.5
-2
-2.5
-3

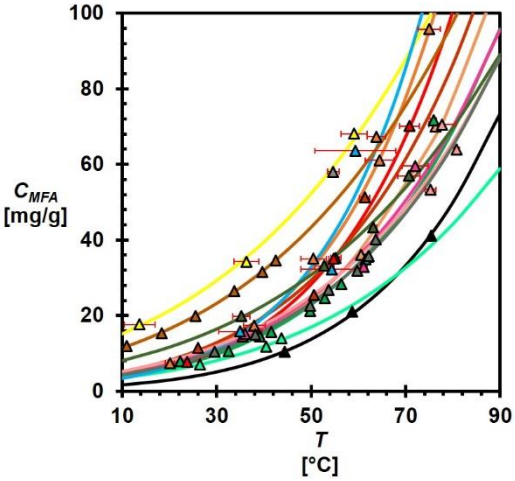
C_{MFA} [mg/g]
100
80
60
40
20
0
10 30 50 70 90
T [°C]

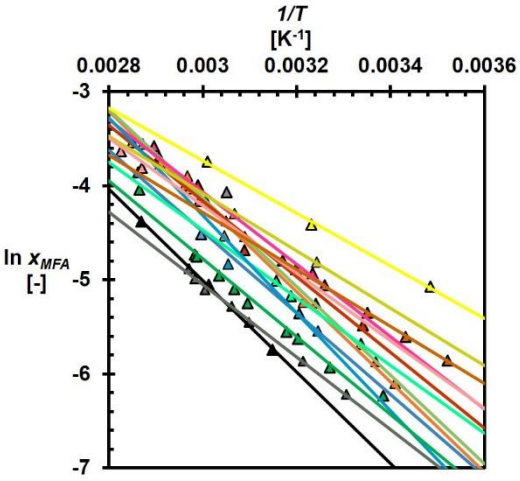
1/T [K-1]
0.0028 0.003 0.0032 0.0034 0.0036
ln x_{MFA} [-]
-3
-4
-5
-6
-7

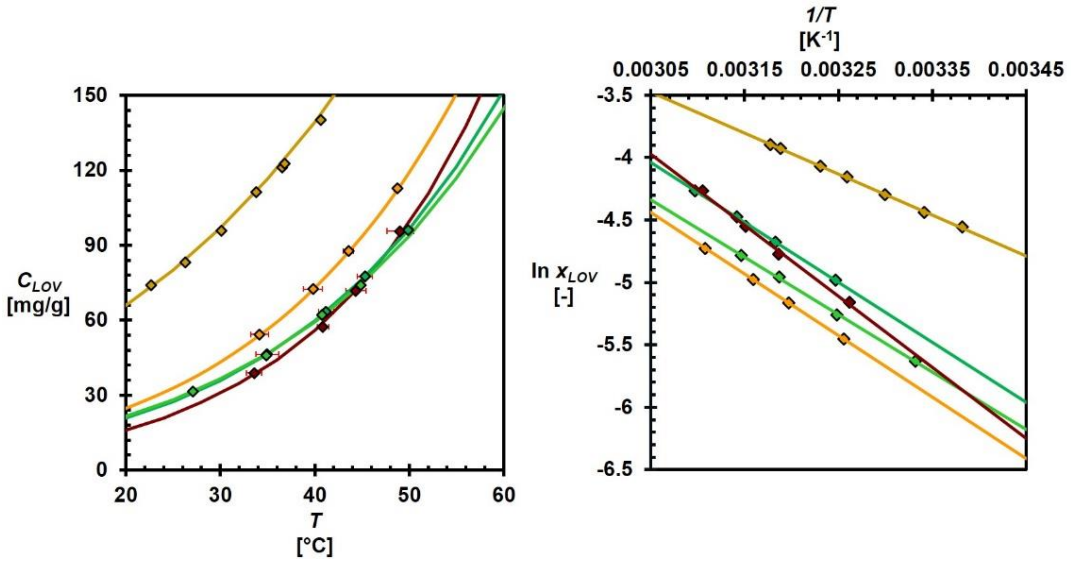

Figure 3-4: The solubility in mol fraction (left) and the van't Hoff plots (right) of Benzoic acid (■), Diphenylamine (●), Mefenamic acid (▲) and Lovastatin (♦) in the following solvents: MeOH (—), EtOH (—), PrOH (—), IPA (—), IPAc(—), BuOH (—), 2-BuOH (—), PeOH (—), AcO (—), EtAc (—), PrAC (—), BuAc (—), IBA (—), 2-BuO (—), 2-HepO (—), 2-PeO (—), 2M1P (—), 3M1B (—), 1,2-DMCH (—), DMF (—), MIBK (—). The solid line is the predicted solubility from the fit of the Van't Hoff correlation. The error bars for each system are marked by red caps —. In some cases, these error bars are within the marker and so are not observed visually.

MFA presents the lowest solubility in the measured solvents with no MFA-solvent combination obtaining a solubility above 0.01 g/g in the measured temperature range presented in Figure 3-4. The solvent order of solubility is: 2-PeO > AcO > MIBK > EtAc > PrAc > 2-BuOH > IPA > BuAc > 2-PenOH > EtOH > BuOH > PrOH > IBA > 2M1P. Like with the other systems, MFA has the largest measured solubility in solvents containing a ketone group, with MFA in 2-PeO giving the largest solubility of 29 mg/g at 30 °C (0.0033 K^{-1}) followed by AcO and MIBK at 23 and 16 mg/g at the same temperature. Although some ketones do experience a much lower solubility than its counter parts with IBA producing the lowest and 2nd lowest solubility out of the ketones and measured solvents respectively. For the

alcohols, the highest measured saturation concentration came from 2-BuOH at only 11 mg/g at 30 °C with 2-PenOH and EtOH following closely behind at 10.7 and 10.5 mg/g respectively.

LOV in its respective solvents show similar behaviour to that of the previous compounds, with the solubility order at 30 °C as follows: AcO > MeOH > EtOH > PrOH > IPA. The ketone AcO shows the highest solubility for LOV of 97 mg/g at 30°C . Of the alcohols, MeOH presents the highest solubility at 43 mg/g at 30 °C, followed by EtOH and PrOH at 36 mg/g and 35 mg/g respectively at the same temperature. The secondary alcohol IPA shows the lowest solubility of 30 mg/g at 30 °C. As the temperature increases, LOV in IPA shows a stronger temperature dependence than the other systems, with this dependence causing the system to have much higher solubilities than that of both EtOH and PrOH at $T \geq 48$ °C.

The raw data for each system is provided in the following publication[76].

3.4.3 Solubility Thermodynamic Models

Thermodynamic modelling of the experimental solubility allows for the interpolation and extrapolation of solubility data within any temperature range. For these extrapolations, Hildebrand proposed the following expression to describe the solubility of systems based on their solid-state thermal properties[77]:

$$\ln x = \ln x^{id}\gamma = \frac{\Delta H_f}{R}\left(\frac{1}{T_m} - \frac{1}{T}\right) - \frac{1}{RT}\int_{T_m}^{T} \Delta C_p \, dT + \frac{1}{R}\int_{T_m}^{T} \frac{\Delta C_p}{T} dT \qquad 53$$

With x, x^{id} and γ representing the experimental solubility, the ideal solubility and the activity coefficient of the compound respectively. ΔH_f (J/mol) and T_m (K) refer to the heat of fusion and melting temperature of the solute with R (J/molK) representing the gas constant. The term ΔC_p represents the difference in heat capacity between the solid and liquid phases of the compound. As the last two terms are generally significantly smaller than that of the term, the van 't Hoff equation provides solubility prediction with a minor loss of accuracy:

$$\ln x = \ln x^{id}\gamma = \frac{\Delta H_f}{R}\left(\frac{1}{T_m} - \frac{1}{T}\right) \qquad 54$$

The ideal molar fraction solubility x^{id} is obtained when heat of fusion and melting temperature are known and the activity coefficient is set to γ=1:

$$\ln x^{id} = \frac{\Delta H_f}{R}\left(\frac{1}{T_m} - \frac{1}{T}\right) \qquad 55$$

Often, the parameters $\Delta H_f = \Delta H_d$ and $T_m = T_o$ are used as fitting parameters for the mole fraction solubility x:

$$\ln x = \frac{\Delta H_d}{R}\left(\frac{1}{T_0} - \frac{1}{T}\right) \qquad 56$$

The van't Hoff proposes a linear relationship between the natural logarithm of the mol fraction and the inverse of the saturation temperature:

$$\ln x = \frac{A}{T} + B \qquad 57$$

With $A = \frac{\Delta H_d}{R}$ and $B = \frac{\Delta H_d}{RT_0}$ being fitting parameters. This equation often describes solubilities of organic compounds in organic solvents quite well.

To obtain the regressed constants for the Van't Hoff correlation, the experimental solubility data was plotted utilising Equation 54 in Figure 3-4 for BA (■), DPA (●), LOV (♦) and MFA (▲). The van't Hoff plot for each system is provided alongside the temperature-dependent solubility in Figure 3-4 with the obtained fitting parameters provided in Table 3-3.

Each system presents a highly negative gradient (parameter *A*) highlighting the strong temperature dependence of the solubility for all compounds. For BA, the 1,2-DMCH and DMF show the highest and lowest temperature dependence, respectively, with the remaining BA-solvent systems showing intermediate dependence. Switching from units of mg/ml to mole fraction for the solubility changes the solubility order as can be seen in Figure 3-4. The ketones show the highest solubility for BA between the alcohol and ketones, with the solvent AcO showing the highest solubility for BA followed by 2HepO. For alcohols, EtOH shows the highest mol fraction solubility of the alcohols with the lowest mol fraction solubility for BA being in 2M1P.

Table 3-3: Solubility Correlation Models (Van 't Hoff, Apelblat and Buchowski-Ksaizaczak) for BA, DPA, MFA and LOV in each solvent listed.

			Van't Hoff		Apelblat			Buchowski-Ksaizaczak	
Compound	Solvent	N	A [-]	B [-]	a [-]	b [-]	c [-]	λ [-]	h [J/mol]
Benzoic Acid (BA)	EtOH	7	-1579	3.6	-13	350	2	0.37	3270
	PrOH	6	-1564	3.5	-81	3471	12	0.22	4025
	BuOH	6	-1814	4.3	-269	11990	40	0.57	2803
	2-BuOH	4	-1603	3.7	16	-968	-2.2	0.44	2853
	AcO	8	-1523	3.5	-5.4	-48	1.	0.31	3160
	2-BuO	8	-1706	4.1	-73	3017	11	0.58	2544
	2-HepO	4	-1653	3.9	-6.5	27	1.2	0.54	2626
	3M1B	6	-2118	5.3	-1.9	-226	0.5	0.81	2434
	2M1P	6	-2165	5.3	-216	9502	32	1.1	2242
	1,2-DMCH	6	-4185	9.8	-14	579	2.1	10	829
	DMF	8	-467	0.81	-44	1851	6.7	-0.5	2767

			σ [%]		
Compound	Solvent	N	Van't Hoff	Apelblat	Buchowski-Ksaizaczak
Benzoic Acid (BA)	EtOH	7	1.0	0.93	1.1
	PrOH	6	1.5	0.7	1.1
	BuOH	6	3.2	2.3	3.2
	2-BuOH	4	1.2	0.53	1.3
	AcO	8	0.95	0.64	1.2
	2-BuO	8	0.88	0.68	0.79
	2-HepO	4	1.5	1.4	1.5
	3M1B	6	3.5	2.2	3.5
	2M1P	6	3.8	1.1	3.8
	1,2-DMCH	6	1.5	1.4	57
	DMF	8	0.93	0.3	0.36

			Van't Hoff		Apelblat			Buchowski-Ksaizaczak	
Compound	Solvent	N	A [-]	B [-]	a [-]	b [-]	c [-]	λ [-]	h [J/mol]
Diphenylamine (DPA)	EtOH	8	-6474	20.0	-1052	46050	158	1.29	5323
	PrOH	7	-6478	19.8	-1269	55930	190	1.0	6595
	BuOH	7	-4391	12.9	-455	19460	68	0.4	9874
	2-BuOH	6	-8799	27.5	-2104	93070	314	10	1502
	AcO	8	-1502	4.5	-275	11550	41.98	0.12	2259
	2-BuO	6	-1242	3.6	-113.7	4386	17.47	0.07	2337
	2-HepO	5	-1372	4.05	-136.1	5357	20.83	0.07	2483
	3M1B	5	-4547	13.3	-186.1	7766	28.11	0.25	13300
	2M1P	6	-5873	17.4	-563.1	24520	84.42	0.43	12520
	1,2-DMCH	8	-9646	30.1	-1860	82460	277.9	2.7	4221

			σ [%]		
Compound	Solvent	N	Van't Hoff	Apelblat	Buchowski-Ksaizaczak
Diphenylamine (DPA)	EtOH	8	0.62	0.32	0.66
	PrOH	7	2.9	1.6	2.9
	BuOH	7	6.1	1.6	4.9
	2-BuOH	6	1.3	0.78	6.7
	AcO	8	0.35	0.2	0.25
	2-BuO	6	0.58	0.26	0.23
	2-HepO	5	0.31	0.15	0.15
	3M1B	5	1.4	1.4	1.4
	2M1P	6	3.3	1.8	2.9
	1,2-DMCH	8	3	0.7	3.5

			Van't Hoff		Apelblat			Buchowski-Ksaizaczak	
Compound	Solvent	N	A [-]	B [-]	a [-]	b [-]	c [-]	λ [-]	h [J/mol]
Mefenamic Acid (MFA)	EtOH	7	-3855	6.5	-34	1623	5.2	9.9	901
	PrOH	9	-4144	7.7	-10	457	1.5	9.96	1003
	BuOH	3	-4331	8.5	-16.05	739.1	2.384	9.8	992
	2-BuOH	7	-4800	10.2	-20	918	3.1	9.97	894
	2-PeOH	4	-4713	10.0	-14.06	624	2.1	9.9	898
	AcO	6	-3033	4.8	-3.4	140	0.52	9.9	748
	2-PeO	3	-2799	4.7	-8.6	364	1.3	9.9	787
	EtAc	3	-4025	7.9	-27	1245	4.1	9.9	847
	PrAc	3	-3592	6.6	-78	3640	11	9.9	991.5
	BuAc	3	-3846	7.5	-34	1623	5.2	9.9	901
	IPAc	3	-5166	11.7	-77	3640	11.53	9.7	862
	IBAc	3	-3599	6.3	-12	547.2	1.8	9.9	792
	2M1P	3	-4865	9.6	-8	365	1.2	9.9	1053
	MIBK	4	-3048	5.1	-12	540	1.8	9.9	897

			σ [%]		
Compound	Solvent	N	Van't Hoff	Apelblat	Buchowski-Ksaizaczak
Mefenamic Acid (MFA)	EtOH	7	21	2.9	33
	PrOH	9	14	2.7	39
	BuOH	3	5.5	4.9	41
	2-BuOH	7	16	8.2	24
	2-PeOH	4	1.3	1.9	38
	AcO	6	8.2	0.80	36
	2-PeO	3	3.8	0.56	58
	EtAc	3	23	0.11	28
	PrAc	3	12	15	14
	BuAc	3	16	0.038	37
	IPAc	3	30	0.064	27
	IBAc	3	12	2	24
	2M1P	3	2.7	0.3	37
	MIBK	4	3.6	2.2	40

			Van't Hoff		Apelblat			Buchowski-Ksaizaczak	
Compound	Solvent	N	A [-]	B [-]	a [-]	b [-]	c [-]	λ [-]	h [J/mol]
Lovastatin (LOV)	MeOH	4	-4926	10.582	-1.0	445	1.5	9.97	800
	EtOH	4	-5139	11.48	-8.4	366	1.3	9.96	770
	PrOH	4	-4799.4	10.6	-14	596	2.0	9.96	760
	IPA	4	-5697.8	13.408	-21.4	952.3	3.2	9.97	761
	AcO	8	-3385.9	6.8862	-12	509.2	1.8	9.96	653.9

			σ [%]		
Compound	Solvent	N	Van't Hoff	Apelblat	Buchowski-Ksaizaczak
Lovastatin (LOV)	MeOH	4	0.12	0.58	14
	EtOH	4	14	0.8	18
	PrOH	4	0.12	0.87	20
	IPA	4	1.6	1.7	12
	AcO	8	5.8	0.52	21

The solubility of DPA is much larger than that of BA for the same solvents. In the ketones, the solubility is significantly larger than that of the alcohols with the van't Hoffs presenting much higher mol fractions, although the alcohols present a much larger temperature dependence. Ketones are known to have a lower

temperature dependence in comparison to alcohols, with their solubilities and mol fraction solubilities much larger[78,77]. The ketones present similar mol fractions to one another, with the differences in molecular weight influencing their absolute solubility order in Figure 3-4(left). The alcohols present similar mol fractions to one another, with DPA-EtOH showing the highest mol fraction of x_{DPA} = 0.19 (T = 303K) and 2M1P showing the lowest at x_{DPA} = 0.16 at the same temperature.

MFA presents the lowest mol fraction solubilities in all solvents compared to the other compounds, with the ketones showing the highest mol fraction solubilities. The system of MFA and 2PeO shows the highest mol fraction solubility at x_{MFA} = 0.0103 followed by MIBK and AcO at x_{MFA} = 0.0068 and 0.0056 at 0.0033K^{-1} (T = 30 °C), respectively. Unlike previously the lower molecular weight solvents present the lowest mol fraction solubilities at 0.0033K^{-1} (T = 30 °C). The acetates and alcohols have similar temperature dependences with the acetates showing a slightly lower dependence as expected from previous examples and literature[79].

LOV shows a similar pattern to the previous molecules, with the ketone presenting a higher mol fraction at x_{LOV} = 0.014 at 303K (0.0033K^{-1}), with the temperature dependence lower than in the other alcohols according to its respective parameter A. LOV-PrOH presents the highest mol fraction of the alcohols with LOV-MeOH presenting the lowest at x_{LOV} = 0.0034 at 0.0033K^{-1} (T = 30 °C). The system of LOV and IPA shows high temperature dependence in comparison to its counterparts, changing the solvent order of the solubility with temperature.

The Apelblat and Buchowski-Ksaizaczak are effective thermodynamic models for extrapolating and correlating solubility data for solid–liquid equilibrium systems. The semi-empirical Apelblat equation is represented through the equation:

$$\ln x = \frac{a}{T} + b + c \ln(T) \qquad 58$$

With the empirical constants *a* and *b* accounting for the effect of the enthalpy of dissolution on the mole fraction, and *c* accounting for differences in heat capacity of the solid and liquefied solute at the solution temperature T[80].

Buchowski proposed another two-parameter model as a correction to the Van't Hoff equation to extrapolate experimental solubility data at specific temperatures:

$$ln\left(1+\frac{\lambda(1-x_2)}{x_2}\right)=\lambda h\left(\frac{1}{T}-\frac{1}{T_m}\right) \qquad 59$$

For all three thermodynamic models, the parameters obtained from each fitting are provided in Table 3-3.

The relative standard deviation σ for each system can be determined from the following[81]:

$$\sigma = 100 * \sqrt{\frac{1}{(N-1)}\sum_{i=1}^{N}\left(\frac{x_2 - x_2^{pred}}{x_2}\right)^2} \qquad 60$$

With it determining the relative average deviation in percentage %, of the experimentally measured mole fraction solubilities x_2 from the mol fraction solubilities x_2^{pred} described with the model, with N being the number of measurements.

For BA, the Apelblat equation produces the lowest σ when compared to the other models, with the van't Hoff equation providing very similar values for all systems. For the majority of BA-solvent systems measured, the Buchowski equation produces similar values to the other models although for 1,2-DMCH it shows extremely large variation. This could be due to the small solubility of BA in 1,2-DMCH and so slight deviation impacts the comparison to a larger amount. Like for BA, the Apelblat equation provides the best σ compared to the other models used. Unlike previously, the van't Hoff shows much larger variation between the measured and predicted values, with the acetates showing the lowest σ. Like previously the lower solubility of this compound in the different solvents would impact the σ to a greater degree than it would for the acetates where better σ are

observed. The lower number of points used for the MFA-solvent systems show significant impact on the σ when compared to the previous model compounds. The Apelblat shows the lowest σ like previously with the Van't Hoff being the next best, although to a much lesser degree. The Buchowski model shows its reduced capability to model LOV compared to the other models, with it showing the highest σ. This again could be due to the lower solubility of MFA so the difference in measured and predicted values provides a larger error. The Apelblat once again shows the best predictive capability. The van't Hoff showing good agreement with the measured values for all except EtOH.

The extent of non-ideality of the systems can be shown by comparing the experimentally determined heat of fusion ΔH_f and melting temperature T_m from Table 3-2 to the heat of dissolution ΔH_d and temperature T_0 obtained from the fitting procedure with equation 56. This is shown in Figure 3-5.

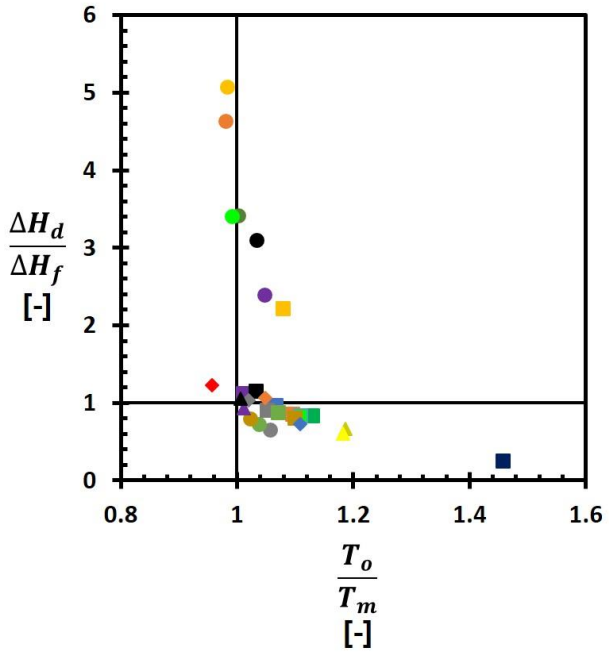

Figure 3-5: Deviations from ideality for each compound-solvent system, based on the ratio $\Delta H_d/\Delta H_f$ of the heat of dissolution and heat of fusion and the ratio of temperature T_0 and melting temperatures T_m. The markers represent the specific model compound Benzoic acid - BA (■), Diphenylamine – DPA (●), Mefenamic acid – MFA (▲) or Lovastatin - LOV (♦), while the colours represent the specific solvent: MeOH (—), EtOH (—), PrOH (—), IPA (—), IPAc(—), BuOH

(—), 2-BuOH (—), PeOH (—), AcO (—), EtAc (—), PrAC (—), BuAc (—), IBA (—), 2-BuO (—), 2-HepO (—), 2-PeO (—), 2M1P (—), 3M1B (—), 1,2-DMCH (—), DMF (—), MIBK (—). The solid lines denote the ideal behavior values for each ratio and a system in the point (1,1) would behave ideal.

For BA, the majority of systems are situated around 1, showing the compound-solvent systems often behave close to ideal. The system BA-DMF shows the highest non-ideality from every other BA-solvent system. The deviation from ideality is due to both disparity in the heat of dissolution ($\frac{\Delta H_d}{\Delta H_f} = 0.24$), as well as a more prevalent difference in T_m and T_o ($\frac{T_0}{T_m} = 1.46$). For DPA, the value of $\frac{T_0}{T_m}$ for a number of systems like 1,2DMCH ($\frac{T_0}{T_m} = 0.98$) and 2-BuO ($\frac{T_0}{T_m} = 1.06$) only slightly deviates from 1 so closely agreeing with ideality, while a much larger variation is seen in the ratio $\frac{\Delta H_d}{\Delta H_f}$. DPA in 1,2-DMCH shows the highest ratio of $\frac{\Delta H_d}{\Delta H_f}$ followed by 2-BuOH while these systems show the lowest solubility of DPA. Both LOV and MFA show a similar degree of non-ideality with most of each solute-solvent system structured around (1,1) so close resemblance to ideality. MFA in the ketones shows slightly greater non-ideality than the other MFA-solvent systems with this decreasing towards ideality at decreasing solubility. The error identified from the determination of the T_m and ΔH_f is much lower than the variation observed from ideality for the systems so identifying the deviations are significant.

3.4.4 Activity Coefficient Modelling

Through a determination of the activity coefficient for each system in its respective solvent, a perspective of the interactions influencing the solubilities is provided. The activity coefficient is a quantitative method to analyse the deviation from ideality due to molecular interactions present in the system, so providing a method to deduce specific solvent types for further solvent selection. Equation 53 gives a relation between the activity coefficient γ and the ideal and the measured solubilities:

$$\ln \gamma = \ln x - \ln x^{id} \qquad 61$$

Equation 61 can be rearranged to obtain the activity coefficient γ:

$$\gamma = \frac{x}{x^{id}} \qquad 62$$

Thus, the activity coefficient γ can be determined from a solubility measurement point at a particular temperature.

The calculated activity coefficients ln γ for all measured samples are provided in Figure 3-6. For BA, the order of activity coefficients at 303K from smallest to largest is as follows: DMF > AcO > 2-BuO > 2-HepO > 2-BuOH > EtOH > BuOH > 3M1B > PrOH > 2M1P > 1,2-DMCH. For BA in 1,2-DMCH, its low solubility is represented through a highly positive activity coefficient at 30 °C, whereas for DMF a highly negative activity coefficient is observed. For the other solvents at 303 K, the measured γ_{BA} distribute themselves around a γ_{BA} =1 (ln γ_{BA} = 0) showing close-to-ideal behaviour.

For DPA in the same solvents, the alcohols had $\gamma_{DPA} > \gamma_{BA}$ whereas the ketone's go from non-ideal towards ideal at increasing *T*. The order of activity coefficient in decreasing order of magnitude is similar to that previously although now 1,2-DMCH has a slightly lower γ_{DPA} than that of 3M1B, with a γ_{DPA} = 3.54 (ln γ_{DPA} =1.27) and γ_{DPA} = 3.55 (ln γ_{DPA} =1.26) respectively at 303K. For DPA the ketones position themselves close to ideality, with AcO slightly negative at 303K. EtOH and PrOH both have positive deviations from ideality with γ_{DPA} = 2.4 (ln γ_{DPA} = 0.89) and 2.9 (ln γ_{DPA} =1.1) respectively at 30 °C. At increasing temperatures, the activity coefficient for all systems go towards ideality as described by equation 55.

MFA experiences the most significant negative non-ideality with the solvents used in this study, with the majority of experimental values observing a ln γ < 0. 2M1P was the only solvent in which all the γ_{MFA} was above 1 at all measured temperature ranges with a γ_{MFA} = 1.4 (ln γ_{MFA} =0.33) at 30 °C. Like for DPA and BA excluding DMF, the ketones produced the lowest of the measured γ_{MFA} with 2-PeO. Although from Figure 3-6, MFA in 2-BuO produces an experimental γ_{MFA} = 0.41 (ln γ_{MFA} =-1.1) at 54 °C, proper conclusions at 30 °C are not possible due to the lack of experimental points. BuOH and PrOH obtain a γ_{MFA} = 0.72 (ln γ_{MFA} =-

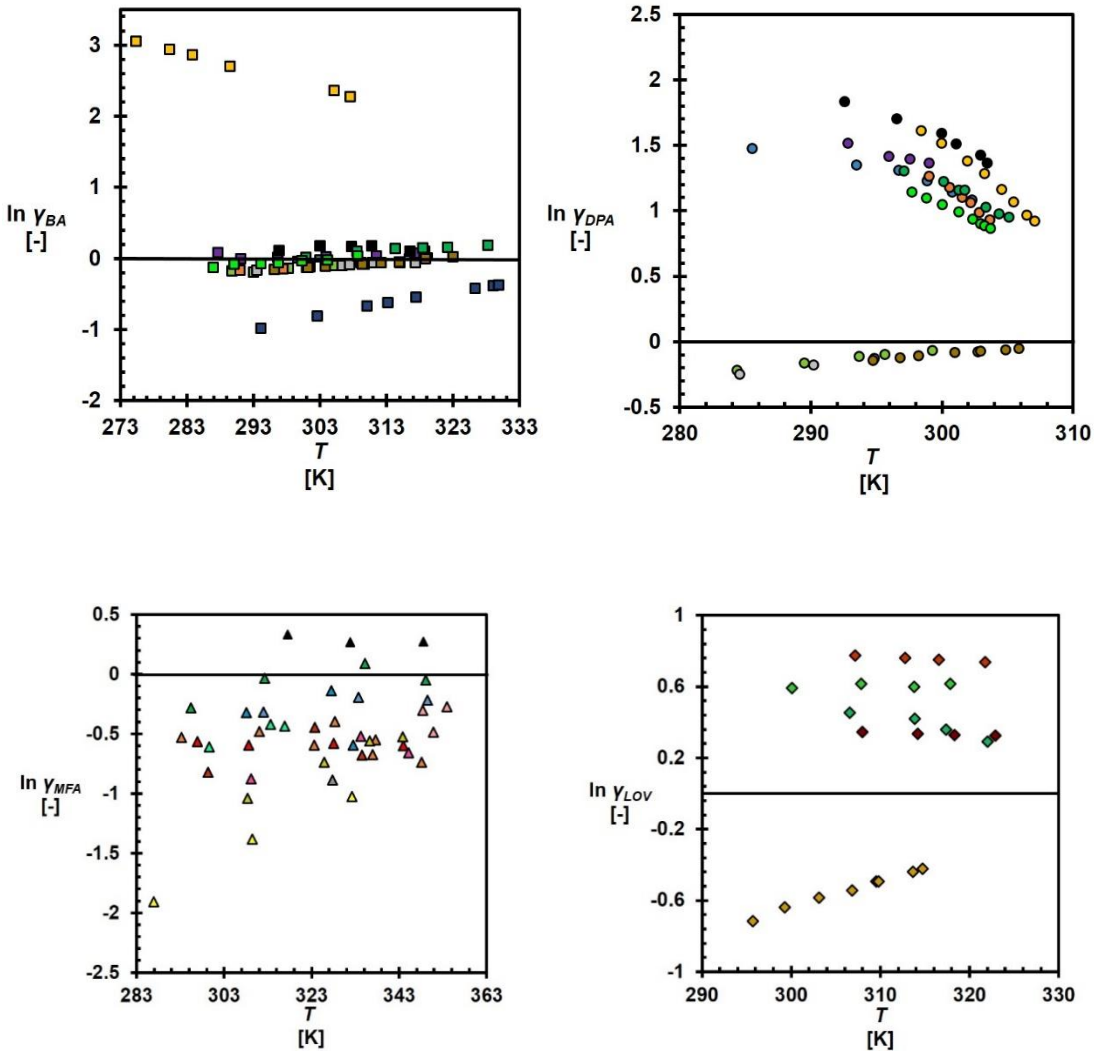

Figure 3-6: Experimental activity coefficients for Benzoic acid (■), Diphenylamine (●), Mefenamic acid (▲) and Lovastatin (♦) in the following solvents: MeOH (—), EtOH (—), PrOH (—), IPA (—), IPAc(—), BuOH (—), 2-BuOH (—), PeOH (—), AcO (—), EtAc (—), PrAC (—), BuAc (—), IBA (—), 2-BuO (—), 2-HepO (—), 2-PeO (—), 2M1P (—), 3M1B (—), 1,2-DMCH (—), DMF (—), MIBK (—).

0.33) and γ_{MFA} = 0.85 (ln γ_{MFA} =-0.16) at 303 K respectively, with the γ_{MFA} of both these solvents increasing towards ideality at increasing temperatures.

For LOV, all systems show a highly non-ideal behaviour, with the alcohols showing a positive deviation with the magnitude decreasing at increasing chain length. Whereas LOV in AcO shows a highly negative non-ideal behaviour,

reducing as the temperature increases towards T_m. Although IPA has a similar functional groups to that of PrOH, IPA observes a different γ_{LOV} greater temperature dependence to that of PrOH, causing it to observe an ideal nature at a lower temperature than would be expected from Equation 55.

Activity coefficient modelling offers a more thermodynamically rigorous approach to investigating molecular interactions between the solute and solvent than the empirical approach applied from the solubility models. Provided in Table 3-4 is the regressed adjustable parameters of three activity coefficient models: Margules, Van Laar and Wilson, to the experimentally determined activity coefficients for each solute-solvent system presented in this work. The Margules equation provides a simple yet comprehensive two-constant relation between the mole fraction solubility of a given solute-solvent system and the measured activity coefficient from Equation 62 for molecules which differ significantly in molecular volume[16]:

$$\ln \gamma_2 = x_1^2\big(A_{12} + 2x_2(A_{21} - A_{12})\big) \qquad 63$$

With x_2 and γ_2 representing the mole fraction and subsequent activity coefficient of the solute in a specific solvent system, and x_1 the reciprocal mole fraction of solvent within this same system. A_{12} and A_{21} are the two regressed constants obtained from the fitting to all experimental data for each solvent system. This detail the interaction of solute (2) and solvent (1) molecules and their respective influence on the activity coefficient.

For BA in all systems where a $\gamma < 1$, $A_{21} < 0$. This observation suggests these systems present a higher favourability of hydrogen bonding interactions between molecules to occur, reducing to $\gamma < 1$[82]. For the BA-solvent systems which present $A_{21} < 0$, A_{12} presents a highly positive value with this increasing while A_{21} decreases. This constant is consistent with the degree of non-ideality presented by a system, with a more positive value resembling a larger degree of non-ideality. This degree of variation is also shown significantly for BA-1,2DMCH with it being the only BA system showing a $A_{21} > 0$ and respective $\gamma_{BA} > 1$ across all measured temperatures, so showing a $A_{21} << 0$.

Table 3-4: Regressed coefficients from the Margules, Van Laar and Wilson activity coefficient models for BA, DPA, LOV and MFA in each of its respective solvent systems, alongside their σ determined from Equation 60.

			Margules		Van Laar		Wilson					σ [%]		
Compound	Solvent	N	A_{12} [-]	A_{21} [-]	C [-]	D [-]	λ_{12} [kJ/mol]	λ_{21} [kJ/mol]	Compound	Solvent	N	Margules	Van Laar	Wilson
Benzoic Acid (BA)	EtOH	7	0.70	-0.63	-1166	-83300	-0.12	-0.075	Benzoic Acid (BA)	EtOH	7	0.49	2.0	4.6
	PrOH	6	0.74	-0.46	4755	157	2.6	-3.2		PrOH	6	2.3	6.8	3.1
	BuOH	6	0.17	-0.25	-195	2201	-0.10	-0.10		BuOH	6	4.0	4.1	4.6
	2-BuOH	4	0.40	-0.68	-545	-4172	-0.54	-0.21		2-BuOH	4	1.5	1.9	3.6
	AcO	8	0.43	-0.75	828	-2.59E+04	-1.9	3.3		AcO	8	1.3	2.2	4.4
	2-BuO	8	0.20	-0.53	-764	-1.20E+04	-2.4	3.7		2-BuO	8	2.7	2.7	2.8
	2-HepO	4	0.27	-0.63	-659	-1110	-0.56	-0.16		2-HepO	4	2.0	2.6	2.8
	3M1B	6	0.036	-0.094	-115	-174	-0.11	-0.011		3M1B	6	3.4	3.4	3.4
	2M1P	6	0.0011	0.14	233	296.9	0.027	0.346		2M1P	6	3.5	3.5	3.5
	1,2-DMCH	6	-17	3.1	1281	7044	-1.6	9.1		1,2-DMCH	6	4.9	2.1	1.4
	DMF	8	-0.77	-5.8	-6760	1.80E+04	-6.2	-1.2		DMF	8	3.8	8.1	9.9

			Margules		Van Laar		Wilson					σ [%]		
Compound	Solvent	N	A_{12} [-]	A_{21} [-]	C [-]	D [-]	λ_{12} [kJ/mol]	λ_{21} [kJ/mol]	Compound	Solvent	N	Margules	Van Laar	Wilson
Diphenylamine (DPA)	EtOH	8	0.62	1.9	3888	4685	5.0	1.2	Diphenylamine (DPA)	EtOH	8	0.16	0.12	0.054
	PrOH	7	0.60	2.0	4054	4960	4.7	2.0		PrOH	7	0.29	0.61	0.014
	BuOH	7	0.58	2.0	4396	4643	4.9	1.8		BuOH	7	0.10	1.2	0.73
	2-BuOH	6	0.50	2.1	3666	5333	3.5	3.4		2-BuOH	6	0.30	0.21	0.0094
	AcO	8	-0.17	-0.66	-0.0044	0.47	0	0		AcO	8	0.052	2.7	1.3
	2-BuO	6	-0.20	-1.1	0.02	0.98	-0.58	-0.37		2-BuO	6	0.44	12	1.6
	2-HepO	5	-0.098	-0.80	-453	1147	-0.27	-0.111		2-HepO	5	0.16	2.6	1.7
	3M1B	5	0.41	2.2	4272	5058	4.5	2.7		3M1B	5	0.016	0.72	0.12
	2M1P	6	-0.027	2.4	3873	5917	4.4	3.8		2M1P	6	0.39	0.44	1.7
	1,2-DMCH	8	0.36	2.3	3791	5872	2.7	5.0		1,2-DMCH	8	1.3	0.96	0.15

			Margules		Van Laar		Wilson					σ [%]		
Compound	Solvent	N	A_{12} [-]	A_{21} [-]	C [-]	D [-]	λ_{12} [kJ/mol]	λ_{21} [kJ/mol]	Compound	Solvent	N	Margules	Van Laar	Wilson
Mefenamic Acid (MFA)	EtOH	7	-2.4	0.33	4111	593	34	-5.2	Mefenamic Acid (MFA)	EtOH	7	2.7	12	3.2
	PrOH	9	2.9	-0.034	20	2.8	7.3	-4.7		PrOH	9	10	10	7.9
	BuOH	3	2.2	-0.31	-83	-826	0.13	-0.019		BuOH	3	6.1	4.5	6.6
	2-BuOH	7	-4.8	-0.45	5.3	-193	0.12	-0.025		2-BuOH	7	7.7	34	14
	2-PeOH	4	-1.5	-0.57	-8106	-1551	0.38	-1.7		2-PeOH	4	1.4	5.3	5.5
	AcO	6	48	-1.5	3326	-2340	-0.33	0.047		AcO	6	3.6	18	19
	2-PeO	3	19	-2.0	3479	-3433	-2.6	4.7		2-PeO	3	13	34	19
	EtAc	3	1.2	-0.68	-3640	-1704	-1.9	4.6		EtAc	3	19	17	16
	PrAc	3	-11	0.20	14	-253	-0.051	-0.59		PrAc	3	8.4	7.2	11
	BuAc	3	2.6	-0.81	2247	-1809	-3.1	6.9		BuAc	3	16	15	10
	IPAc	3	-12	-0.12	-3345	-897	0.073	-0.65		IPAc	3	16	22	22
	IBAc	3	27.58	-0.79	-34	-2249	-3.0	7.1		IBAc	3	3.8	3.0	5.4
	2M1P	3	-2.37	0.33	137	872	-0.059	-0.029		2M1P	3	2.4	2.2	2.0
	MIBK	4	14.37	-1.2	-136	-4016	-2.66	5.3		MIBK	4	8.1	4.1	14

Compound	Solvent	N	Margules A_{12} [-]	Margules A_{21} [-]	Van Laar A [-]	Van Laar B [-]	Wilson λ_{12} [kJ/mol]	Wilson λ_{21} [kJ/mol]
Lovastatin (LOV)	MeOH	4	-3.8	0.82	1358	2018	5.5	-3.5
	EtOH	4	2.3	0.59	18267	1558	6.1	-4.1
	PrOH	4	-0.96	0.36	1111	889	3.9	-3.1
	IPA	4	-10	0.59	54.9	1632	1.1	2.2
	AcO	8	13	-0.98	-95.9	-3156	9.3	-7.5

Compound	Solvent	N	σ [%] Margules	Van Laar	Wilson
Lovastatin (LOV)	MeOH	4	0.50	0.47	0.5
	EtOH	4	0.65	1.79	0.6
	PrOH	4	0.19	0.12	0.013
	IPA	4	1.1	1.1	0.05
	AcO	8	1.47	0.91	4.3

When applying similar regression to DPA, the same phenomena is shown with only the ketones obtaining a $A_{21} < 0$ corresponding to the $\gamma < 1$ that is obtained from Equation 62. The propensity for hydrogen bonding decreases at increasing chain length from A_{21}, with A_{12} moving towards zero showing an increasing degree away from ideality. The magnitude of A_{12} for the ketones shows they are significantly close to ideality much like was observed for BA-3M1B. For LOV, LOV-AcO observes a highly negative non-ideal behaviour from both $A_{12} \gg 0$ and $A_{21} < 0$. The other alcohol systems present $A_{21} > 0$ with all these systems presenting a $\gamma > 1$ and so showing a reduced propensity of hydrogen bonding. For MFA, all systems except EtOH, PrAc and 2M1P present $A_{21} > 0$ with these systems presenting a lower propensity for hydrogen bonding between the solute-solvent systems and so $\gamma_{LOV} > 1$. The ketones present the lowest A_{21} with PeO showing the highest propensity for hydrogen bonding with MFA, followed by AcO.

To counteract the limitations of the Margules equation to describe systems that have highly dissimilar molecules and so dissimilar interaction energies, Van Laar proposed an alternative equation[16]:

$$\ln \gamma = \frac{D}{RT\left(1 + \frac{D}{C x_1}\right)^2} \qquad 64$$

With x_1 and x_2 representing the mole fraction of the solute and solvent respectively. C and D are the two constants obtained from regression of the experimental activity coefficients with the Van Laar equation. For BA, the Van Laar predicts systems with a lower accuracy in most cases, although some systems like 3M1B observe a similar σ. For 1,2-DMCH it predicts better than the Margules. Simialrly to BA, the Van Laar observes poorer fitting when compared

to the Margules in most cases. Its largest σ is observed for systems close to ideal like 2-BuO although similar to BA, 1,2-DMCH has a lower error then the Margules. This same phenomenon for larger errors than the Margules is again seen in the MFA and LOV systems, with some being slightly lower. Van Laar predicts systems that have activity coefficients less than 1, with the Margules doing better in systems closer to ideal.

Despite the flexibility and simplicity of both the Margules and Van Laar to fit and correlate experimental data, their inability to predict highly non-ideal systems reduces its effectiveness to distinguish interactions within a system[16]. As well as this, the parameters from these two models do not have a simple relation to molecular interactions. Wilson proposed the following two-parameter equation considering the temperature dependence of the excess free energy alongside the assumed non-random interaction between the individual components[83,84]:

$$\ln \gamma_2 = -\ln(x_2 + x_1\Lambda_{21}) + x_1\left(\frac{\Lambda_{12}}{x_1 + x_2\Lambda_{12}} - \frac{\Lambda_{21}}{x_2 + x_1\Lambda_{21}}\right) \quad 65$$

where:

$$\Lambda_{12} = \frac{v_2}{v_1}\exp\left(-\frac{\lambda_{12}}{RT}\right) \quad 66$$

$$\Lambda_{21} = \frac{v_1}{v_2}\exp\left(-\frac{\lambda_{21}}{RT}\right) \quad 67$$

The basis of the Wilson equation is that there is a local contraction of molecules centred together due to intermolecular interactions, so Λ_{12} and Λ_{21} represent the binary interaction parameters between the two different components in the system. The interaction energy between the two constituent components is represented through λ_{12} and λ_{21} in J/molK, with these parameters obtained from regression analysis against experimental activity coefficient γ data at different temperatures T.

The Wilson equation is able to describe the activity coefficient for BA with significant agreement as shown in Figure 3-7. Also the σ for each system can be found in Table 3-4. From Figure 3-7, BA in DMF shows the least well described system with an σ = 9.9%. 1,2-DMCH observes the best fit from all measured

systems of BA with a σ = 1.4%. For Wilson predictions of systems with a γ < 1 and to a lesser extent γ ≈ 0, a relatively poor regression fits than that of γ > 1. This is due to the smaller relative magnitude of the interaction values compared to the relative error in experimental data.

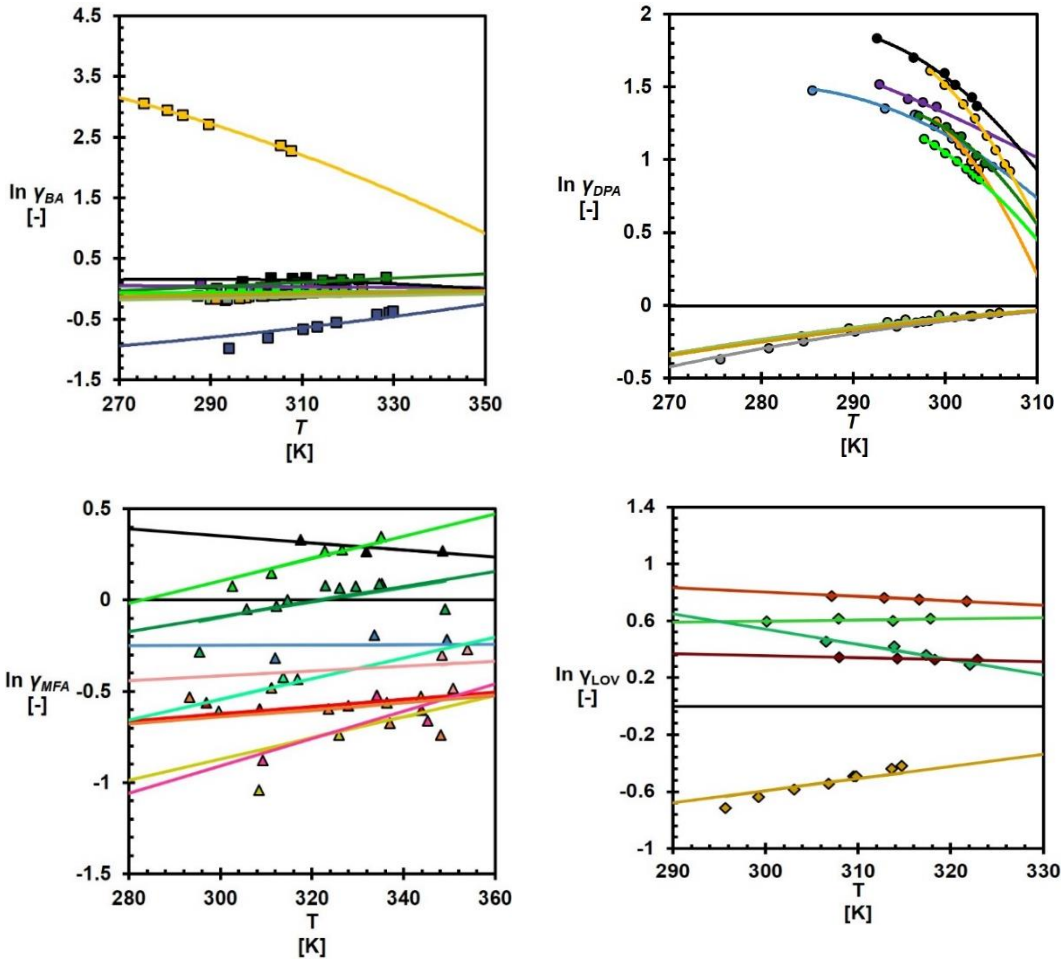

Figure 3-7: The predicted Wilson activity coefficients for BA (■), DPA (●), LOV (♦) and MFA (▲) in the solvent systems: MeOH (—), EtOH (—), PrOH (—), IPA (—), IPAc(—), BuOH (—), 2-BuOH (—), PeOH (—), AcO (—), EtAc (—), PrAC (—), BuAc (—), IBA (—), 2-BuO (—), 2-HepO (—), 2-PeO (—), 2M1P (—), 3M1B (—), 1,2-DMCH (—), DMF (—), MIBK (—).. The solid lines represent the best fit of the Wilson model. The markers represent the individual experimental activity coefficients obtained using Equation 62. For MFA, specific systems were removed due to observing a σ > 15% relative to the Wilson fitting procedure.

This analysis holds true for BA shown here. For all systems except PrOH, as the temperature increases the predicted activity coefficient tends towards 1 as is predicted from Equation 524 This increase at increasing temperatures is likely to due being so close to ideal. At the higher temperatures closer to the melting point of BA, these systems experience a non-linear path. This observation similarly agrees with Equation 54, with the activity coefficient going towards $\gamma \approx 1$ ($\ln \gamma_{BA} \approx 0$) and so having to compensate for its activities being higher at temperatures further away from the melting point. At these lower temperatures measured for all systems, a linear relationship between $\ln \gamma$ and T is observed. For the systems which are observed and predicted to have $\gamma \approx 1$ ($\ln \gamma_{BA} \approx 0$), temperature dependence stays relatively constant when compared to the DMF and 1,2-DMCH systems as these systems are already observing close to ideal behaviour and so an increase in temperature will have little impact on the change in activity of the system.

DPA shows the same trend observed for BA when applying the Wilson equation to experimental results. With systems that observe a $\gamma > 1$, the Wilson predicts a good fit according to its σs and resultant fitting, while systems like the ketones where $\gamma \leq 1$ present slightly worse fits and σs compared to the other systems. Although unlike previously, the σ is not as bad as previously observed with BA with likely due to a larger range of temperatures examined. As the melting point for DPA is much smaller than for BA, the non-linear relationship between $\ln \gamma_{DPA}$ and T is more significant with the linear relationship at lower temperatures adjusting to meet the assumption of Equation 54. The ketones experience a linear temperature dependence with little impact on the activity due to their proximity to ideality.

The systems for LOV that experience $\gamma > 1$ show good agreement with the predictions from the Wilson equation, with the LOV-PrOH system showing the lowest σ of these measured systems. Like for the previous systems, the ketone system LOV-AcO experiences the highest σ of all the measured systems for LOV with it also having a $\gamma < 1$ ($\ln \gamma_{LOV} < 0$). Like previously, the systems show a linear relationship between $\ln \gamma_{LOV}$ and T with the measured temperatures being much

lower than that of the melting point. The systems show slight temperature dependence with LOV-AcO showing the strongest change, which is uncommon when comparing ketone and alcohol systems. LOV-EtOH is the only system that experiences an increasing Wilson prediction at increasing temperatures with it also providing a small σ. This abnormal situation could be due to the limited temperature range used alongside a lack of temperature dependence.

Due to the lack of data points, systems with an σ > 15% for MFA have been removed from Figure 3-7, although their obtained interaction parameters have been retained in Table 3-4. For the majority of systems, they comply with Equation 54 with increasing temperatures producing γ towards 1 with this trend also represented from the Wilson predictions. Some systems like MFA-EtOH experience an increasing activity away from ideality at increasing temperatures with the respective Wilson prediction showing good agreement with the data due to its low σ. Some systems also produce a flat activity prediction with no temperature dependence at increasing temperatures, although this is likely due to the lack of experimental data. Also due to the inability to determine actual heats of melting and melting temperatures for MFA, the literature used could cause the largest error and so produce unexpected results.

3.5 Discussion

The data in this work was used to determine functional group parameters within SAFT-gamma Mie to enhance solubility predictions for Mefenamic Acid. SAFT-gamma Mie requires the use of the melting point and heat of fusion for the model compound being predicted, similar to the models used here. Due to the transformation of MFA to form 2 on standard heating, accurate values could not be obtained for the form 1. By determining the solubility of BA and DPA in a large number of solvents, the molecular interactions specific to functional groups in MFA were able to be modelled allowing better general predictive capabilities for SAFT-gamma Mie.

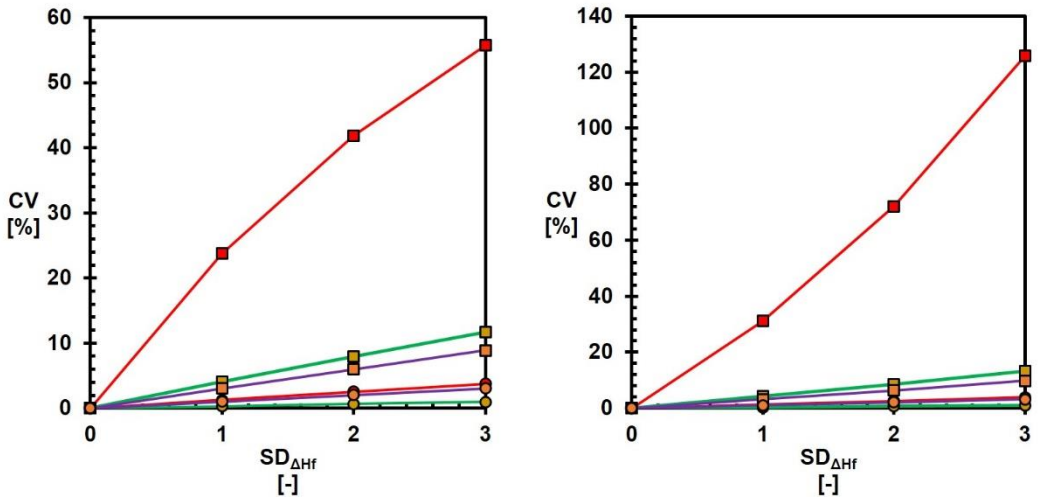

Figure 3-8: The variation of the ideal solubility obtained from equation 54 (CV) as a function of the number of standard deviations ($SD_{\Delta Hf}$) away from the mean heat of fusion for BA (—), DPA (—) and LOV (—). The graph on the left denotes the impact of the variation due to a positive change in the heat of fusion whereas the right presents the impact of a negative deviation. The markers denote the temperature where predictions have been made, with ■ and ● representing 25 °C (298.15 K) and (T_m - 10) K respectively.

For modelling capabilities, precise heats of fusion and melting temperatures for a compound are required in order to predict the solubility of a system in a given solvent, as well as those not measured. Therefore, having an accurate measurement for these physical properties of a target compound is key to an accurate solubility prediction that is built on scientific understanding of solubility thermodynamics. Figure *3-3* and accompanying Table 3-2 show the variation in the heat of fusion and melting temperature of the used model compounds.

In order to investigate the effect of the deviation in the heat of fusion on the accuracy of activity coefficients, Figure 3-8 presents the impact of the variation on the measured ideal solubility for each system, using the standard deviations in Table 3-2. From Figure 3-8, all systems show the variation of the true ideal solubility is impacted by the direction of the variation from the true value, with negative deviations (right) affecting the measured x^{id} greater than for positive deviations. For both positive and negative deviations, the temperature point at which solubility measurements are being made can influence how precise x^{id} will

be. Closer to the melting point of the solid, the deviation is markedly smaller. The order at which each compound is ranked on its variation does not change between $SD_{\Delta Hf}$ with it dependent on the magnitude of the variation from measurements, although going from 25 °C to (T_m-10°C) DPA and BA change order in both scenarios, with BA going from the 2nd highest to lowest in terms of CV.

According to equation 54, this variation would reduce the measured γ of systems, and so their predicted solubility independent of the model they are using. As well as the predicted solubility, information provided by the models on the molecular interactions within the system will be inaccurate leading to incorrect interpretations for solubility modelling. From equation 52, as the bracketed value is smaller the x^{id} will be smaller, so reducing the multiplier for whatever error is presented from the heat of fusion.

The analysis of the temperature dependence of the measured systems show that the compounds used are significantly more soluble in ketones, followed by the alcohols. For MFA, the esters used provided greater solubilities than that of the alcohols although still lesser than that of the ketones. From the applied models, the Wilson equation provides the best fitting according to the for all systems measured except for those close to an $\gamma \approx 1$ ($\ln \gamma \approx 0$) like for BA with this also being recognized in literature for non-ideal systems[16]. As these values are closer to 0, their absolute values are much smaller and so the errors associated with them are much larger. For systems where γ were further away from ideal, the σ improves.

As well as providing a better σ for the systems, the Wilson equation provides qualitative and quantitative data on the interactions between the molecules. From equation 66 and 67, -ve values of λ correspond to negative deviations from Raoult's Law whereas +ve λ values correspond to negative deviations[16]. These positive and negative deviations relate to the activity coefficient and so interaction between solute-solvent molecules within a given system. –ve deviations from non-ideal systems present with a $\gamma < 1$ according to equation 62, with these systems having a higher solubility than ideal and so the solute-solvent interactions are stronger than that of the solute-solute/solvent-solvent

interactions and vice-versa. Using the values obtained from Wilson analysis, interpretations of specific functional groups that exhibit beneficial interactions for solubility in a given system is possible.

For BA, both alcohols and ketone exhibit $\gamma \approx 1$. These systems are considered ideal in terms of their interactions and so there is no dominant interaction between the molecules highlighted by the small magnitude of the interaction parameters for these systems. Whereas 1,2-DMCH and DMF observe highly non-ideal interactions according to Figure 3-6. According to Raoult's law, solute-solvent interactions dominate with highly negative λ values, therefore detailing why BA observes a much higher solubility in this system compared to the others. Whereas for 1,2-DMCH the positive γ alongside the highly positive interaction coefficients reveal stronger like-like interactions between molecules and so reduced solubility in comparison to the other systems. So overall BA would observe a higher solubility in polar protic systems, whereas in more non-polar systems like 1,2-DMCH a lower solubility is observed and so could act as a suitable antisolvent due to its lower solubility.

Table 3-5: Ideal solvents to be used for each compound depending on the method to induce crystallization: cooling or antisolvent addition**.** For cooling, either a single or mixed solvent system could be used.

	Cooling		Antisolvent addition	
Compound	Solvent	Antisolvent	Solvent	Antisolvent
Benzoic Acid	Ethanol 2-Methyl-1-Propanol 3-Methyl-1-Butanol		DMF EtOH	Water
Diphenylamine	Ethanol 1,2-DMCH	1,2-DMCH Heptane	2-Butanone EtOH	Water
Mefenamic Acid	Iso-Propyl Acetate Butyl Acetate	Water	2-PeO IPA	Water
Lovastatin	IPA		AcO	Water

The other systems also can be defined this way, detailing suitable solvent classes on their interactions. For DPA and LOV, apolar protic solvents show greater

propensity of solute-solvent interactions than those of the polar protic solvents of BuOH and EtOH respectively. Non-polar solvents in the case of DPA shows no significant difference from the alcohols in terms of activity and so similar in solvation propensity. For LOV, although non-polar solvents were used it is observed that increasingly non-polar solvents will also observe higher like-like interactions with increasingly non-polar solvents showing reduction in solubility. The increasing solubility and increased –ve interaction parameters here follow the same trend shown in literature for alcohols, with it reaching a maximum solubility in BuOH, followed by a large reduction in solubility in more non-polar systems[85].

The molecular similarities of MFA to DPA help provide the same conclusions as observed for DPA. Increasingly non-polar and apolar protic solvents observe the most –ve Wilson interaction parameters, with these systems showing a highly non-ideal behavior. These systems like DPA show strong solute-solvent interactions and so ideal choices for crystallization solvents in terms of their increased solubility. Polar protic solvents show ideal behavior with their interaction parameters close to zero so a reduced solubility in comparison to the polar aprotic solvents.

Table 3-5 details the ideal specific solvent and antisolvent, which could be used to induce crystallization. For cooling crystallization, a large temperature dependence is preferred whereas for antisolvent a larger solubility is preferred. For BA, the best temperature dependence are observed for the methylated alcohols as well as alcohols such as EtOH. For mixed solvent cooling crystallizations, the purpose of the antisolvent is to reduce the solubility to a more acceptable value. For this non-polar systems like 1,2-DMCH will be ideal as they will not likely to produce synergistic relationships due to their lack of interaction with the solvent. For antisolvent crystallizations, larger solubilities are required so DMF and EtOH provide ideal options. For the antisolvent, the use of water is preferred due to its likely ability to interact the compound. DPA has extremely high solubility so all systems show good acceptability for cooling. In

terms of mixed solvent, water is the preferred option with it likely to interact with the compound to bring down to levels that are more acceptable. Like BA, water is a preferred antisolvent with the ketones being the preferred choice of solvent for antisolvent addition. For all systems the use of ketones and water are the preferred solvent and antisolvent for antisolvent addition.

The parameters identified by the Wilson model can be used to interpret suitable solvent types. By selecting a small amount of solvents each with different functional groups, the Wilson interaction parameters provide a quantitative basis to narrow down solvent screens to only favorable functional groups. By applying this type of analysis, the materials and time required can be reduced and so aiding the solvent selection procedure.

3.6 Conclusion

The solubility data and activity coefficient measurements for four different model compounds in a number of protic polar, aprotic polar and non-polar solvents over a large temperature range were determined from experimental clear point measurements and thermal analysis methods. The experimental data was described using regression to three semi-empirical models: van 't Hoff, Apelblat and Buchowski-Ksiazaczak (λh model), and three activity coefficient models: Margules, Van Laar and Wilson. The relative standard deviation for each system was used as a measurement for the appropriateness of the models to describe the solubility data. The Margules and Wilson model provided a low σ compared to the other models used. Unlike the Margules, the Wilson equation provides information on solute-solvent interactions which directly relate to the observed solubility. In a crystallization process design, suitable solubility behavior could be quantified in specific model parameter quantities which might aid in the solvent selection procedure.

3.7 Acknowledgements

The authors would like to acknowledge financial support from the Strathclyde Institute of Physical Biomedical and Sciences and the Doctoral Training Centre in Continuous Manufacturing and Crystallization (CMAC). I would also like to thank

Stephanie Urwin for her Mefenamic solubilities, Carlos Moreno for his helpful discussions.

3.8 References

1. Wouters OJ, McKee M, Luyten J. Estimated Research and Development Investment Needed to Bring a New Medicine to Market, 2009-2018. *JAMA - J Am Med Assoc*. 2020;323(9):844-853. doi:10.1001/jama.2020.1166
2. Savjani KT, Gajjar AK, Savjani JK. Drug Solubility: Importance and Enhancement Techniques. *ISRN Pharm*. 2012;2012(100 mL):1-10. doi:10.5402/2012/195727
3. Committee for Human Medicinal Products. ICH guideline Q3C (R5) on impurities: Guideline for Residual Solvents. *Int Conf Harmon Tech Requir Regist Pharm Hum Use*. 2015;44(October 2002):24.
4. Lewis A, Seckler M, Kramer H, Rosmalen G. Melt Crystallisation. In: *Industrial Crystallization: Fundamentals and Applications*. ; 2015:261-281.
5. Lewis A, Kramer H, Seckler M. Thermodynamics, Crystallzation Methods and Supersaturation. In: *Industrial Crystallization: Fundamentals and Applications*. ; 2015:1-25.
6. Spyriouni T, Krokidis X, Economou IG. Thermodynamics of pharmaceuticals: Prediction of solubility in pure and mixed solvents with PC-SAFT. *Fluid Phase Equilib*. 2011;302(1-2):331-337. doi:10.1016/j.fluid.2010.08.029
7. Loschen C, Klamt A. Solubility prediction, solvate and cocrystal screening as tools for rational crystal engineering. *J Pharm Pharmacol*. 2015;67(6):803-811. doi:10.1111/jphp.12376
8. Tung HH, Tabora J, Variankaval N, Bakken D, Chen CC. Prediction of pharmaceutical solubility via NRTL-SAC and COSMO-SAC. *J Pharm Sci*. 2008;97(5):1813-1820. doi:10.1002/jps.21032
9. Myerson AS, Erdemir D, Lee AY. Thermodynamic Concepts and Ideal Solubility. In: *Handbook of Industrial Crystallization*. ; 2019:1-31.
10. Zumdahl S. The Equilibrium Constant. In: *Chemistry*. 5th ed. Houghton

Mifflin; 1999:578-620.

11. Xu R, Huang C. Solubility Modeling and Solution Thermodynamics of 4-Amino-2,6-Dimethoxypyrimidine in Cosolvent Mixtures of Methanol, Ethanol, Isopropanol, and N, N-Dimethylformamide + Water. *J Chem Eng Data*. 2018;63(11):4234-4240. doi:10.1021/acs.jced.8b00719
12. Zhao H, Xu H, Yang Z, Li R. Solubility of 3,4-dichloronitrobenzene in methanol, ethanol, and liquid mixtures (methanol + water, ethanol + water): Experimental measurement and thermodynamic modeling. *J Chem Eng Data*. 2013;58(11):3061-3068. doi:10.1021/je400507u
13. Jia L, Yin Q. Insights into the mechanism of concomitant nucleation of form II and ethanol solvate of spironolactone in cooling crystallization †. 2018:9697-9706. doi:10.1039/c7ra13094e
14. Yang Y, Tang W, Li X, et al. Solubility of Benzoin in Six Monosolvents and in Some Binary Solvent Mixtures at Various Temperatures. *J Chem Eng Data*. 2017;62(10):3071-3083. doi:10.1021/acs.jced.7b00238
15. Gmehling J, Kleiber M. *Vapor-Liquid Equilibrium and Physical Properties for Distillation*.; 2014. doi:10.1016/B978-0-12-386547-2.00002-8
16. Seader JD, Henley E, Roper DK. *Seperation Process Principles-Chemical and Biochemical Operations*. 3rd ed. John Wiley & Sons, Inc.; 2011.
17. Smith JM, Ness HC Van, Abbot MM, Swihart MT. *Introduction to Chemical Engineering Thermodynamics Eight Edition*.; 2018.
18. Abbot M, Berthold J, de Loos T. *Models for Thermodynamic and Phase Equilibria Calculations*. 1st ed. (Sandler S, ed.).; 1994.
19. Vagenas GK, Marinos-Kouris D. Use of the Wilson equation for the prediction of the sorptional equilibrium of sugar-based foodstuffs. *Fluid Phase Equilib*. 1992;78(C):191-207. doi:10.1016/0378-3812(92)87034-K
20. Dojcanský J, Bafrncová S, Surový J. Application of the Wilson Equation with Binary Parameters to the Prediction of the Isothermal Vapour-Liquid Equilibrium Data of Ternary and Quaternary Systems in the Assessment of the Polar Solvent in Extractive Distillation. 2001;55(2):71-74.

21. Sadeghi R. Extension of the Wilson model to multicomponent polymer solutions: Applications to polymer-polymer aqueous two-phase systems. *J Chem Thermodyn*. 2005;37(1):55-60. doi:10.1016/j.jct.2004.08.007

22. von Raumer M, Hilfiker R. A Short Introduction to Polymorphism and Solid-State Development. In: *Polymorphism in the Pharmaceutuical Industr: Solid Form and Drug Development*. 1st ed. ; 2019:1-23.

23. Vrani E. Amorphous Pharmaeutical Solids. *Bosn J Basic Med Sci*. 2004;4(3):35-39.

24. Aitipamula S, Banerjee R, Bansal AK, et al. Polymorphs, salts, and cocrystals: What's in a name? *Cryst Growth Des*. 2012;12(5):2147-2152. doi:10.1021/cg3002948

25. Lewis A, Seckler M, Kramer H, Rosmalen G. Polymorphism. In: *Industrial Crystallization: Fundamentals and Applications*. ; 2015:303-319.

26. Cruz-Cabeza AJ, Reutzel-Edens SM, Bernstein J. Facts and fictions about polymorphism. *Chem Soc Rev*. 2015;44(23):8619-8635. doi:10.1039/c5cs00227c

27. Lee EH. A practical guide to pharmaceutical polymorph screening & selection. *Asian J Pharm Sci*. 2014;9(4):163-175. doi:10.1016/j.ajps.2014.05.002

28. Cesur S, Gokbel S. Crystallization of mefenamic acid and polymorphs. *Cryst Res Technol*. 2008;43(7):720-728. doi:10.1002/crat.200711119

29. Ferrari ES, Davey RJ, Cross WI, Gillon AL, Towler CS. Crystallization in polymorphic systems: The solution-mediated transformation of β to α glycine. *Cryst Growth Des*. 2003;3(1):53-60. doi:10.1021/cg025561b

30. Padrela L, Zeglinski J, Ryan KM. Insight into the Role of Additives in Controlling Polymorphic Outcome: A CO2-Antisolvent Crystallization Process of Carbamazepine. *Cryst Growth Des*. 2017;17(9):4544-4553. doi:10.1021/acs.cgd.7b00163

31. Kulkarni SA, McGarrity ES, Meekes H, Ter Horst JH. Isonicotinamide self-association: The link between solvent and polymorph nucleation. *Chem*

Commun. 2012;48(41):4983-4985. doi:10.1039/c2cc18025a

32. Joel Bernstein, Roger J. Davey, Jan-Olav Henck. Concomitant Polymorphs. *Angew Chemie Int Ed*. 1999;38(23):2440-3461. doi:10.1002/(SICI)1521-3773(19991203)38:23<3440::AID-ANIE3440>3.0.CO;2

33. Teychené S, Biscans B. Nucleation kinetics of polymorphs: Induction period and interfacial energy measurements. *Cryst Growth Des*. 2008;8(4):1133-1139. doi:10.1021/cg0609320

34. Jiang S, Horst JH, Jansens PJ. Concomitant Polymorphism of o-Aminobenzoic Acid in Antisolvent Crystallization. *Cryst Growth Des*. 2008;8(1):37-43.

35. ter Horst JH, Kramer HJM, Jansens PJ. A New Molecular Modeling Approach To Predict Concomitant Nucleation of Polymorphs. *Cryst Growth Des*. 2002;2(5):351-356.

36. Black S, Muller F, Fielding M. A Practical Approach for Using Solubility to Design Cooling Crystallisations. *Org Process Res Dev*. 2009;13:1315-1321.

37. Lewis A, Seckler M, Kramer H. Batch Crystallisation. In: *Industrial Crystallization*. ; 2015:178-191.

38. Zhang D, Liu L, Xu S, Du S, Dong W, Gong J. Optimization of cooling strategy and seeding by FBRM analysis of batch crystallization. *J Cryst Growth*. 2018;486:1-9. doi:10.1016/j.jcrysgro.2017.12.046

39. Zhang F, Liu T, Chen W, Ma CY, Wang XZ. Seed Recipe Design for Batch Cooling Crystallization with Application to l -Glutamic Acid. *Ind Eng Chem Res*. 2019;58(8):3175-3187. doi:10.1021/acs.iecr.8b06006

40. Pinho SP, Macedo EA. Solubility of NaCl, NaBr, and KCl in water, methanol, ethanol, and their mixed solvents. *J Chem Eng Data*. 2005;50(1):29-32. doi:10.1021/je049922y

41. Svärd M, Nordström FL, Jasnobulka T, Rasmuson ÅC. Thermodynamics and nucleation kinetics of m-aminobenzoic acid polymorphs. *Cryst Growth Des*. 2010;10(1):195-204. doi:10.1021/cg900850u

42. Mullin J. Ideal and Non-ideal Solutions. In: *Nucleation*. 4th ed. ; 2001:98-

100.

43. Bhamidi V, Kenis PJA, Zukoski CF. Probability of Nucleation in a Metastable Zone : Cooling Crystallization and Polythermal Method. doi:10.1021/acs.cgd.7b00875

44. Lenka M, Sarkar D. Determination of metastable zone width, induction period and primary nucleation kinetics for cooling crystallization of L-asparaginenohydrate. *J Cryst Growth*. 2014;408:85-90. doi:10.1016/j.jcrysgro.2014.09.027

45. Karpinski P, Baldyga J. Precipitation Processes. In: *Handbook of Industrial Crystallization*. 3rd ed. ; 2019:217-265.

46. Macedo EA. Solubility of amino acids, sugars, and proteins. *Pure Appl Chem*. 2005;77(3):559-568. doi:10.1351/pac200577030559

47. Giulietti M, Bernardo A. Crystallization by Antisolvent Addition and Cooling. *Cryst - Sci Technol*. 2012. doi:10.5772/50328

48. Chang J, Wang J, Diao Y, Wang W, Chen Q, Yu Z. Study on the solubility characteristic of the antisolvent crystallization of RDX. *J Phase Equilibria Diffus*. 2011;32(3):206-211. doi:10.1007/s11669-011-9872-3

49. Hansen TB, Qu H. Formation of Piroxicam Polymorphism in Solution Crystallization : E ff ect and Interplay of Operation Parameters. 2015. doi:10.1021/acs.cgd.5b01016

50. Hilfiker R, Blatter F, Szelagiewicz M. Screening for Polymorphs,Hydrates and Solvates. In: Hilfiker R, von Raumer M, eds. *Polymorphism in the Pharmaceutuical Industr: Solid Form and Drug Development*. 1st ed. ; 2019:241-256.

51. Lee S, Lee CH, Kim WS. Anti-solvent crystallization of L-threonine in Taylor crystallizers and MSMPR crystallizer: Effect of fluid dynamic motions on crystal size, shape, and recovery. *J Cryst Growth*. 2017;469:119-127. doi:10.1016/j.jcrysgro.2016.08.021

52. Ferguson S, Morris G, Hao H, Barrett M, Glennon B. Characterization of the anti-solvent batch, plug flow and MSMPR crystallization of benzoic acid.

Chem Eng Sci. 2013;104:44-54. doi:10.1016/j.ces.2013.09.006

53. Mostafa Nowee S, Abbas A, Romagnoli JA. Antisolvent crystallization: Model identification, experimental validation and dynamic simulation. *Chem Eng Sci*. 2008;63(22):5457-5467. doi:10.1016/j.ces.2008.08.003

54. Vellema J, Hunfeld NGM, Van Den Akker HEA, Ter Horst JH. Avoiding crystallization of lorazepam during infusion. *Eur J Pharm Sci*. 2011;44(5):621-626. doi:10.1016/j.ejps.2011.10.010

55. Nagy ZK, Fujiwara M, Braatz RD. Modelling and control of combined cooling and antisolvent crystallization processes. *J Process Control*. 2008;18(9):856-864. doi:10.1016/j.jprocont.2008.06.002

56. Braatz RD. Advanced control of crystallization processes. *Annu Rev Control*. 2002;26 I:87-99. doi:10.1016/S1367-5788(02)80016-5

57. Barik K, Prusti P, Mohapatra SS. Single- and multi-objective optimisation for a combined cooling and antisolvent semi-batch crystallisation process with an ACADO toolkit. *Indian Chem Eng*. 2020;62(3):287-300. doi:10.1080/00194506.2019.1677511

58. Lindenberg C, Krättli M, Cornel J, Mazzoti M, Brozio J. Design and optimization of a combined cooling/antisolvent crystallization process. *Cryst Growth Des*. 2009;9(2):1124-1136. doi:10.1021/cg800934h

59. Holaň J, Skořepová E, Heraud L, et al. Polymorphic Crystallization and Structural Aspects of Agomelatine Metastable Form X Prepared by Combined Antisolvent/Cooling Process. *Org Process Res Dev*. 2016;20(1):33-43. doi:10.1021/acs.oprd.5b00241

60. Zhang D, Xu S, Du S, Wang J, Gong J. Progress of Pharmaceutical Continuous Crystallization. *Engineering*. 2017;3(3):354-364. doi:10.1016/J.ENG.2017.03.023

61. Galan K, Eicke MJ, Elsner MP, Lorenz H, Seidel-Morgenstern A. Continuous preferential crystallization of chiral molecules in single and coupled mixed-suspension mixed-product-removal crystallizers. *Cryst Growth Des*. 2015;15(4):1808-1818. doi:10.1021/cg501854g

62. Pawar N, Agrawal S, Methekar R. Continuous Antisolvent Crystallization of α-Lactose Monohydrate: Impact of Process Parameters, Kinetic Estimation, and Dynamic Analysis. *Org Process Res Dev*. 2019;23(11):2394-2404. doi:10.1021/acs.oprd.9b00301

63. Sultana M, Jensen KF. Microfluidic continuous seeded crystallization: Extraction of growth kinetics and impact of impurity on morphology. *Cryst Growth Des*. 2012;12(12):6260-6266. doi:10.1021/cg301538y

64. Lawton S, Steele G, Shering P, Zhao L, Laird I, Ni XW. Continuous crystallization of pharmaceuticals using a continuous oscillatory baffled crystallizer. *Org Process Res Dev*. 2009;13(6):1357-1363. doi:10.1021/op900237x

65. Likozar B, Orehek J. Continuous Crystallization Processes in Pharmaceutical Manufacturing : A Review. 2021. doi:10.1021/acs.oprd.0c00398

66. Gong J, Tang W. Nucleation. *Pharm Cryst Sci Eng*. 2018:47-88. doi:10.1002/9781119046233.ch2

67. Sheikholeslamzadeh E, Rohani S. Solubility prediction of pharmaceutical and chemical compounds in pure and mixed solvents using predictive models. *Ind Eng Chem Res*. 2012;51(1):464-473. doi:10.1021/ie201344k

68. Lewis R, Evans W. Solutions and Solubility. *Chemistry (Easton)*. 2018:173-193. doi:10.1057/978-1-137-61037-9_11

69. Mane MB, Shinde SN. Vapor Liquid Equilibria: a Review. *Sci Revs Chem Commun*. 2012;2(2):158-171. www.sadgurupublications.com.

70. De Souza B, Keshavarz L, Steendam RRE, et al. Solubility Measurement and Thermodynamic Modeling of N-(4-Methylphenyl- Z-3-chloro-2-(phenylthio)propenamide in 12 Pure Solvents at Temperatures Ranging from 278.15 to 318.15 K. *J Chem Eng Data*. 2018;63(5):1419-1428. doi:10.1021/acs.jced.7b01011

71. Reus MA, Van Der Heijden AEDM, Ter Horst JH. Solubility Determination from Clear Points upon Solvent Addition. *Org Process Res Dev*.

2015;19(8):1004-1011. doi:10.1021/acs.oprd.5b00156

72. Brittain HG. Vibrational spectroscopic studies of cocrystals and salts. 2. The benzylamine-benzoic acid system. *Cryst Growth Des*. 2009;9(8):3497-3503. doi:10.1021/cg9001972

73. Surov AO, Terekhova I V., Bauer-Brandl A, Perlovich GL. Thermodynamic and structural aspects of some fenamate molecular crystals. *Cryst Growth Des*. 2009;9(7):3265-3272. doi:10.1021/cg900002q

74. Temperini MLA, Petrilli HM, Constantino VRL. Mefenamic Acid Anti-In fl ammatory Drug: Probing Its Polymorphs by Vibrational (IR and Raman) and Solid-State NMR Spectroscopies. 2014. doi:10.1021/jp500988k

75. Kato F, Otsuka M, Matsuda Y. Kinetic study of the transformation of mefenamic acid polymorphs in various solvents and under high humidity conditions. 2006;321:18-26. doi:10.1016/j.ijpharm.2006.04.020

76. Febra SA, Bernet T, Mack C, et al. Extending the SAFT-γ Mie approach to model benzoic acid, diphenylamine, and mefenamic acid: Solubility prediction and experimental measurement. *Fluid Phase Equilib*. 2021;540:113002. doi:10.1016/j.fluid.2021.113002

77. Granberg RA, Rasmuson ÅC. Solubility of paracetamol in pure solvents. *J Chem Eng Data*. 1999;44(6):1391-1395. doi:10.1021/je990124v

78. Sun H, Gong JB, Wang JK. Solubility of Lovastatin in acetone, methanol, ethanol, ethyl acetate, and butyl acetate between 283 K and 323 K. *J Chem Eng Data*. 2005;50(4):1389-1391. doi:10.1021/je0500781

79. Mudalip SKA, Bakar MRA, Jamal P, Adam F. Prediction of Mefenamic Acid Solubility and Molecular Interaction Energies in Di ff erent Classes of Organic Solvents and Water. *Ind Eng Chem Res*. 2018. doi:10.1021/acs.iecr.8b02722

80. Wan Y, He H, Zhang P, et al. Solid-liquid equilibrium solubility and thermodynamic properties of cis-5-norbornene-endo-2,3-dicarboxylic anhydride in fourteen pure solvents and three binary solvents at various temperatures. *J Mol Liq*. 2020;297:111396.

doi:10.1016/j.molliq.2019.111396

81. Shayanfar A, Velaga S, Jouyban A. Fluid Phase Equilibria Solubility of carbamazepine , nicotinamide and carbamazepine – nicotinamide cocrystal in ethanol – water mixtures. *Fluid Phase Equilib*. 2014;363:97-105. doi:10.1016/j.fluid.2013.11.024

82. Elliot JR, Lira CT. Introduction to Multicomponent Systems. In: *Introductory Chemical Engineering Thermodynamics*. ; 2012:369-411.

83. Gothard FA, Codrea Clobanu MF, Breban DG, Bucur CI, Sorescu G V. Predicting the Parameters in the Wilson Equations for Activity Coefficients in Binary Hydrocarbon Systems. *Ind Eng Chem Process Des Dev*. 1976;15(2):333-337. doi:10.1021/i260058a020

84. Hristova M, Donchev T, Kolev D, Baloch I, Georgiev H. Parameter'S Estimate in Wilson Equation. *Int Electron J Pure Appl Math*. 2015;7(3). doi:10.12732/iejpam.v9i1.4

85. Nti-Gyabaah J, Chmielowski R, Chan V, Chiew YC. Solubility of lovastatin in a family of six alcohols: Ethanol, 1-propanol, 1-butanol, 1-pentanol, 1-hexanol, and 1-octanol. *Int J Pharm*. 2008;359(1-2):111-117. doi:10.1016/j.ijpharm.2008.03.046

86. ter Horst JH, Schmidt C, Ulrich J. Fundamentals of Industrial Crystallization. In: *Handbook of Crystal Growth*. ; 2015:1317-1346.

87. Wichianphong N, Charoenchaitrakool M. Journal of Industrial and Engineering Chemistry Statistical optimization for production of mefenamic acid – nicotinamide cocrystals using gas anti-solvent (GAS) process. *J Ind Eng Chem*. 2018;62:375-382. doi:10.1016/j.jiec.2018.01.017

88. Sun H, Wang J. Solubility of lovastatin in acetone + water solvent mixtures. *J Chem Eng Data*. 2008;53(6):1335-1337. doi:10.1021/je800063d

89. Acree WE. Comments on "Solubility and Dissolution Thermodynamic Data of Cefpiramide in Pure Solvents and Binary Solvents." *J Solution Chem*. 2018;47(1):198-200. doi:10.1007/s10953-018-0714-3

90. Pramanik R, Bagchi S. Studies on solvation interaction: Solubility of a

betaine dye and a ketocyanine dye in homogeneous and heterogeneous media. *Indian J Chem - Sect A Inorganic, Phys Theor Anal Chem*. 2002;41(8):1580-1587.

91. Ruidiaz MA, Delgado DR, Martínez F, Marcus Y. Solubility and preferential solvation of sulfadiazine in 1,4-dioxane+water solvent mixtures. *Fluid Phase Equilib*. 2010;299(2):259-265. doi:10.1016/j.fluid.2010.09.027

92. Ter Horst JH, Deij MA, Cains PW. Discovering New Co-Crystals. *Cryst Growth Des*. 2009;9(3):1531-1537.

93. Yoshida MI, Oliveira MA, Gomes ECL, Mussel WN, Castro W V., Soares CD V. Thermal characterization of lovastatin in pharmaceutical formulations. *J Therm Anal Calorim*. 2011;106(3):657-664. doi:10.1007/s10973-011-1510-0

94. Sullivan RA, Davey RJ, Sadiq G, et al. Revealing the roles of desolvation and molecular self-assembly in crystal nucleation from solution: Benzoic and p -aminobenzoic acids. *Cryst Growth Des*. 2014;14(5):2689-2696. doi:10.1021/cg500441g

95. Shayanfar A, Fakhree MAA, Acree WE, Jouyban A. Solubility of lamotrigine, diazepam, and clonazepam in ethanol + water mixtures at 298.15 K. *J Chem Eng Data*. 2009;54(3):1107-1109. doi:10.1021/je8007827

96. Kongsamai P. Seperation of DL-Asparagine Enantiomers Using Crystallization Inhibitors. 2017.

97. Romero S, Escalera B, Bustamante P. Solubility behavior of polymorphs I and II of mefenamic acid in solvent mixtures. 1999;178:193-202.

98. Mack C, Hoffmann J, Sefcik J, ter Horst JH. Phase Diagram Determination and Process Development for Continuous Antisolvent Crystallizations. *Crystals*. 2022;12(8).

99. Black S, Dang L, Liu C, Wei H. On the measurement of solubility. *Org Process Res Dev*. 2013;17(3):486-492. doi:10.1021/op300336n

100. Zhang D, Xu S, Du S, Wang J, Gong J. Progress of Pharmaceutical Continuous Crystallization. *Engineering*. 2017;3(3):354-364.

doi:10.1016/J.ENG.2017.03.023

101. Bustamante P, Navarro J, Romero S, Escalera B. Thermodynamic origin of the solubility profile of drugs showing one or two maxima against the polarity of aqueous and nonaqueous mixtures: Niflumic acid and caffeine. *J Pharm Sci*. 2002;91(3):874-883. doi:10.1002/jps.10076

102. Granberg RA, Rasmuson AC. Solubility of paracetamol in binary and ternary mixtures of water plus acetone plus toluene. *J Chem Eng Data*. 2000;45(3):478-483. doi:10.1021/je990272l

103. Pacheco DP, Martínez F. Thermodynamic analysis of the solubility of naproxen in ethanol + water cosolvent mixtures. *Phys Chem Liq*. 2007;45(5):581-595. doi:10.1080/00319100701313862

104. Wang L, Yang W, Song Y, Gu Y. Solubility Measurement, Correlation, and Molecular Interactions of 3-Methyl-6-nitroindazole in Different Neat Solvents and Mixed Solvents from T = 278.15 to 328.15 K. *J Chem Eng Data*. 2019;64(8):3260-3269. doi:10.1021/acs.jced.8b01256

105. Li X, Chen J, Chen G, Zhao H. Solubility modelling, solution thermodynamics and preferential solvation of hymecromone in binary solvent mixtures of: N, N -dimethylformamide + methanol, ethanol or n -propanol. *RSC Adv*. 2017;7(73):46378-46387. doi:10.1039/c7ra07587a

106. Sato S, Hata T, Tsujita Y. The structure of monacolin K, C24H36O5. *Acta Cryst*. 1984;40(1):195-198.

107. Turner TD, Hatcher LE, Wilson CC, Roberts KJ. Habit Modification of the Active Pharmaceutical Ingredient Lovastatin Through a Predictive Solvent Selection Approach. *J Pharm Sci*. 2019;108(5):1779-1787. doi:10.1016/j.xphs.2018.12.012

108. Naik JB, Mokale V. Preparation of Freeze-dried Solid Dispersion Powder using Mannitol to Enhance Solubility of Lovastatin and Development of Sustained Release Tablet Dosage Form. *Columbia Int Publ Am J Pharm Sci Nanotechnol*. 2014;1(1):11-26. doi:10.13140/2.1.4312.5769

109. Mikhail SZ, Kimel WR. Densities and Viscosities of Methanol-Water

Mixtures. *J Chem Eng Data*. 1961;6(4):533-537. doi:10.1021/je60011a015

110. Perry RH, Green D. Densities of Aquous Organic Mixtures. In: *Perry's Chemical Engineers Handbook*. 7th ed. ; 1997:109-117. https://www.handymath.com/cgi-bin/isopropanolwghtvoltble5.cgi?submit=Entry.
111. Washburn EW. *International Critical Tables of Numerical Data of Physics, Chemistry, and Technology*. Vol 3. 1st ed. New York; 1930.
112. Thomas KT, McAllister RA. Densities of liquid-acetone-water solutions up to their normal boiling points. *AIChE J*. 1957;3(2):161-164. doi:10.1002/aic.690030206
113. Asghar SZ, Jouyban A, Martinez F, Rahimpour E. Solubility of naproxen in ternary mixtures of {ethanol + propylene glycol + water} at various temperatures: Data correlation and thermodynamic analysis. *J Mol Liq*. 2018;268:517-522. doi:10.1016/j.molliq.2018.07.082
114. Abbott M, Prausnitz J. Modelling the Excess Gibbs Energy. In: *Models for Thermodynamic and Phase Equilibria Calculations*. ; 1994:1-87.
115. Anslyn E, Dougherty D. Binding Forces. In: Murzdek J, ed. *Modern Physical Organic Chemistry*. 1st ed. ; 2006:168-177.
116. Editor G, Mccoustra M, Vendrell O, et al. Water–methanol mixtures: topology of hydrogen bonded network. *Phys Chem Chem Phys*. 2008;(10):5004-5011. doi:10.1039/b812223g
117. Yang B, Cao X, Lang H, Wang S, Sun C. Study on hydrogen bonding network in aqueous methanol solution by Raman spectroscopy. *Spectrochim Acta Part A Mol Biomol Spectrosc*. 2020;225:117488. doi:10.1016/j.saa.2019.117488
118. Valavi M, Svärd M, Rasmuson ÅC. Improving Estimates of the Crystallization Driving Force: Investigation into the Dependence on Temperature and Composition of Activity Coefficients in Solution. *Cryst Growth Des*. 2016;16(12):6951-6960. doi:10.1021/acs.cgd.6b01137

Chapter 4: Accurate Phase Diagrams for the Basic Design of Antisolvent Crystallization Processes

Corin Mack[1], Johannes Hoffmann[1], Jan Sefcik[2], Joop H. ter Horst[1,3]

1. University of Strathclyde, EPSRC Centre for Innovative Manufacturing in Continuous Manufacturing and Crystallization (CMAC), Strathclyde Institute of Pharmacy and Biomedical Sciences, Technology and Innovation Centre, 99 George Street, Glasgow G1 1RD, United Kingdom

2. Department of Chemical and Process Engineering, University of Strathclyde, Glasgow

3. Laboratoire Sciences et Méthodes Séparatives, Université de Rouen Normandie, Place Emile Blondel, 76821 Mont Saint Aignan Cedex, France

4.1 Abstract

Optimisation of antisolvent crystallization processes require accurate phase diagram construction. In this study, an approach to determine these antisolvent phase diagrams has been outlined, using four model compounds (Sodium bromate, DL-Asparagine Monohydrate, Mefenamic acid and Lovastatin) which are similar those observed in industry such as salts and hydrates, as well as highly water insoluble compounds. Using the temperature variation method, single solvent and solvent-antisolvent solubilities are obtained at varying temperatures, with the systems presenting with either a non-linear decrease from the onset of antisolvent addition or a synergistic increase towards a maximum. From these measurements, a semi-empirical model equation encompassing both temperature and antisolvent fraction was designed to describe the entire antisolvent phase diagram. These were compared to the model systems finding good agreement with the measured system. Utilising this equation, basic antisolvent crystallization design for each system identified optimized regions for each system based on productivity, slurry density and yield. A workflow was developed for the methodology followed here for future applications.

4.2 Introduction

The access to accurate solubilities of pharmaceutical compounds sets the foundations towards the design and optimization of crystallization processes[86,87]. Although there are methods developed to determine the solubility from computational methods, the need for experimentally determined values is still required in order to account for accuracy as well as regulatory approval[67,85,79]. Solubility data in single solvent mixtures is widely accessible for a large variety of compounds whereas solubilities in binary solvent mixtures are much less common[46,78].

It is common in antisolvent crystallization that upon increasing the antisolvent fraction the solubility decreases substantially more than the concentration decreases due to dilution. It is only until the solubility drops below that of the dilution line at higher antisolvent fractions that recrystallization is thermodynamically possible. In order to establish the phase diagram in anti-solvent crystallization process development, the most common method used is the gravimetric method, in which a suspension is equilibrated and the solution concentration is determined at a specific temperature[88,89,41]. Work by Reus et al.[71] displayed a variation of this equilibrium method, utilizing solvent addition to a suspension in order to dissolve the measured solute and obtain its saturation concentration. Alongside these, spectrographic methods[90] are used to determine the concentration of solutes in mixed solvent systems after the equilibrium method has been applied as is shown in the case of sulfadiazine[91]. Although effective, the constant temperature method commonly used takes substantial laboratory effort and time.

Temperature variation methods, in which temperature of a suspension is slowly increased until the temperature dependent solubility matches the overall sample composition[92], have become more important. In this method, the saturation temperature is approximated by the clear point temperature, the temperature at which, upon increasing the temperature of a suspension, the suspension turns into a clear solution. This method has been utilized in many single solvent systems in order to establish single solvent data, but its applicability has not yet

been widely used for the process of establishing mixed solvent solubility data, as the variable temperature is introduced, next to compound concentration and antisolvent fraction, increasing complexity of the analysis. One previous example of the use of the temperature variation method for such a system is shown by Vellema et al.[54] describing the solubility of Lorazepam at varying levels of glucose solution, in order to determine the correct operating window to prevent recrystallization of Lorazepam solution during infusion.

Therefore, the objective of this work is to outline an approach to accurately obtain phase diagrams for anti-solvent crystallization process design using the temperature variation method. For four model systems, the phase diagram for antisolvent crystallization is determined as a function of temperature and antisolvent fraction. From the observed saturation data, a solubility model is established. The model is then used for a basic process design identifying the most optimal region in terms of antisolvent fraction and temperature to achieve a productivity, yield and suspension density within specifications.

4.3 Materials and Methods

4.3.1 Materials

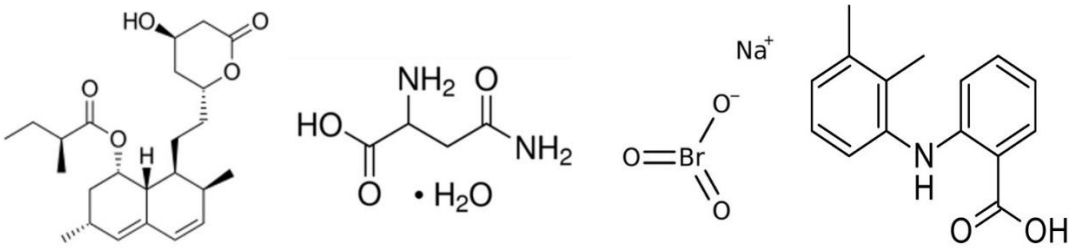

Figure 4-1: Molecular structure of the four model compounds. From left to right: Lovastatin (LOV), DL-Asparagine Monohydrate (DL-Asn.H_2O), Sodium Bromate ($NaBrO_3$) and Mefenamic Acid (MFA).

The molecular structures of the model compounds are shown in Figure 4-1. Lovastatin (LOV) was supplied from Molekula (>98%, Darlington), DL-Asparagine Monohydrate (DL-Asn.H_2O), Sodium Bromate ($NaBrO_3$) and Mefenamic Acid (MFA) were obtained from Sigma Aldrich (>99%). All compounds were used as received. For solution preparation, acetone (99%) and

ethanol (99%) were obtained from VWR International. The water used was distilled and filtered using the in-house Millipore Systems setup.

Sodium bromate ($NaBrO_3$) is a water-soluble salt used as one the compounds of interest in this piece of work. In solution, it is achiral but crystallizes as a single chiral enantiomer in the space group $P2_13$. As $NaBrO_3$ is a salt with a high water solubility, it is a good model compound for this study, allowing non-toxic solvents and antisolvent to be used.

Asparagine monohydrate is a non-essential amino acid, and is known to crystallize as a conglomerate forming system in either the L- or D- configuration. For the purpose of this work, the racemic form of the system is used and so has the configuration DL-Asn.H_2O. This compound has been frequently used throughout literature as a model compound for crystallization systems, with its solubility in water and other systems previously investigated. This makes it a good choice for a model compound in this work.

Mefenamic acid is a member of the anthranilic acid derivatives of non-steroidal anti-inflammatory drugs (NSAIDs), used for the treatment of mild and moderate pains. It is not widely used compared to other NSAID due to its higher costs. MFA is known to have two polymorphic forms Form 1 and Form 2, although the later it has only been isolated in DMF and through high-pressured systems and has not been identified in systems similar to the one here from the literature. MFA is a non-polar compound and so presents a very low solubility in water similar to other NSAID on the market. Therefore, MFA is a good model compound as it mimics similar instances to that found in industry.

Lovastatin (LOV) is a widely statin family molecule used in the treatment of high cholesterol and cardiovascular disease. It does not have any known polymorphs and is not chiral although presenting a number of chiral centres. Similar to MFA it is highly non-polar and so its very low solubility in water in comparison to other solvents has been noted in literature. Like MFA, LOV presents itself as a similar molecule to that found in industry and so is a good model compound for this study.

4.3.2 Clear point temperature Measurements

A known amount of the crystalline compound was added to a standard HPLC vial. Then, 1 ml of a solvent/antisolvent mixture with known antisolvent mass fraction x_{AS} was pipetted into the HPLC vial from a larger volume of prepared solvent/antisolvent mixture stock solution. These vials were weighed before and after addition of solvent mixture to exactly determine the mass of solvent mixture added. Composition of the sample is denoted by the (solute-free) antisolvent mass fraction x_{AS} and solute concentration C, respectively. The antisolvent mass fraction in the vials equals that in the stock solution, determined from the mass of solvent and antisolvent used to make the stock solution:

$$x_{AS} = \frac{m_{AS}}{m_S + m_{AS}} \qquad 68$$

Where m_{AS} (g) and m_S (g) represent the mass of antisolvent and solvent respectively in the mixture.

The Crystal16 Multiple Reactor Setup (Technobis Crystallization Systems) was used to determine the saturation temperature of the prepared samples. The saturation temperature of the samples was determined in triplicate, with the average between these measurements assumed to be equal to the saturation temperature of the overall sample composition in the vial. Due to known issues of Lovastatin degrading over time in solutions[93] the total experimental time experienced by each sample containing lovastatin was kept smaller than 24hrs. In the case of LOV experiments, there were no observations of large variances between subsequent clear point temperatures of the same sample, indicating degradation of lovastatin is negligible. Also, the measurements with the model compounds $NaBrO_3$ and DL-ASN did not show large variances. Occasionally, samples displayed larger than 1 °C difference between clear point temperatures measured in subsequent cycles and these measurements were then discarded and fresh samples were used in a re-run. This deviation in clear point was usually coinciding with crowning of crystals just above the liquid level in the sample vials. This often could be mitigated by increasing the solvent mixture volume within the vial and decreasing the stirring rate.

The procedure was slightly adapted for MFA measurements due to the polymorphic nature of MFA to remove the impact of polymorphic nucleation of the undesired form from cycling. Instead of 3 measurements, only a single measurement was obtained for a single sample using the initial suspension in the vial without the initial dissolution step. The other polymorph has only been observed from DMF[28]. Therefore, it is unlikely that the other polymorph will be observed with the solvents used. Although due to the lack of certainty this method was deemed acceptable for the scope of the chapter. Vials filled with pure ethanol were added to the Crystal16 setup and held at 20 °C for a short time period. Then, a tune step was performed, registering this clear solution as a reference for complete dissolution of the suspension. Subsequently, the prepared vials containing MFA slurries with the original raw material (Form 1) in ethanol-water mixtures were added to the machine and the temperature was slowly ramped up to a set point temperature of 60 °C. The clear point temperature at which 100% light transmission was reached was taken as the saturation temperature of the sample. Subsequent measurements with the same sample were not done. For this reason a large number of measurements were performed for this model compound.

Fitting of experimental data was done using the MatLab Curve Fitting tool.

4.4 Results

4.4.1 Single Solvent Solubility

Figure 4-2(left) displays the measured temperature dependent solubilities of LOV in acetone, DL-Asn.H_2O in water, MFA in ethanol and $NaBrO_3$ in water. Similar to other sodium salts with affinity to dissociate themselves in water[40,94] the solubility of $NaBrO_3$ in water is large, for instance 367 mg/g at 25°C, and it increases with temperature to 505 mg/g at 40 °C. The solubility of LOV in acetone and DL-Asn.H_2O in water are similar with solubilities ranging from 80 mg/g to 180 mg/g between 20 °C and 40 °C. The solubility of MFA in ethanol is the lowest of the measured systems, with solubilities between 10 mg/g and 42 mg/g at temperatures ranging from 25 °C to 60 °C. Each system shows a strong temperature dependence in their single solvents.

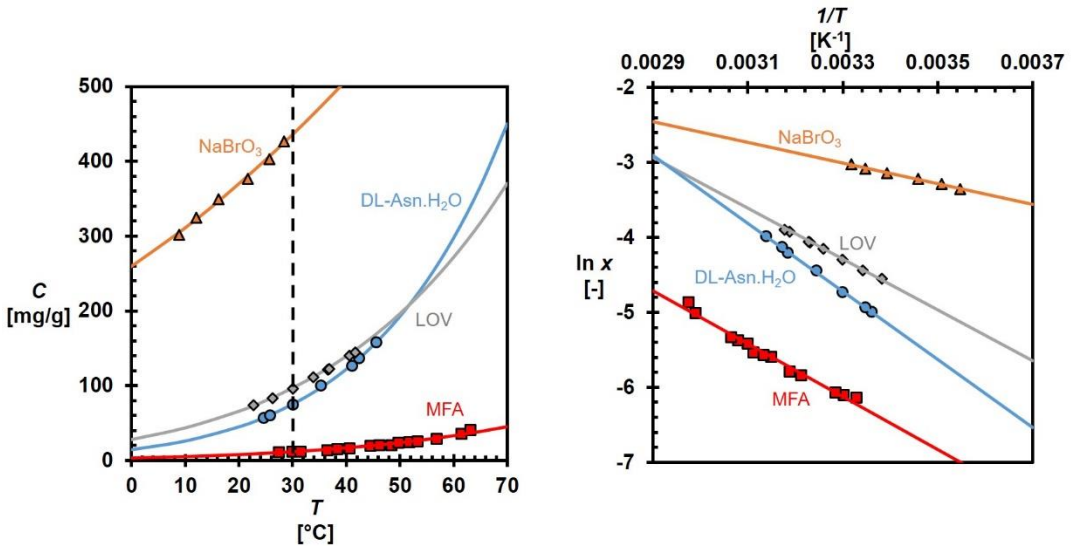

Figure 4-2: Left: Single solvent solubilities of LOV in acetone (♦), DL-Asn.H_2O in H_2O (●), $NaBrO_3$ in water (▲) and MFA in ethanol (■) showing the measured saturation temperature T at concentrations C. Right: The van 't Hoff plot of the same data. The lines through the points are best fits of the Van 't Hoff equation. The error bars for each concentration is marked by a red cap. For some systems the error bars are below the marker. MFA does not have error bars due to the method used to obtain the saturation temperatures, with no repeating cycles carried out.

The van 't Hoff equation (equation 69) describes the ideal solubility x_{id} as a function of temperature T using only two solid state properties: melting temperature T_m and heat of fusion ΔH (kJ mol^{-1}).

$$\ln x_{id} = -\frac{\Delta H}{R}\left(\frac{1}{T} - \frac{1}{T_m}\right) \qquad 69$$

with the molar gas constant R. Due to non-ideality in the solution the ideal solubility can substantially deviate from the measured solubilities. However, often, equation 3, the linearized form of equation 69, gives a good fit to experimental data within a sufficiently narrow temperature region.:

$$\ln x = \frac{a}{T} + b \qquad 70$$

The parameters a and b can be determined from a linear fit in the plot of ln$x$ versus 1/T.

The Van't Hoff relationship describes well the measured solubilities in Figure 4-2(Right) within the measured temperature region using equation 70.

4.4.2 Solubility in Solvent/Antisolvent Mixtures

In ethanol, $NaBrO_3$ and DL-Asn.H_2O are both known to be insoluble due to the anionic and polar nature of respectively $NaBrO_3$ and DL-Asn.H_2O. Therefore, ethanol is chosen as antisolvent in these systems. Both LOV and MFA are insoluble in water with no measured values available in literature. Therefore, water is chosen as antisolvent for both LOV and MFA. Figure 4-3 (left) displays the temperature dependent solubility for all model compounds obtained at specific anti-solvent fractions. In all instances, the solubility increases with temperature at a constant antisolvent fraction.

For $NaBrO_3$, the solubility reduces non-linearly as a function of antisolvent fraction as observed from its corresponding mol fraction reduction at 30 °C. When going from x_{AS} = 0 to x_{AS} = 0.1 at 30°C the solubility drops 43% from 433 mg/g to 247 mg/g. The solubility drops further 20% going to x_{AS} = 0.2, with having decreased by 97% from its original solubility at x_{AS} = 0.5. This trend of a non-linear solubility decrease as a function of antisolvent is consistent with the preferred antisolvent behavior for systems[14,95].

A similar behavior is observed for DL-Asn.H_2O and MFA with the solubilities decreasing as a function of antisolvent fraction. The non-linear decrease in the solubility with increasing antisolvent fraction for both DL-Asn.H_2O and MFA is similar to that observed for $NaBrO_3$, with a 40% drop in the saturation concentration going from 75 mg/g (x_{AS} = 0) to 45 mg/g (x_{AS} = 0.1) at 30°C (0.0033K^{-1}) observed for DL-Asn.H_2O, alongside a 37% drop for MFA. Although DL-Asn.H_2O is known to recrystallize as the anhydrous form at higher antisolvent fractions[71], the difference between them in terms of solubility can be seen as negligible due to how similar they are when correlated for[96]. As well as this, the amount of solvent added from dissolution into the system is negligible compared to water already present to influence solubility significantly.

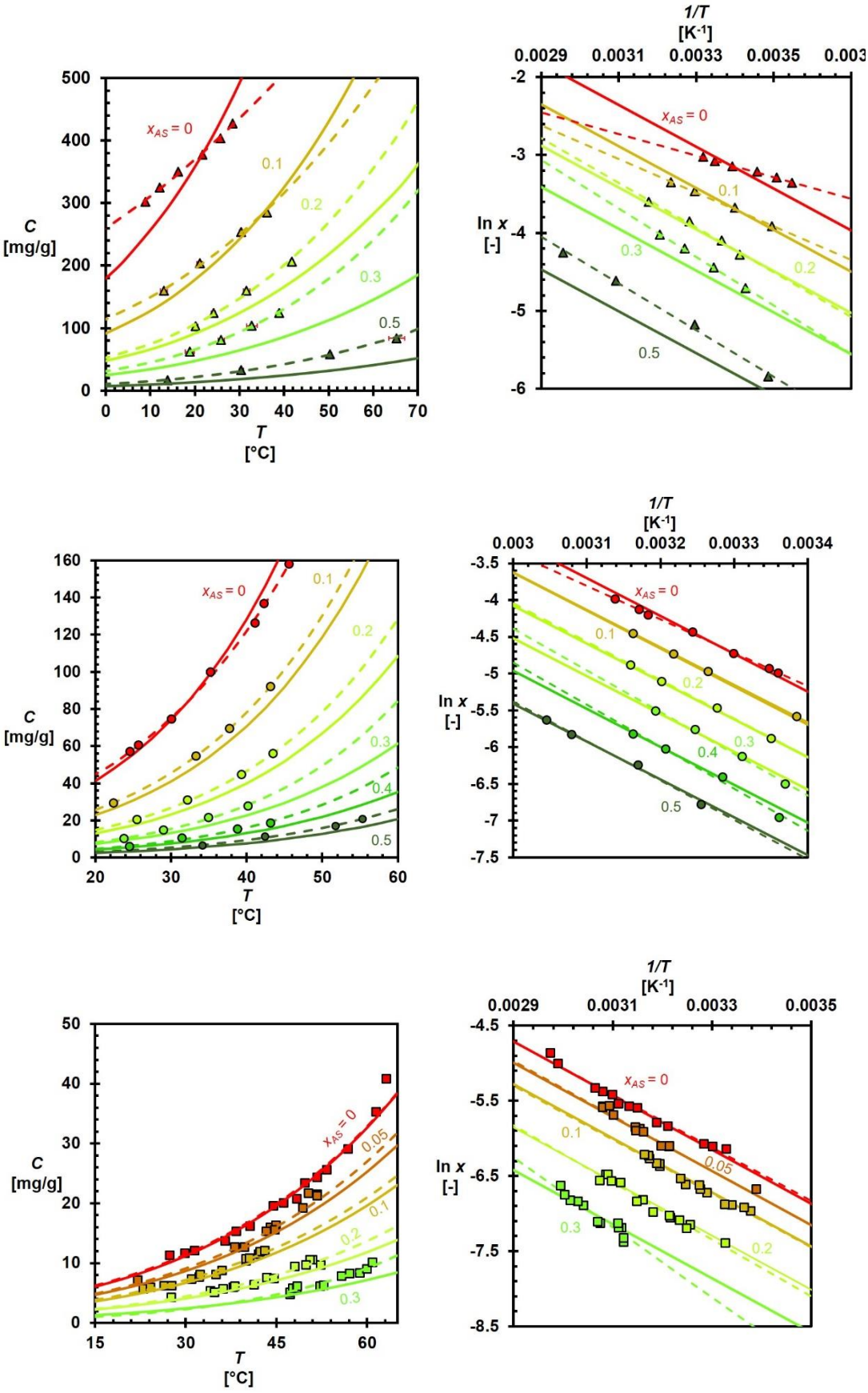
C
[mg/g]
T
[°C]
x_{AS} = 0
0.1
0.2
0.3
0.4
0.5
1/T
[K-1]
ln x
[-]
0.05

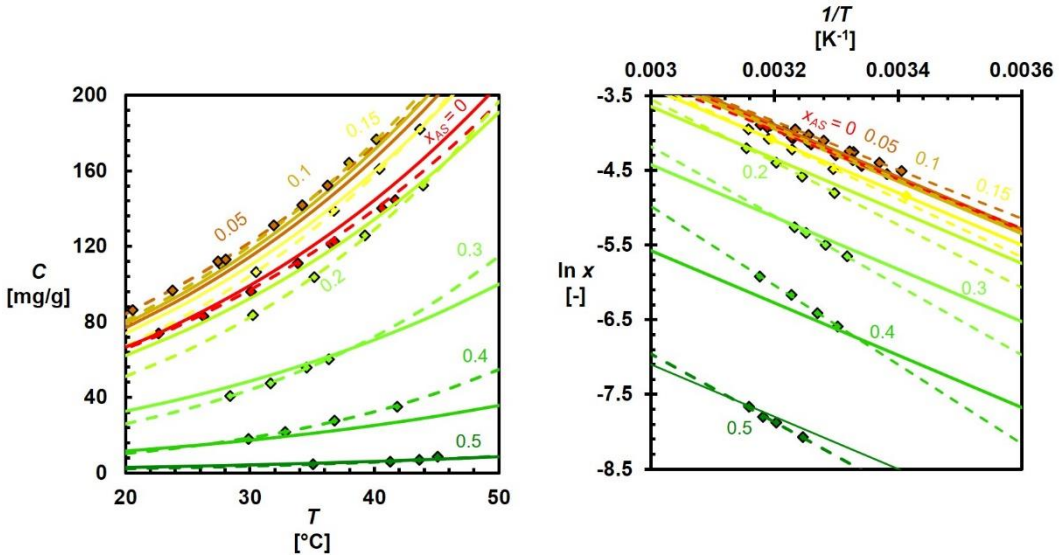

Figure 4-3: Concentration-Temperature diagrams (left) and the Van 't Hoff diagrams (right) of $NaBrO_3$ (▲) and DL-Asn.H_2O (●) in water-ethanol, LOV (♦) in acetone/water and MFA (■) in ethanol/water at various antisolvent fractions. The experimental data for each system is represented by the markers on each plot, with the colours and respective label representing the change in antisolvent fraction within each system. The dashed lines passing through each set of experimental data is derived from their respective Van't Hoff plot. The solid lines represent the predicted solubility at each antisolvent using Equation 71. Red caps mark the error bars for each concentration. For some concentrations, the error bar is below the marker. MFA does not have error bars due to the method used to obtain the saturation temperatures, with no repeating cycles carried out.

However, LOV in acetone-water at small antisolvent fractions, the opposite behavior is observed. Going from x_{AS} = 0 to x_{AS} = 0.05 at 30°C, the solubility increases from 98 mg/g to 122 mg/g representing a 26% increase. As the antisolvent fraction increases further, the solubility decreases. At x_{AS} = 0.1 the solubility reduces to 98 mg/g and it reduces to below its pure system concentration at x_{AS} = 0.2. At x_{AS} = 0.5 the solubility has further non-linearly decreased to 4.6 mg/g, beyond which no accurate data could be obtained. Several systems exhibit similar solubility behavior, especially in systems where water is

used as the antisolvent[90,91] although it has also been found in systems where water is not used[97]. The raw data for each system can be found in the supplementary information for the following paper[98].

4.4.3 Antisolvent Crystallization Phase Diagrams

Utilizing the observed behavior of the solubility as a function of temperature and antisolvent fraction a single empirical equation is proposed based on the van't Hoff equation (equation 70) with antisolvent fraction dependent van 't Hoff parameters in order to provide an equation to predict solubility as a function of temperature and antisolvent concurrently:

$$\ln x = \left((a x_{AS} + a')\frac{1}{T}\right) + b x_{AS}^2 + b' x_{AS} + b'' \qquad 71$$

Table 4-1: Fitting parameters obtained from the model equation 71 using the entire dataset for a combination of compound, solvent and antisolvent. The 95% confidence interval detailing the goodness for these fits to the experimental data are given as error intervals. The σ for each system for all data point used is provided.

		Fitting Parameters						
Compound	**Solvent/Anti-solvent**	***N*** **[-]**	***a*** **[-]**	***a'*** **[-]**	***b*** **[-]**	***b'*** **[-]**	***b''*** **[-]**	***σ*** **[%]**
$NaBrO_3$	Water/ EtOH	22	0	-2580 ± 351	0	5.2 ± 0.3	5.6 ± 1.0	15
DL-Asn.H_2O	Water/ EtOH	27	0	-5149 ± 234	0	-4.4 ±0.1	12.3 ± 0.8	4.8
MFA	EtOH/Water	65	0	-3592 ± 276	0	-5.7 ±0.4	5.7 ± 0.9	5.9
LOV	AcO/Water	39	0	-3498 ± 506	-18.7 ± 1.4	1.6 ± 0.7	7.2 ± 1.6	7.7

The fitted parameters of equation 71 are shown in Table 4-1. The goodness of the fit for the model was determined between the predicted mol fraction x_{pred} and the actual mol fraction x_i for each system at a given temperature using the following equation for the relative standard deviation (σ):

$$\sigma = 100 * \sqrt{\frac{\sum_{i=1}^{N}\left(\frac{x_i - x_{pred}}{x_i}\right)^2}{N-1}} \qquad 72$$

With the σ measured in % and *N* being the total number of experimental data points used.

The model describes the systems with MFA and DL-Asn.H_2O reasonably well with σ of respectively 5.9 and 4.8%. For the LOV system, with the more complex antisolvent fraction dependent solubility behavior, the model performs reasonably well with a σ of 7.7%. The ability of the model to capture the change in antisolvent and temperature is shown through the respective Van't Hoff plots for each model compound as presented in Figure 4-3.

The resulting fitting of the $NaBrO_3$ system shows a rather large σ of 15%. This is because the system shows a strong effect of the antisolvent fraction on the temperature dependence of the solubility. The addition of the parameter *a* does not improve the fitting, which shows that different fitting equations should be used if a more accurate description is needed.

Figure 4-4 shows the antisolvent crystallization phase diagrams for all the systems constructed using the model at a temperature of 20 and 40°C. For $NaBrO_3$, the solubility at x_{AS} = 0 nearly doubles when doubling the temperature, going from c* = 357 mg/g to 665 mg/g. This follows Black's rule closely[99]. As the antisolvent fraction increases, the solubility at x_{AS} = 0.1 decreases by half for both temperature fractions. At other fractions when comparing between both temperatures, this observation is conserved. Unlike $NaBrO_3$, DL-Asn.H_2O observes a 309% increase when doubling the temperature. This difference between the systems is conserved at each antisolvent fraction similar to $NaBrO_3$. MFA observes the same observations as $NaBrO_3$. For LOV at 40 °C, the synergistic effect observed is more defined than at 20 °C, with its solubility differences at increasing antisolvent fractions similar to $NaBrO_3$ and MFA. From equation 69, this observation is to be expected as it predicts there to be no change in temperature dependence at increasing antisolvent fractions.

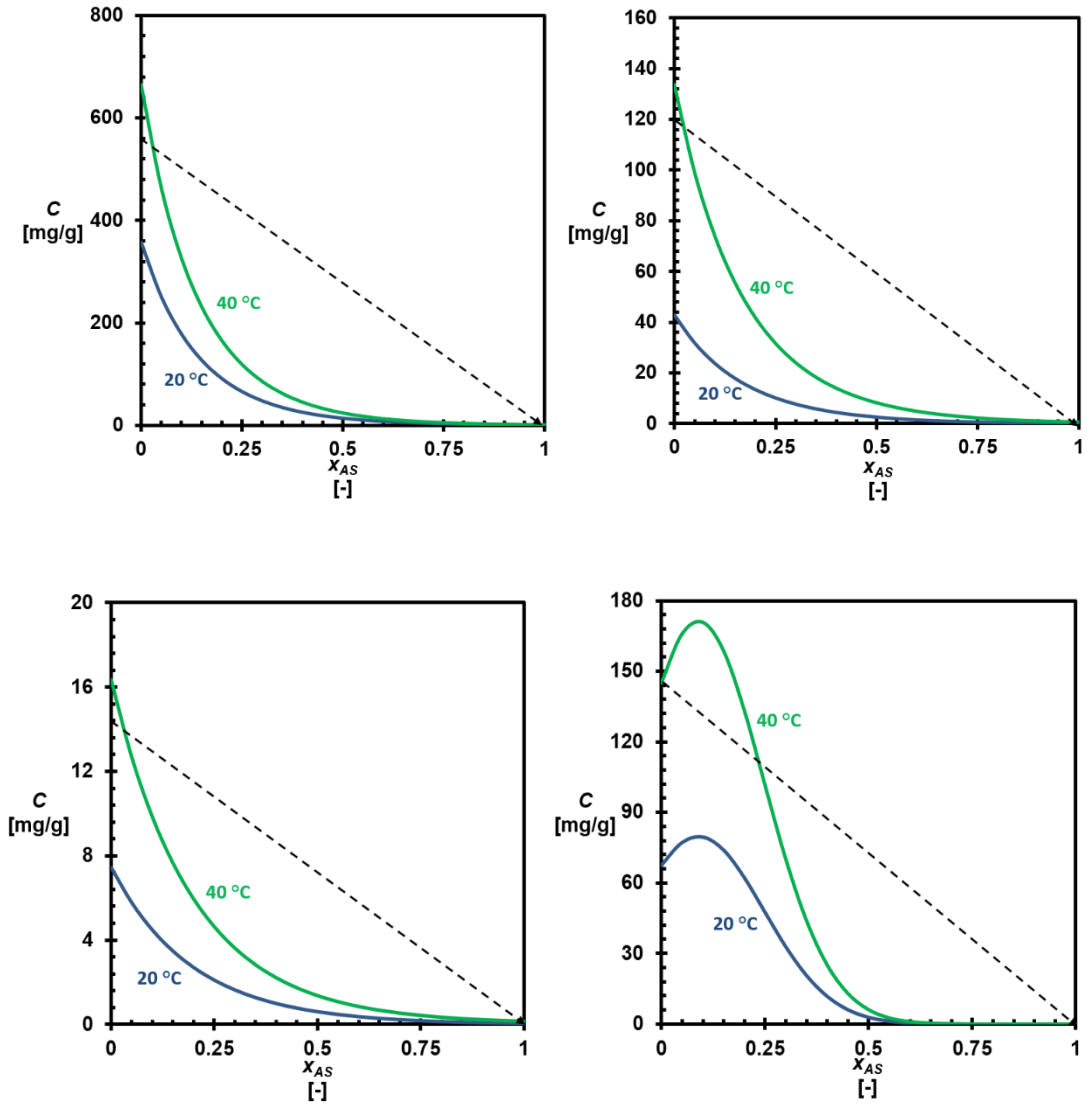

Figure 4-4: The predicted antisolvent crystallization phase diagram of $NaBrO_3$ (top left) and DL-Asn.H_2O (top right) in water-EtOH , MFA in EtOH-water (bottom left) and LOV in AcO-water (bottom right) at 20 °C and 40 °C from the fit to equation 71 using the values in Table 4-1. The dashed line cutting through each antisolvent phase diagram represents the dilution line caused by the addition of antisolvent to a saturated solvent.

Generally for anti-solvent crystallization, by adding an antisolvent the solubility of the solute decreases, inducing a thermodynamic driving force from which crystallization of an API is possible[47]. In doing this, dilution of the overall concentration of the system also occurs due to the addition of another solvent.

This dilution effect is visualized in Figure 4-4. The dilution effect on a system follows a linear path, dictating several key process parameters from the visualization of the dilution of the system due to increased total solvent amount. For each system, as the antisolvent is added the amount of product that can be obtained reduces, so the maximum amount to be obtained from crystallization reduces. It also dictates the supersaturation S being experienced by the system with the equation:

$$S = \frac{c_{x_{AS}}}{c^*_{x_{AS}}} \qquad 73$$

Where $c_{x_{AS}}$ and $c^*_{x_{AS}}$ corresponds to the concentration of the system according to the dilution line and the solubility respectively at a specific antisolvent fraction. For $NaBrO_3$, DL-Asn.H_2O and MFA, the addition of the antisolvent causes the systems to supersaturate according to equation 73. As more antisolvent is added the system becomes more supersaturated as the difference between the dilution and solubility line increases. At a certain supersaturation, the solute will crystallize. For LOV, the initial maxima causes the dilution line to fall below the solubility line and so crystallization is not thermodynamically feasible. It is not until a higher antisolvent fraction of x_{AS} = 0.25 that the system becomes supersaturated and so crystallization is feasible. Although due to the dilution of the system, the maximum yield is reduced.

4.4.4 Continuous Antisolvent Crystallization Productivity and Yield

The use of continuous antisolvent crystallization allows better yields to be obtained for a crystallizing system, while also reducing the variation observed by batch-to-batch crystallizations[62]. Instead of a sealed vessel for batch crystallization, a continuous process has both an inlet and outlet stream, adding in both the crystallizing solution and the antisolvent while simultaneously removing the crystallized product as shown in Figure 4-5. In a continuous antisolvent crystallization, the general operating variables are temperature, residence time and antisolvent addition rate[100]. We can define three boundary conditions for the continuous antisolvent crystallization in Figure 4-5, such as productivity is ≥ 0.012 g/ghr^{-1}, loss is ≤ 10% and slurry density ≤ 20%

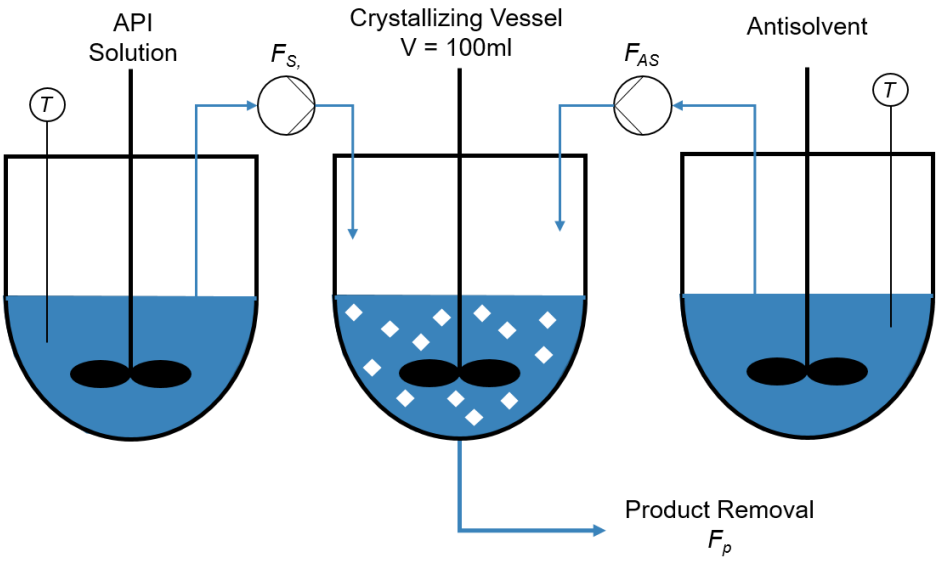

Figure 4-5: Schematic of a continuous antisolvent crystallization process consisting of a feed vessel with the concentrated solution (left), a crystallization vessel (middle) and an antisolvent feed vessel (right). The solution and antisolvent are continuously fed into the crystallization vessel V (blue lines) at specific feed rates for the saturated solution F_s and antisolvent F_{AS} with continuous product removal stream F_p to provide a specific residence time τ to allow the consumption of supersaturation by the crystals in the suspension.

First, we can define a productivity, which is a measure of how effective the system is for obtaining solid product. The productivity P for each system at a specific antisolvent fraction is determined by:

$$P_{x_{AS}} = \frac{c_{x_{AS}} - c^*_{x_{AS}}}{\tau} \qquad 74$$

With it being the difference in overall concentration at a specific antisolvent fraction $C_{x_{AS}}$ with unit g/g, and the solubility of the solute at that same fraction $c^*_{x_{AS}}$ in g/g at a residence time τ in hours, assuming that the crystallization kinetics are sufficiently fast so that all supersaturation is consumed by the forming and growing crystals. This means that the residence time is sufficiently long. The residence time is defined as the average time molecules spend in the

crystallizer and is determined by the crystallizer volume V and the flow rate F_p of the outlet feed.

$$\tau = \frac{V}{F_p} \qquad 75$$

Long residence times allow the maximum amount of product to be obtained. If the residence time becomes too short, the concentration in the crystallizer will deviate from the saturation concentration as the crystallization kinetics are not fast enough to consume all supersaturation. A target productivity of an economically viable chemical process leading is regarded to be $P \geq 0.012$ g/ghr.

Alongside the productivity, the loss L, having the same units as the productivity, can be defined as one of the boundary conditions of the process. The loss in a continuous antisolvent crystallization process is related to the amount of product remaining in solution, which is determined by the solubility of the product in the crystallizing solvent mixture, if the crystallization kinetics are sufficiently fast. Here we define the Loss L in relation to the productivity P and residence time of the system τ:

$$L_{x_{AS}} = \frac{c_{x_{AS}}}{\tau} - P_{x_{AS}} = \frac{c^*_{x_{AS}}}{\tau} \qquad 76$$

The yield Y is the amount of product crystallized and removed from the crystallization vessel. So by assuming a minimum yield of Y_{min} = 90%, the maximum loss L_{max} should be lower than 10% remaining in solution.

The third boundary condition is the suspension density, which is defined as a weight fraction of the crystallizer occupied by the solid phase. This is calculated from the following equation:

$$\rho_{Slurry} = \left(\frac{x_{AS} - x_{AS,f}}{1 - x_{AS}}\right)\left(\frac{P_{x_{AS}}}{1 + P_{x_{AS}}}\right) \qquad 77$$

With x_{AS} and $x_{AS,f}$ representing the antisolvent content present in the solution and the antisolvent present in the feed solution, alongside the solids present through the calculated productivity. Here we assume that the antisolvent does not contain any solute. The more product crystallizes from the solution, the larger

the suspension density. If the suspension density becomes too high the suspension of crystals is hampered which would decrease the product quality from the process. We assume that a suspension density of $\rho_{Max} = 20\%$ is the upper boundary limit of a continuous antisolvent crystallization to maintain proper mixing.

The predicted productivity P, loss L and slurry density ρ_{slurry} for each system is presented in Figure 4-6 with a residence time τ of 0.42 hours and a saturated feed. From Figure 4-6, the productivity of $NaBrO_3$ increases significantly from x_{AS} = 0 up to x_{AS} = 0.3 while simultaneously the loss decreases. As the productivity is related to the difference between the dilution line and solubility of the API from equation 72, the maximum observed is expected with the solubility reducing to a smaller degree at higher antisolvent fractions than at the lower amounts. Therefore, this analysis shows that systems can be optimized up to specific antisolvent fractions to obtain the highest possible productivity, beyond which influences both the productivity and so inherently the effectiveness of the process. The loss decreases similarly to the solubility curve, as the solute left in solution is not able to recrystallize. Due to the high absolute concentration, the slurry density increases significantly at increasing antisolvent fractions due to the presence of recrystallized $NaBrO_3$. At a higher antisolvent fraction, the slurry density presents a maximum with the productivity also decreasing and antisolvent presence factor reducing similarly. Due to infinite dilution, the slurry density would be expected to reach a maximum as shown with it going to zero at x_{AS} = 1.

Like for $NaBrO_3$, DL-Asn.H_2O and MFA, the productivity increases non-linearly at increasing antisolvent fractions with the loss mirroring the solubility decrease. Although due to the much lower absolute concentration of DL-Asn.H_2O and MFA in the system, the productivity is much lower in comparison to $NaBrO_3$, going below the target *P* for 20 °C. The slurry density presents a similar shape to that of $NaBrO_3$, although to a lesser magnitude due to the much lower concentration of DL-Asn.H_2O and MFA in the system and so smaller than the considered maximum slurry density for a system. This influence of absolute concentration is affecting

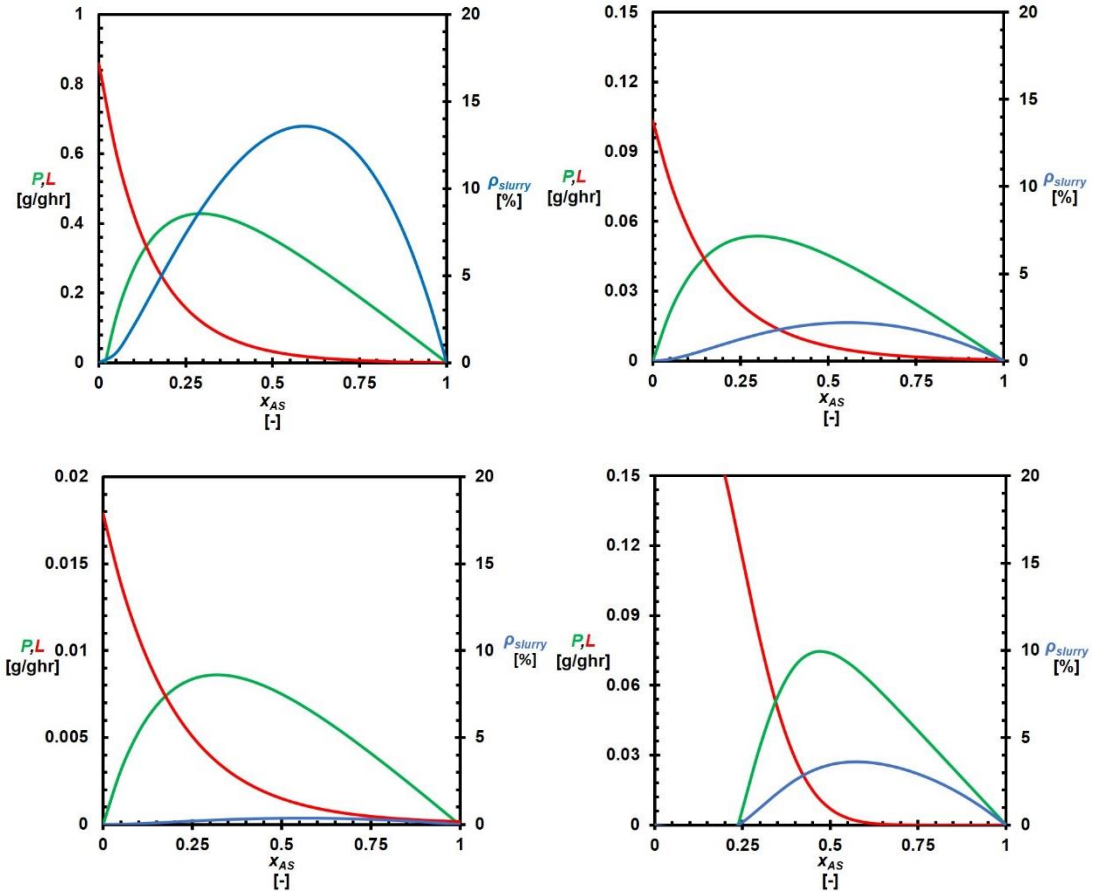

Figure 4-6: The predicted productivity (—), loss (—) and slurry density (—) in a continuous antisolvent crystallization process with a saturated feed and a pure antisolvent feed as a function of antisolvent fraction at 20°C (293K) for $NaBrO_3$ in water/EtOH (top), DL-Asn.H_2O in water/EtOH (2nd), MFA in EtOH/water (3rd) and LOV in AcO/water (bottom) (left). The residence time for each system is 25 minutes (0.417 hours).

both productivity and slurry density for MFA with both specifications being again much lower than for the previous system. As the shape of the phase diagram is similar to that of the previous systems, the shape of the productivity, loss and slurry density curves are similar.

For LOV in AcO-water the productivity and loss predictions are uniquely different to the other systems, with the influence of the solubility increase at lower antisolvent fractions being visible. At the lower fractions, there is no productivity due to the dilution line being below the solubility line so inducing no

supersaturation. As it increases, the solubility becomes lower than absolute concentration of LOV in the system so making recrystallization thermodynamically feasible and so increasing the predicted productivity. Due to the steepness of the solubility decrease, the productivity rises to an expected maximum within a smaller antisolvent range than in previous systems. The range of the predicted maximum productivity is also much less than in the previous systems with the difference in solubility and concentration quickly decreasing at the higher fractions. From this observation, the region to achieve productivity optimization is much smaller and so requires detailing the requirement for better control as going further than this maximum will reduce the overall productivity of the system and so the process yield. The slurry density also resonates previous systems with it reaching a maximum from the point at which crystallization is thermodynamically feasible.

To optimize a continuous antisolvent crystallization process, specific parameters such as productivity, yield and slurry density are conditioned for the general process conditions of temperature and antisolvent. As the yield Y of system is directly related to the productivity and loss, it can be predicted from the following equation:

$$Y = \frac{P_{x_{AS}}}{L_{x_{AS}} + P_{x_{AS}}} * 100 \qquad 78$$

With Y being in units of % with both the productivity $P_{x_{AS}}$ and loss $L_{x_{AS}}$ in units of g/ghr.

From this perception, it would be reasonable to assume that by adding more antisolvent the loss is reduced significantly as shown in Figure 4-6. Although from Figure 4-6, the productivity is shown to reduce sub-optimally at higher antisolvent fractions with the slurry density also increasing which would inevitably cause insufficient mixing and poor flowability of the slurry so reducing overall yield.

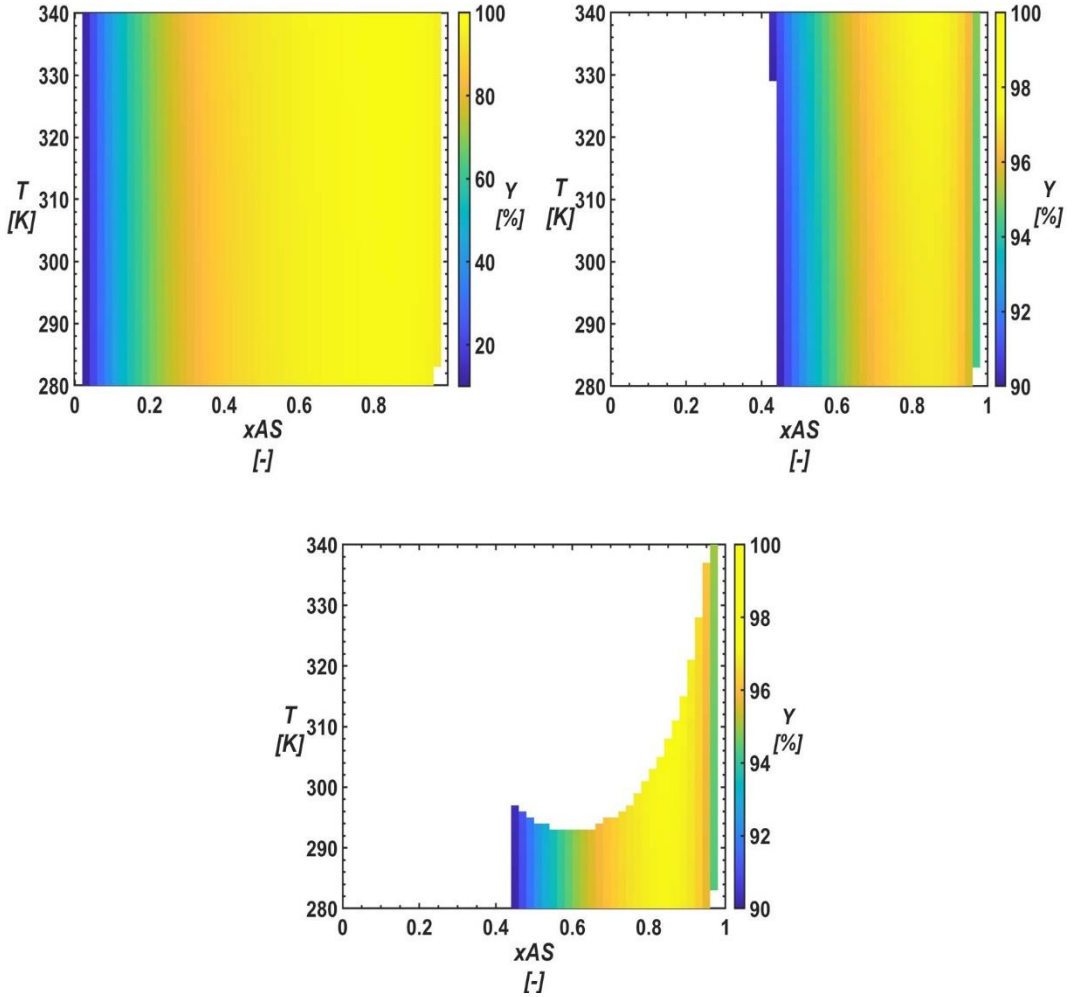

Figure 4-7: The optimal antisolvent and temperature regions for a continuous antisolvent crystallization of $NaBrO_3$, using the specifications: Y ≥ 90%, P ≥ 0.012 g/ghr and $\rho_{slurry} \leq 20\%$ are shown 3 scenarios (from top left to bottom): if only the productivity specification was followed; if both the productivity and yield specifications are applied; if all specification are applied. The colour scheme represents the change in yield Y as a function of both temperature T and antisolvent fraction x_{AS}.

Figure 4-7 presents the optimal antisolvent regions for continuous crystallization of $NaBrO_3$ at varying temperatures for each system based of the process requirements: $Y \geq 90\%$, $P_{x_{AS}} \geq 0.012$ g/ghr,$\rho_{Slurry} \leq 20\%$. The coloured region for each system represents specific antisolvent and temperature combinations in which the specific operating conditions are met the. The white regions represent

the antisolvent and temperature values at which the operating conditions are not met.

For $NaBrO_3$, when only the productivity specification is imposed on the crystallization, the optimal antisolvent and tempetrure regions is not influenced significantly, with only the extremely low and high antisolvent regions being omitted. Including the yield specification, temperature and antisolvent regions that do not meet the specification are omitted. Due to this, $x_{AS} < 0.4$ do not meet the 90% yield threshold. When including the slurry density specification, further antisolvent and temperature regions are omitted from the optimal crystallization regions. At the lower temperatures and increasing x_{AS}, this optimal region is maintained from previously. As the temperature increases, the optimal x_{AS} region reduces significantly with the larger solid amount likely to reduce the stirrability of the process. As the slurry density is heavily dependent on the P, this variable will increase significantly at higher temperatures due to the higher overall concentration. This results in a higher density than that of the specifications

Like $NaBrO_3$, the region in which the specifications are met for DL-Asn.H_2O (Figure 4-8) are at a much higher antisolvent fraction than when recrystallization is thermodynamically feasible. This would be due to the much lower overall concentration present in solution so it is not until higher fractions that the yield becomes an acceptable level. The impact of temperature is shown more through the maximum predicted yield with it only reaching a maximum between $0.8 < x_{AS} < 0.85$ at only $335 \leq T \leq 340$, unlike $NaBrO_3$ where it predominately dictated the optimal regions through the slurry density. The reduction of the solubility due to increased antisolvent is the major cause of this lower maximum yield with the systems loss remaining higher than that presented of $NaBrO_3$. Due to much lower slurry density at increasing fractions as shown in Figure 4-6 compared to $NaBrO_3$, the increasing temperature does not significantly influence the slurry density enough to dictate the optimal regions for continuous recrystallization. Therefore, allowing an optimal crystallization at higher temperatures in comparison to $NaBrO_3$.

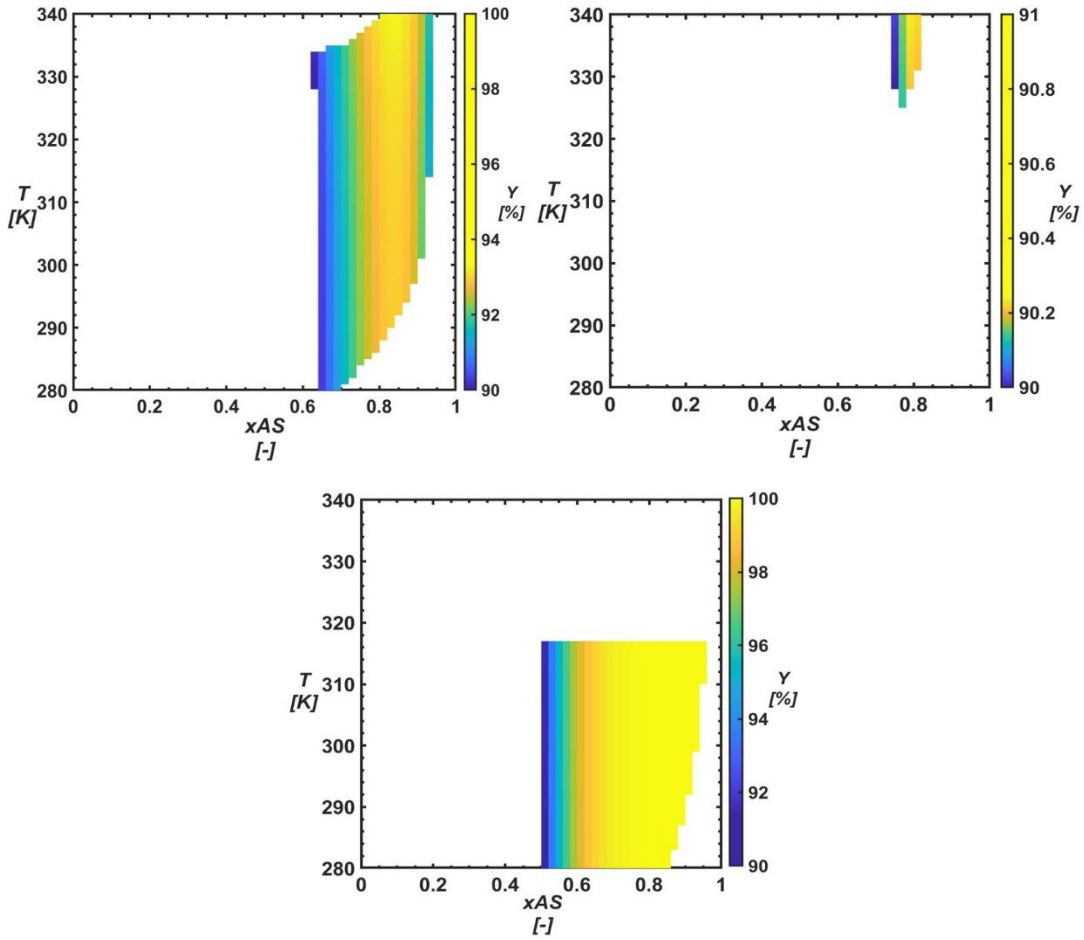

Figure 4-8: The optimal antisolvent and temperature regions for a continuous antisolvent crystallization of DL-Asn.H2O (top left),MFA (top right) and LOV (bottom) using the specifications: Y ≥ 90%, P ≥ 0.012 g/ghr and $\rho_{slurry} \leq 20\%$. The colour scheme represents the change in yield Y as a function of both temperature T and antisolvent fraction x_{AS}.

In contrast to the previous systems, MFA has a very similar phase diagram and productivity profile although has a much smaller optimization region only achievable at much higher temperatures and x_{AS} and even then within a much smaller optimization region. Only at the highest temperatures of 340K< T <350K and antisolvent fractions of 0.7 < x_{AS} <0.8 is an optimal process achievable. For this the extremely low solubility and so low overall solution concentration significantly reduces the region in which a high productivity and yield are achieved. This much lower overall concentration is too low for the slurry density to be considered impactful the optimization like it did for $NaBrO_3$. From Figure

4-6, there are no antisolvent or temperature regions, which produce a yield similar to that of the previous systems.

The region of optimization for LOV in AcO/water is only shown at temperatures below 318K due to the low boiling point of AcO. At the lower temperatures, the region in which an optimized continuous crystallization is achievable is similarly large to that of $NaBrO_3$. This is expected with extremely low solubility of LOV in higher x_{AS}. Similar to DL-Asn.H_2O, the slurry density does not have a significant impact as it did for $NaBrO_3$ with no regions at higher temperatures being cut off unless above the maximum set temperature. The optimal region is achieved at x_{AS} = 0.5 for all temperatures with the productivity and so yield quickly increasing once the system becomes thermodynamically feasible. Due to the extreme decrease in solubility between x_{AS} = 0.25 and x_{AS} = 0.5 the productivity increases and so quickly reaching a region of maximum yield at all temperatures past x_{AS} = 0.65. At the highest x_{AS} values the productivity reduces and so becoming sub-optimal. As the temperatures increase, P increases and so increasing the x_{AS} where the system becomes sub-optimal. The system is able to reach high levels of yield as similarly to that of NaBrO3 due to the extremely low solubility of LOV in water so causing a sharp reduction in solubility and increasing the obtainable product due to the linear dilution line.

4.5 Discussion

By applying the methodology above, antisolvent phase diagrams can be accurately described using this alternative method to what is commonly applied. The methodology outlined above works for systems which observe either the standard antisolvent phase diagram or one similar to LOV with an initial synergistic increase in solubility.

Process specifications like productivity and yield across the entire antisolvent phase diagram allow identification of optimal regions for a highly efficient continuous crystallization process. A workflow is presented in Figure 4-9 to provide a systematic approach to accurately develop antisolvent phase diagrams for continuous antisolvent crystallizations.

Large scale solvent screening is well known to occur for initial process design, with this systematically done through dropwise addition of a specific solvent into a known amount of the solute used. Although this is not as accurate as other solubility determination methods, it provides a fast way to determine a solute concentration to begin with before turbidity experiments. Solvents with similar functional groups and polarities to that of the solute exhibit high solubilities and so are the ideal candidates for solvent screening, with this exhibited from the solubilities for each system in Figure 4-2. Hazardous solvents are sometimes used as a preliminary solvent choice for a system depending on the physiochemical properties of the system like polymorphic form obtained. Following the ICH guidelines for solvent classes, specific hazards related to the solvent must be deemed acceptable in order to continue as well as solvents which must not be used further[3].

Once suitable solvents are selected, turbidity measurements follow which allow accurate acquisition of multiple saturation temperatures for each system as well as different antisolvent fractions. Solids with a high solubility in water generally have low solubilities in organic solvents as well as the opposite also being the case. As most systems either present one of the phase diagrams presented in this work, a minimum of four different fractions would be required to capture the majority of the solubility decrease due to the antisolvent presence.

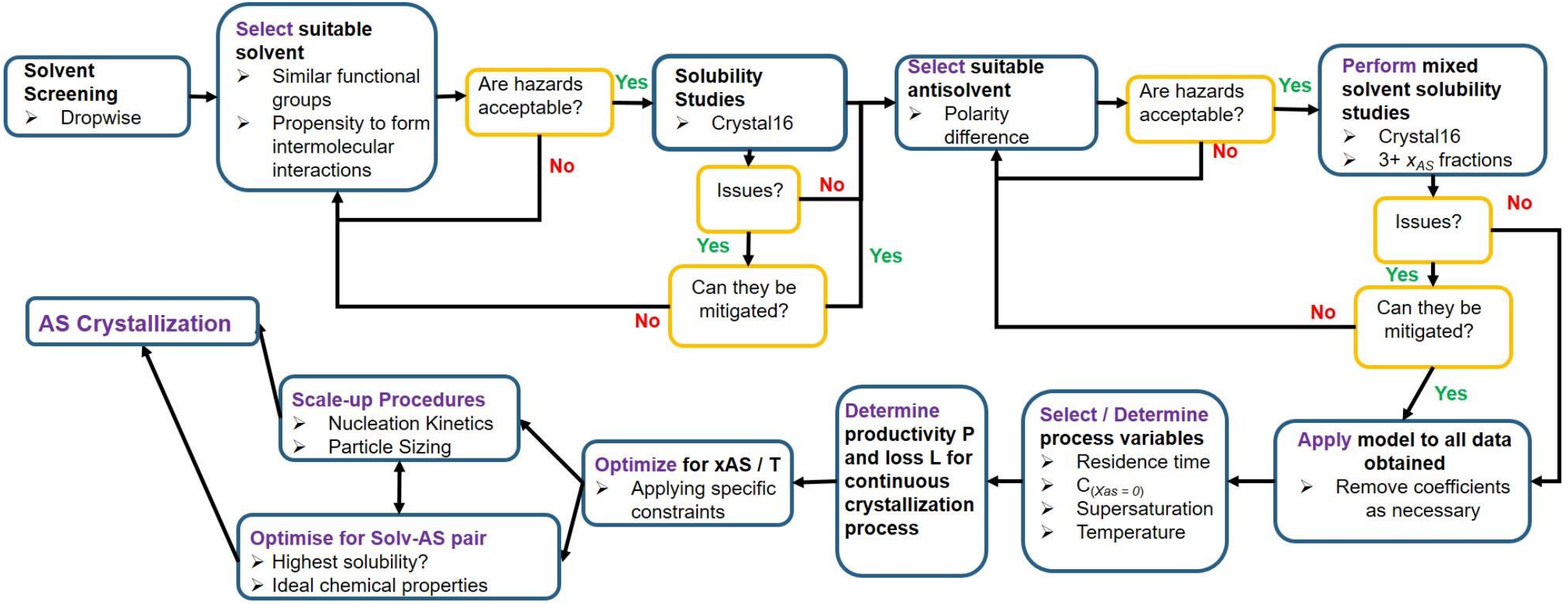

Figure 4-9: Workflow for the Design of Antisolvent Phase Diagrams, and the specific steps required towards detailed design of a continuous antisolvent crystallization. Each action performed is identified with the action highlighted in purple, with preceding criteria of acceptability highlighted by a yellow outlined box with different routes dependent on the choice and acceptance criteria.

Specific issues such as crowning are known to occur in systems with high solubility, although in some situations systems with different morphologies such as needles are known to also exhibit crowning issue due to their high propensity to agglomerate. This issue reduces the concentration of solute in the system and so reduces the measured solubility, identified commonly by systematic reductions in clear points at repeating cycles and so must be avoided. Specific ways of reducing this are increasing the solvent amount in the system or increasing stirring rates at higher temperatures. Synergistic relationships are common between solvents with it not only shown in solvent-water systems as has been presented here[101]. The maxima is both compound and solvent mixture dependent so could occur at any solvent fraction. There are computational methods such as SAFT-gamma Mie[6] and COSMOtherm[8] to predict synergistic relationships although their accuracy can be inconsistent and require further computational processing ability.

Once the solubility data is collected in different temperatures and antisolvent fractions, applying equation 71 allows the construction of the antisolvent phase diagram at different temperatures. The presence of antisolvent is assumed to have negligible impact on the temperature dependence of a system, in comparison to the solubility decrease. The model paired with productivity and yield calculations identifies optimal antisolvent and temperature regions for a continuous antisolvent system to be effective.

Applying this method speed up the path towards the most optimal systems. From the optimal regions, larger scale as well as mere detailed process design can be undertaken as shown from the final boxes in Figure 4-9, with these experiments consisting of both nucleation and growth rate calculations.

4.6 Conclusion

The accurate measurement of antisolvent solubilities as a function of antisolvent fraction and temperature is enabled by clear point measurements, even using a small number of experiments. A simple empirical equation was used to model

these experimental results in order to present the various antisolvent crystallization phase diagrams. The phase diagrams of $NaBrO_3$ and DL-ASN in water with antisolvent ethanol and MFA in ethanol with antisolvent water all resemble the typical antisolvent crystallization phase diagram with a significant reduction in solubility at small antisolvent fractions. LOV in acetone with antisolvent water shows a solubility increase with antisolvent fraction before a strong decrease. By this approach the basic design of API-solvent-antisolvent systems is performed by a less labor-intensive means than is required for the more commonly used gravimetric method. Using such a phase diagram, we can perform a basic design and optimization of a continuous antisolvent crystallization following preselected boundaries on the process parameters productivity, yield and suspension density, resulting in specific antisolvent and temperature regions for optimal operation.

4.7 Acknowledgements

The authors would like to acknowledge financial support from the Strathclyde Institute of Physical Biomedical and Sciences and the Doctoral Training Centre in Continuous Manufacturing and Crystallization (CMAC). I would also like to thank Johannes Hoffmann for his Sodium bromate and DL-Asparagine monohydrate solubility data.

4.8 References

1. Wouters OJ, McKee M, Luyten J. Estimated Research and Development Investment Needed to Bring a New Medicine to Market, 2009-2018. *JAMA - J Am Med Assoc*. 2020;323(9):844-853. doi:10.1001/jama.2020.1166
2. Savjani KT, Gajjar AK, Savjani JK. Drug Solubility: Importance and Enhancement Techniques. *ISRN Pharm*. 2012;2012(100 mL):1-10. doi:10.5402/2012/195727
3. Committee for Human Medicinal Products. ICH guideline Q3C (R5) on impurities: Guideline for Residual Solvents. *Int Conf Harmon Tech Requir Regist Pharm Hum Use*. 2015;44(October 2002):24.
4. Lewis A, Seckler M, Kramer H, Rosmalen G. Melt Crystallisation. In: *Industrial Crystallization: Fundamentals and Applications*. ; 2015:261-281.

5. Lewis A, Kramer H, Seckler M. Thermodynamics, Crystallzation Methods and Supersaturation. In: *Industrial Crystallization: Fundamentals and Applications*. ; 2015:1-25.

6. Spyriouni T, Krokidis X, Economou IG. Thermodynamics of pharmaceuticals: Prediction of solubility in pure and mixed solvents with PC-SAFT. *Fluid Phase Equilib*. 2011;302(1-2):331-337. doi:10.1016/j.fluid.2010.08.029

7. Loschen C, Klamt A. Solubility prediction, solvate and cocrystal screening as tools for rational crystal engineering. *J Pharm Pharmacol*. 2015;67(6):803-811. doi:10.1111/jphp.12376

8. Tung HH, Tabora J, Variankaval N, Bakken D, Chen CC. Prediction of pharmaceutical solubility via NRTL-SAC and COSMO-SAC. *J Pharm Sci*. 2008;97(5):1813-1820. doi:10.1002/jps.21032

9. Myerson AS, Erdemir D, Lee AY. Thermodynamic Concepts and Ideal Solubility. In: *Handbook of Industrial Crystallization*. ; 2019:1-31.

10. Zumdahl S. The Equilibrium Constant. In: *Chemistry*. 5th ed. Houghton Mifflin; 1999:578-620.

11. Xu R, Huang C. Solubility Modeling and Solution Thermodynamics of 4-Amino-2,6-Dimethoxypyrimidine in Cosolvent Mixtures of Methanol, Ethanol, Isopropanol, and N, N-Dimethylformamide + Water. *J Chem Eng Data*. 2018;63(11):4234-4240. doi:10.1021/acs.jced.8b00719

12. Zhao H, Xu H, Yang Z, Li R. Solubility of 3,4-dichloronitrobenzene in methanol, ethanol, and liquid mixtures (methanol + water, ethanol + water): Experimental measurement and thermodynamic modeling. *J Chem Eng Data*. 2013;58(11):3061-3068. doi:10.1021/je400507u

13. Jia L, Yin Q. Insights into the mechanism of concomitant nucleation of form II and ethanol solvate of spironolactone in cooling crystallization †. 2018:9697-9706. doi:10.1039/c7ra13094e

14. Yang Y, Tang W, Li X, et al. Solubility of Benzoin in Six Monosolvents and in Some Binary Solvent Mixtures at Various Temperatures. *J Chem Eng Data*.

2017;62(10):3071-3083. doi:10.1021/acs.jced.7b00238

15. Gmehling J, Kleiber M. *Vapor-Liquid Equilibrium and Physical Properties for Distillation*.; 2014. doi:10.1016/B978-0-12-386547-2.00002-8

16. Seader JD, Henley E, Roper DK. *Seperation Process Principles-Chemical and Biochemical Operations*. 3rd ed. John Wiley & Sons, Inc.; 2011.

17. Smith JM, Ness HC Van, Abbot MM, Swihart MT. *Introduction to Chemical Engineering Thermodynamics Eight Edition*.; 2018.

18. Abbot M, Berthold J, de Loos T. *Models for Thermodynamic and Phase Equilibria Calculations*. 1st ed. (Sandler S, ed.).; 1994.

19. Vagenas GK, Marinos-Kouris D. Use of the Wilson equation for the prediction of the sorptional equilibrium of sugar-based foodstuffs. *Fluid Phase Equilib*. 1992;78(C):191-207. doi:10.1016/0378-3812(92)87034-K

20. Dojcanský J, Bafrncová S, Surový J. Application of the Wilson Equation with Binary Parameters to the Prediction of the Isothermal Vapour-Liquid Equilibrium Data of Ternary and Quaternary Systems in the Assessment of the Polar Solvent in Extractive Distillation. 2001;55(2):71-74.

21. Sadeghi R. Extension of the Wilson model to multicomponent polymer solutions: Applications to polymer-polymer aqueous two-phase systems. *J Chem Thermodyn*. 2005;37(1):55-60. doi:10.1016/j.jct.2004.08.007

22. von Raumer M, Hilfiker R. A Short Introduction to Polymorphism and Solid-State Development. In: *Polymorphism in the Pharmaceutuical Industr: Solid Form and Drug Development*. 1st ed. ; 2019:1-23.

23. Vrani E. Amorphous Pharmaeutical Solids. *Bosn J Basic Med Sci*. 2004;4(3):35-39.

24. Aitipamula S, Banerjee R, Bansal AK, et al. Polymorphs, salts, and cocrystals: What's in a name? *Cryst Growth Des*. 2012;12(5):2147-2152. doi:10.1021/cg3002948

25. Lewis A, Seckler M, Kramer H, Rosmalen G. Polymorphism. In: *Industrial Crystallization: Fundamentals and Applications*. ; 2015:303-319.

26. Cruz-Cabeza AJ, Reutzel-Edens SM, Bernstein J. Facts and fictions about

polymorphism. *Chem Soc Rev*. 2015;44(23):8619-8635. doi:10.1039/c5cs00227c

27. Lee EH. A practical guide to pharmaceutical polymorph screening & selection. *Asian J Pharm Sci*. 2014;9(4):163-175. doi:10.1016/j.ajps.2014.05.002
28. Cesur S, Gokbel S. Crystallization of mefenamic acid and polymorphs. *Cryst Res Technol*. 2008;43(7):720-728. doi:10.1002/crat.200711119
29. Ferrari ES, Davey RJ, Cross WI, Gillon AL, Towler CS. Crystallization in polymorphic systems: The solution-mediated transformation of β to α glycine. *Cryst Growth Des*. 2003;3(1):53-60. doi:10.1021/cg025561b
30. Padrela L, Zeglinski J, Ryan KM. Insight into the Role of Additives in Controlling Polymorphic Outcome: A CO2-Antisolvent Crystallization Process of Carbamazepine. *Cryst Growth Des*. 2017;17(9):4544-4553. doi:10.1021/acs.cgd.7b00163
31. Kulkarni SA, McGarrity ES, Meekes H, Ter Horst JH. Isonicotinamide self-association: The link between solvent and polymorph nucleation. *Chem Commun*. 2012;48(41):4983-4985. doi:10.1039/c2cc18025a
32. Joel Bernstein, Roger J. Davey, Jan-Olav Henck. Concomitant Polymorphs. *Angew Chemie Int Ed*. 1999;38(23):2440-3461. doi:10.1002/(SICI)1521-3773(19991203)38:23<3440::AID-ANIE3440>3.0.CO;2
33. Teychené S, Biscans B. Nucleation kinetics of polymorphs: Induction period and interfacial energy measurements. *Cryst Growth Des*. 2008;8(4):1133-1139. doi:10.1021/cg0609320
34. Jiang S, Horst JH, Jansens PJ. Concomitant Polymorphism of o-Aminobenzoic Acid in Antisolvent Crystallization. *Cryst Growth Des*. 2008;8(1):37-43.
35. ter Horst JH, Kramer HJM, Jansens PJ. A New Molecular Modeling Approach To Predict Concomitant Nucleation of Polymorphs. *Cryst Growth Des*. 2002;2(5):351-356.
36. Black S, Muller F, Fielding M. A Practical Approach for Using Solubility to

Design Cooling Crystallisations. *Org Process Res Dev*. 2009;13:1315-1321.

37. Lewis A, Seckler M, Kramer H. Batch Crystallisation. In: *Industrial Crystallization*. ; 2015:178-191.

38. Zhang D, Liu L, Xu S, Du S, Dong W, Gong J. Optimization of cooling strategy and seeding by FBRM analysis of batch crystallization. *J Cryst Growth*. 2018;486:1-9. doi:10.1016/j.jcrysgro.2017.12.046

39. Zhang F, Liu T, Chen W, Ma CY, Wang XZ. Seed Recipe Design for Batch Cooling Crystallization with Application to l -Glutamic Acid. *Ind Eng Chem Res*. 2019;58(8):3175-3187. doi:10.1021/acs.iecr.8b06006

40. Pinho SP, Macedo EA. Solubility of NaCl, NaBr, and KCl in water, methanol, ethanol, and their mixed solvents. *J Chem Eng Data*. 2005;50(1):29-32. doi:10.1021/je049922y

41. Svärd M, Nordström FL, Jasnobulka T, Rasmuson ÅC. Thermodynamics and nucleation kinetics of m-aminobenzoic acid polymorphs. *Cryst Growth Des*. 2010;10(1):195-204. doi:10.1021/cg900850u

42. Mullin J. Ideal and Non-ideal Solutions. In: *Nucleation*. 4th ed. ; 2001:98-100.

43. Bhamidi V, Kenis PJA, Zukoski CF. Probability of Nucleation in a Metastable Zone : Cooling Crystallization and Polythermal Method. doi:10.1021/acs.cgd.7b00875

44. Lenka M, Sarkar D. Determination of metastable zone width, induction period and primary nucleation kinetics for cooling crystallization of L-asparaginenohydrate. *J Cryst Growth*. 2014;408:85-90. doi:10.1016/j.jcrysgro.2014.09.027

45. Karpinski P, Baldyga J. Precipitation Processes. In: *Handbook of Industrial Crystallization*. 3rd ed. ; 2019:217-265.

46. Macedo EA. Solubility of amino acids, sugars, and proteins. *Pure Appl Chem*. 2005;77(3):559-568. doi:10.1351/pac200577030559

47. Giulietti M, Bernardo A. Crystallization by Antisolvent Addition and Cooling. *Cryst - Sci Technol*. 2012. doi:10.5772/50328

48. Chang J, Wang J, Diao Y, Wang W, Chen Q, Yu Z. Study on the solubility characteristic of the antisolvent crystallization of RDX. *J Phase Equilibria Diffus*. 2011;32(3):206-211. doi:10.1007/s11669-011-9872-3

49. Hansen TB, Qu H. Formation of Piroxicam Polymorphism in Solution Crystallization : E ff ect and Interplay of Operation Parameters. 2015. doi:10.1021/acs.cgd.5b01016

50. Hilfiker R, Blatter F, Szelagiewicz M. Screening for Polymorphs,Hydrates and Solvates. In: Hilfiker R, von Raumer M, eds. *Polymorphism in the Pharmaceutuical Industr: Solid Form and Drug Development*. 1st ed. ; 2019:241-256.

51. Lee S, Lee CH, Kim WS. Anti-solvent crystallization of L-threonine in Taylor crystallizers and MSMPR crystallizer: Effect of fluid dynamic motions on crystal size, shape, and recovery. *J Cryst Growth*. 2017;469:119-127. doi:10.1016/j.jcrysgro.2016.08.021

52. Ferguson S, Morris G, Hao H, Barrett M, Glennon B. Characterization of the anti-solvent batch, plug flow and MSMPR crystallization of benzoic acid. *Chem Eng Sci*. 2013;104:44-54. doi:10.1016/j.ces.2013.09.006

53. Mostafa Nowee S, Abbas A, Romagnoli JA. Antisolvent crystallization: Model identification, experimental validation and dynamic simulation. *Chem Eng Sci*. 2008;63(22):5457-5467. doi:10.1016/j.ces.2008.08.003

54. Vellema J, Hunfeld NGM, Van Den Akker HEA, Ter Horst JH. Avoiding crystallization of lorazepam during infusion. *Eur J Pharm Sci*. 2011;44(5):621-626. doi:10.1016/j.ejps.2011.10.010

55. Nagy ZK, Fujiwara M, Braatz RD. Modelling and control of combined cooling and antisolvent crystallization processes. *J Process Control*. 2008;18(9):856-864. doi:10.1016/j.jprocont.2008.06.002

56. Braatz RD. Advanced control of crystallization processes. *Annu Rev Control*. 2002;26 I:87-99. doi:10.1016/S1367-5788(02)80016-5

57. Barik K, Prusti P, Mohapatra SS. Single- and multi-objective optimisation for a combined cooling and antisolvent semi-batch crystallisation process

with an ACADO toolkit. *Indian Chem Eng*. 2020;62(3):287-300. doi:10.1080/00194506.2019.1677511

58. Lindenberg C, Krättli M, Cornel J, Mazzoti M, Brozio J. Design and optimization of a combined cooling/antisolvent crystallization process. *Cryst Growth Des*. 2009;9(2):1124-1136. doi:10.1021/cg800934h

59. Holaň J, Skořepová E, Heraud L, et al. Polymorphic Crystallization and Structural Aspects of Agomelatine Metastable Form X Prepared by Combined Antisolvent/Cooling Process. *Org Process Res Dev*. 2016;20(1):33-43. doi:10.1021/acs.oprd.5b00241

60. Zhang D, Xu S, Du S, Wang J, Gong J. Progress of Pharmaceutical Continuous Crystallization. *Engineering*. 2017;3(3):354-364. doi:10.1016/J.ENG.2017.03.023

61. Galan K, Eicke MJ, Elsner MP, Lorenz H, Seidel-Morgenstern A. Continuous preferential crystallization of chiral molecules in single and coupled mixed-suspension mixed-product-removal crystallizers. *Cryst Growth Des*. 2015;15(4):1808-1818. doi:10.1021/cg501854g

62. Pawar N, Agrawal S, Methekar R. Continuous Antisolvent Crystallization of α-Lactose Monohydrate: Impact of Process Parameters, Kinetic Estimation, and Dynamic Analysis. *Org Process Res Dev*. 2019;23(11):2394-2404. doi:10.1021/acs.oprd.9b00301

63. Sultana M, Jensen KF. Microfluidic continuous seeded crystallization: Extraction of growth kinetics and impact of impurity on morphology. *Cryst Growth Des*. 2012;12(12):6260-6266. doi:10.1021/cg301538y

64. Lawton S, Steele G, Shering P, Zhao L, Laird I, Ni XW. Continuous crystallization of pharmaceuticals using a continuous oscillatory baffled crystallizer. *Org Process Res Dev*. 2009;13(6):1357-1363. doi:10.1021/op900237x

65. Likozar B, Orehek J. Continuous Crystallization Processes in Pharmaceutical Manufacturing : A Review. 2021. doi:10.1021/acs.oprd.0c00398

66. Gong J, Tang W. Nucleation. *Pharm Cryst Sci Eng*. 2018:47-88. doi:10.1002/9781119046233.ch2

67. Sheikholeslamzadeh E, Rohani S. Solubility prediction of pharmaceutical and chemical compounds in pure and mixed solvents using predictive models. *Ind Eng Chem Res*. 2012;51(1):464-473. doi:10.1021/ie201344k

68. Lewis R, Evans W. Solutions and Solubility. *Chemistry (Easton)*. 2018:173-193. doi:10.1057/978-1-137-61037-9_11

69. Mane MB, Shinde SN. Vapor Liquid Equilibria: a Review. *Sci Revs Chem Commun*. 2012;2(2):158-171. www.sadgurupublications.com.

70. De Souza B, Keshavarz L, Steendam RRE, et al. Solubility Measurement and Thermodynamic Modeling of N-(4-Methylphenyl- Z-3-chloro-2-(phenylthio)propenamide in 12 Pure Solvents at Temperatures Ranging from 278.15 to 318.15 K. *J Chem Eng Data*. 2018;63(5):1419-1428. doi:10.1021/acs.jced.7b01011

71. Reus MA, Van Der Heijden AEDM, Ter Horst JH. Solubility Determination from Clear Points upon Solvent Addition. *Org Process Res Dev*. 2015;19(8):1004-1011. doi:10.1021/acs.oprd.5b00156

72. Brittain HG. Vibrational spectroscopic studies of cocrystals and salts. 2. The benzylamine-benzoic acid system. *Cryst Growth Des*. 2009;9(8):3497-3503. doi:10.1021/cg9001972

73. Surov AO, Terekhova I V., Bauer-Brandl A, Perlovich GL. Thermodynamic and structural aspects of some fenamate molecular crystals. *Cryst Growth Des*. 2009;9(7):3265-3272. doi:10.1021/cg900002q

74. Temperini MLA, Petrilli HM, Constantino VRL. Mefenamic Acid Anti-In fl ammatory Drug: Probing Its Polymorphs by Vibrational (IR and Raman) and Solid-State NMR Spectroscopies. 2014. doi:10.1021/jp500988k

75. Kato F, Otsuka M, Matsuda Y. Kinetic study of the transformation of mefenamic acid polymorphs in various solvents and under high humidity conditions. 2006;321:18-26. doi:10.1016/j.ijpharm.2006.04.020

76. Febra SA, Bernet T, Mack C, et al. Extending the SAFT-γ Mie approach to

model benzoic acid, diphenylamine, and mefenamic acid: Solubility prediction and experimental measurement. *Fluid Phase Equilib*. 2021;540:113002. doi:10.1016/j.fluid.2021.113002

77. Granberg RA, Rasmuson ÅC. Solubility of paracetamol in pure solvents. *J Chem Eng Data*. 1999;44(6):1391-1395. doi:10.1021/je990124v

78. Sun H, Gong JB, Wang JK. Solubility of Lovastatin in acetone, methanol, ethanol, ethyl acetate, and butyl acetate between 283 K and 323 K. *J Chem Eng Data*. 2005;50(4):1389-1391. doi:10.1021/je0500781

79. Mudalip SKA, Bakar MRA, Jamal P, Adam F. Prediction of Mefenamic Acid Solubility and Molecular Interaction Energies in Di ff erent Classes of Organic Solvents and Water. *Ind Eng Chem Res*. 2018. doi:10.1021/acs.iecr.8b02722

80. Wan Y, He H, Zhang P, et al. Solid-liquid equilibrium solubility and thermodynamic properties of cis-5-norbornene-endo-2,3-dicarboxylic anhydride in fourteen pure solvents and three binary solvents at various temperatures. *J Mol Liq*. 2020;297:111396. doi:10.1016/j.molliq.2019.111396

81. Shayanfar A, Velaga S, Jouyban A. Fluid Phase Equilibria Solubility of carbamazepine , nicotinamide and carbamazepine – nicotinamide cocrystal in ethanol – water mixtures. *Fluid Phase Equilib*. 2014;363:97-105. doi:10.1016/j.fluid.2013.11.024

82. Elliot JR, Lira CT. Introduction to Multicomponent Systems. In: *Introductory Chemical Engineering Thermodynamics*. ; 2012:369-411.

83. Gothard FA, Codrea Clobanu MF, Breban DG, Bucur CI, Sorescu G V. Predicting the Parameters in the Wilson Equations for Activity Coefficients in Binary Hydrocarbon Systems. *Ind Eng Chem Process Des Dev*. 1976;15(2):333-337. doi:10.1021/i260058a020

84. Hristova M, Donchev T, Kolev D, Baloch I, Georgiev H. Parameter'S Estimate in Wilson Equation. *Int Electron J Pure Appl Math*. 2015;7(3). doi:10.12732/iejpam.v9i1.4

85. Nti-Gyabaah J, Chmielowski R, Chan V, Chiew YC. Solubility of lovastatin in a family of six alcohols: Ethanol, 1-propanol, 1-butanol, 1-pentanol, 1-hexanol, and 1-octanol. *Int J Pharm*. 2008;359(1-2):111-117. doi:10.1016/j.ijpharm.2008.03.046

86. ter Horst JH, Schmidt C, Ulrich J. Fundamentals of Industrial Crystallization. In: *Handbook of Crystal Growth*. ; 2015:1317-1346.

87. Wichianphong N, Charoenchaitrakool M. Journal of Industrial and Engineering Chemistry Statistical optimization for production of mefenamic acid – nicotinamide cocrystals using gas anti-solvent (GAS) process. *J Ind Eng Chem*. 2018;62:375-382. doi:10.1016/j.jiec.2018.01.017

88. Sun H, Wang J. Solubility of lovastatin in acetone + water solvent mixtures. *J Chem Eng Data*. 2008;53(6):1335-1337. doi:10.1021/je800063d

89. Acree WE. Comments on "Solubility and Dissolution Thermodynamic Data of Cefpiramide in Pure Solvents and Binary Solvents." *J Solution Chem*. 2018;47(1):198-200. doi:10.1007/s10953-018-0714-3

90. Pramanik R, Bagchi S. Studies on solvation interaction: Solubility of a betaine dye and a ketocyanine dye in homogeneous and heterogeneous media. *Indian J Chem - Sect A Inorganic, Phys Theor Anal Chem*. 2002;41(8):1580-1587.

91. Ruidiaz MA, Delgado DR, Martínez F, Marcus Y. Solubility and preferential solvation of sulfadiazine in 1,4-dioxane+water solvent mixtures. *Fluid Phase Equilib*. 2010;299(2):259-265. doi:10.1016/j.fluid.2010.09.027

92. Ter Horst JH, Deij MA, Cains PW. Discovering New Co-Crystals. *Cryst Growth Des*. 2009;9(3):1531-1537.

93. Yoshida MI, Oliveira MA, Gomes ECL, Mussel WN, Castro W V., Soares CD V. Thermal characterization of lovastatin in pharmaceutical formulations. *J Therm Anal Calorim*. 2011;106(3):657-664. doi:10.1007/s10973-011-1510-0

94. Sullivan RA, Davey RJ, Sadiq G, et al. Revealing the roles of desolvation and molecular self-assembly in crystal nucleation from solution: Benzoic and p

-aminobenzoic acids. *Cryst Growth Des*. 2014;14(5):2689-2696. doi:10.1021/cg500441g

95. Shayanfar A, Fakhree MAA, Acree WE, Jouyban A. Solubility of lamotrigine, diazepam, and clonazepam in ethanol + water mixtures at 298.15 K. *J Chem Eng Data*. 2009;54(3):1107-1109. doi:10.1021/je8007827

96. Kongsamai P. Seperation of DL-Asparagine Enantiomers Using Crystallization Inhibitors. 2017.

97. Romero S, Escalera B, Bustamante P. Solubility behavior of polymorphs I and II of mefenamic acid in solvent mixtures. 1999;178:193-202.

98. Mack C, Hoffmann J, Sefcik J, ter Horst JH. Phase Diagram Determination and Process Development for Continuous Antisolvent Crystallizations. *Crystals*. 2022;12(8).

99. Black S, Dang L, Liu C, Wei H. On the measurement of solubility. *Org Process Res Dev*. 2013;17(3):486-492. doi:10.1021/op300336n

100. Zhang D, Xu S, Du S, Wang J, Gong J. Progress of Pharmaceutical Continuous Crystallization. *Engineering*. 2017;3(3):354-364. doi:10.1016/J.ENG.2017.03.023

101. Bustamante P, Navarro J, Romero S, Escalera B. Thermodynamic origin of the solubility profile of drugs showing one or two maxima against the polarity of aqueous and nonaqueous mixtures: Niflumic acid and caffeine. *J Pharm Sci*. 2002;91(3):874-883. doi:10.1002/jps.10076

102. Granberg RA, Rasmuson AC. Solubility of paracetamol in binary and ternary mixtures of water plus acetone plus toluene. *J Chem Eng Data*. 2000;45(3):478-483. doi:10.1021/je990272l

103. Pacheco DP, Martínez F. Thermodynamic analysis of the solubility of naproxen in ethanol + water cosolvent mixtures. *Phys Chem Liq*. 2007;45(5):581-595. doi:10.1080/00319100701313862

104. Wang L, Yang W, Song Y, Gu Y. Solubility Measurement, Correlation, and Molecular Interactions of 3-Methyl-6-nitroindazole in Different Neat Solvents and Mixed Solvents from T = 278.15 to 328.15 K. *J Chem Eng Data*.

2019;64(8):3260-3269. doi:10.1021/acs.jced.8b01256

105. Li X, Chen J, Chen G, Zhao H. Solubility modelling, solution thermodynamics and preferential solvation of hymecromone in binary solvent mixtures of: N, N -dimethylformamide + methanol, ethanol or n -propanol. *RSC Adv*. 2017;7(73):46378-46387. doi:10.1039/c7ra07587a

106. Sato S, Hata T, Tsujita Y. The structure of monacolin K, C24H36O5. *Acta Cryst*. 1984;40(1):195-198.

107. Turner TD, Hatcher LE, Wilson CC, Roberts KJ. Habit Modification of the Active Pharmaceutical Ingredient Lovastatin Through a Predictive Solvent Selection Approach. *J Pharm Sci*. 2019;108(5):1779-1787. doi:10.1016/j.xphs.2018.12.012

108. Naik JB, Mokale V. Preparation of Freeze-dried Solid Dispersion Powder using Mannitol to Enhance Solubility of Lovastatin and Development of Sustained Release Tablet Dosage Form. *Columbia Int Publ Am J Pharm Sci Nanotechnol*. 2014;1(1):11-26. doi:10.13140/2.1.4312.5769

109. Mikhail SZ, Kimel WR. Densities and Viscosities of Methanol-Water Mixtures. *J Chem Eng Data*. 1961;6(4):533-537. doi:10.1021/je60011a015

110. Perry RH, Green D. Densities of Aquous Organic Mixtures. In: *Perry's Chemical Engineers Handbook*. 7th ed. ; 1997:109-117. https://www.handymath.com/cgi-bin/isopropanolwghtvoltble5.cgi?submit=Entry.

111. Washburn EW. *International Critical Tables of Numerical Data of Physics, Chemistry, and Technology*. Vol 3. 1st ed. New York; 1930.

112. Thomas KT, McAllister RA. Densities of liquid-acetone-water solutions up to their normal boiling points. *AIChE J*. 1957;3(2):161-164. doi:10.1002/aic.690030206

113. Asghar SZ, Jouyban A, Martinez F, Rahimpour E. Solubility of naproxen in ternary mixtures of {ethanol + propylene glycol + water} at various temperatures: Data correlation and thermodynamic analysis. *J Mol Liq*. 2018;268:517-522. doi:10.1016/j.molliq.2018.07.082

114. Abbott M, Prausnitz J. Modelling the Excess Gibbs Energy. In: *Models for Thermodynamic and Phase Equilibria Calculations*. ; 1994:1-87.

115. Anslyn E, Dougherty D. Binding Forces. In: Murzdek J, ed. *Modern Physical Organic Chemistry*. 1st ed. ; 2006:168-177.

116. Editor G, Mccoustra M, Vendrell O, et al. Water–methanol mixtures: topology of hydrogen bonded network. *Phys Chem Chem Phys*. 2008;(10):5004-5011. doi:10.1039/b812223g

117. Yang B, Cao X, Lang H, Wang S, Sun C. Study on hydrogen bonding network in aqueous methanol solution by Raman spectroscopy. *Spectrochim Acta Part A Mol Biomol Spectrosc*. 2020;225:117488. doi:10.1016/j.saa.2019.117488

118. Valavi M, Svärd M, Rasmuson ÅC. Improving Estimates of the Crystallization Driving Force: Investigation into the Dependence on Temperature and Composition of Activity Coefficients in Solution. *Cryst Growth Des*. 2016;16(12):6951-6960. doi:10.1021/acs.cgd.6b01137

Chapter 5: Activity Coefficients in Phase Diagrams for Antisolvent Crystallization

Corin Mack[1], Jan Sefcik[2], Joop H. ter Horst[1,3]

1. University of Strathclyde, EPSRC Centre for Innovative Manufacturing in Continuous Manufacturing and Crystallization (CMAC), Strathclyde Institute of Pharmacy and Biomedical Sciences, Technology and Innovation Centre, 99 George Street, Glasgow G1 1RD, United Kingdom

2. Department of Chemical and Process Engineering, University of Strathclyde, Glasgow

3. Laboratoire Sciences et Méthodes Séparatives, Université de Rouen Normandie, Place Emile Blondel, 76821 Mont Saint Aignan Cedex, France

5.1 Abstract

Activity coefficients provide a qualitative method to describe deviation from ideality of a system due to molecular interactions, with the Wilson equation providing the quantitative backing. This study investigates the applicability of the Wilson binary and multicomponent equations to predict antisolvent phase diagrams for systems where synergistic relationships are observed. Using the model compound Lovastatin, the solubility and respective activity coefficients were determined for different solvent and solvent-antisolvent fractions. The binary Wilson interaction parameters were obtained for each solvent system. Modelling of the binary interaction parameters at different antisolvent fractions allowed the acquisition of the solute-antisolvent parameters. Using the obtained interaction parameters as well as literature sources, the antisolvent phase diagram for each system was modeled using the Wilson multicomponent equation, with it found to not be able to accurately model synergistic relationships in phase diagrams. The use of binary interaction parameters for each antisolvent fraction provided quantitative and qualitative information on how solute-solvent-antisolvent molecules interact in relation to antisolvent phase diagram construction.

5.2 Introduction

Within the pharmaceutical industry, determining solubilities is a major step necessary for the proper design and optimization of crystallization processes[36]. In order to reliably obtain the most effective solvent system, a solvent screening step is required to ascertain the optimal process yield and product characteristics, both strongly related to the solubility behaviour[55,2]. In order to arrive at the right solvent system, often it is needed to use mixed solvents. For such mixed solvent systems, this optimization can take much longer than standard single solvent systems due to the large variety of possible mixtures. By understanding the role that thermodynamic properties play, we are able to understand and predict how these systems behave, circumventing long and extensive screening procedures.

Activity coefficients describe the deviation from ideal thermodynamic behaviour of a system. By measuring the solubility of a compound in a specific solvent or solvent mixture, the activity coefficient is determined, as widely demonstrated on paracetamol[77,102].Development using activity coefficient analysis has led to a better understanding of the molecular interactions between solutes in both single and mixed solvent systems. From studies using Sulfadiazine in dioxane-water mixtures[91], the determined activity coefficients allowed preferential solvation analysis to be performed, resolving that sulfadiazine is preferentially solvated by the solvent mixture due to restructuring of the water molecules due to dioxane, increasing the solubility. This is common in solvent-water systems[102–104]. Whereas at high water fractions, the water molecules structure themselves around the sulfadiazine non-polar regions so reducing the solubility to its lowest point. Similar techniques have been applied to other molecules and solvent mixtures yielding similar results[90,103,105]. Although these techniques are popular throughout literature, quantitative methods such as the Wilson equation can provide means to understand molecules interactions, and how these affect the construction of antisolvent phase diagrams.

The Wilson equation is widely used throughout the chemical and process industry in construction of liquid-liquid, and to a lesser extent solid-liquid,

separation phase diagrams. Due to the effects of hydrogen bonding association between liquid-liquid molecules, regular solution theory could not be applied to accurately obtain thermodynamic property values to construct such diagrams so the Wilson model works at correcting such issues. Derived from local composition theory, interaction energy parameters are obtained when fitting directly to experimental data giving an interpretation of the change of interaction energies between molecules in specific systems. In solid-liquid systems, Wilson's equation is applied to only single solvent systems, obtaining the interaction energy parameters.

In the present work, the binary and multicomponent equations will be applied to different LOV-solvent-water systems to determine how well it can predict synergistic relationships in systems for antisolvent crystallization. Due to the different functional groups present within its molecular structure, its interaction with solvents and its respective antisolvent are suggested to be highly significant with little known about how these interactions for this specific molecule. This will be done by obtaining the activity coefficient for each system from ideal and experimental data. From this data, interpretations of the molecular interactions in each system will identify how a system is impacted from the increase in antisolvent presence and how this impacts the design of antisolvent systems, as well as the solvent selection process.

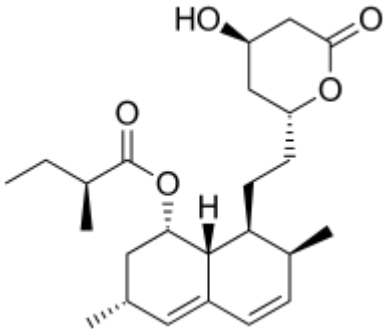

Figure 5-1: Molecular Structure of Lovastatin.

Lovastatin (Figure 5-1) has a highly complex molecular structure, containing specific functional groups important to its solubility and recrystallization in a variety of solvent systems. Although unlike many complex molecules, it is known to only have one polymorphic form with a needle like morphology.

5.3 Materials and Method

5.3.1 Materials

Lovastatin (LOV) was obtained from Molekula (>99%). Methanol (MeOH, ≥99%), Ethanol (EtOH, ≥99%), Propanol (PrOH, ≥99%), Isopropyl alcohol (IPA, ≥99%) and acetone (AcO, ≥99%) were obtained from VWR. All chemicals were used as received. Distilled and filtered water was obtained from a Millipore Water System.

5.3.2 Methods

5.3.2.1 Solubility Determination

Sample Preparation. A known amount of the solid Lovastatin was weighed into a 1.5 ml HPLC vial. A solvent mixture of a specific antisolvent fraction was prepared by weighing the proper amounts of solvents into a glass beaker. Once adequately mixed, a known amount of the prepared solvent mixture was pipetted into the pre-weighed vial containing the compound. The vial was then reweighed in order to accurately determine the exact composition of the sample both in units of mg/ml-solvent mixture and in mole fractions.

Solubility Measurement. The Crystal16 Multiple Reactor (Technobis Crystallization Systems, The Netherlands) was used to determine the clear point temperature for each prepared sample, similar to the procedure reported in literature[54]. If a suspension of solid particles is present in the vial, the transmission of light through the vial is hindered by the stirring suspension, whereas the light passes unhindered through a clear solution. To dissolve the crystals in the stirred (500 rpm) suspension, a heating rate of 0.3 °C/min was applied up to a pre-set high temperature in order to gradually increase the solubility. During the cooling of the solution (0.4 °C/min) to a pre-set low temperature, the solubility gradually decreased and at some point the sample recrystallized. Hold steps (30-60 min) were applied before and after each heating and cooling ramp to ensure adequate dissolution and recrystallization. For accuracy, three temperature cycles were performed. Every sample was subjected to an initial dissolution and subsequent cooling step prior to the first temperature cycle. The heating rate was slow enough to approximate the saturation

temperature of the overall composition in the vial by the average of the measured sample clear point temperatures.

The hold temperatures are dependent on the boiling and freezing point of the solvents used. For acetone, the high hold temperature used was 50 °C whereas for other solvents, temperatures of 10 °C below their respective boiling points were used. A minimum temperature of 0 °C allowed the recrystallization of the solutes within a reasonable timescale. Due to the possible slow degradation of Lovastatin at higher water concentrations, the total experimental time for the 3 temperature cycles was <24 hrs. The issue of crowning was reduced by reducing the headspace between the solution and vial cap by reducing the sample volume. In order to check for crowning, the vials were visually inspected during a high temperature hold step and also at the end of the measurement. Alongside this, crowning can be easily identified during analysis with the reduction of the clear points in subsequent cycles for a sample. If subsequent clear point measurements of a sample resulted in > 2 °C variation the results of that sample were discarded and a new experiment was undertaken.

The experimental solubilities C^* are given in units of mg/g solvent rather than units of mg/ml, as due to the non-linear change in volume at increasing antisolvent fractions, a volume-based metric for the solvent would be less accurate than that of mass-based method.

5.3.2.2 Solid Product Analysis

DSC. Differential Scanning Calorimetry (Polyma DSC 214, Netzsch) was used in order to determine the melting temperature T_m and heat of fusion ΔH_f of Lovastatin. A small amount (<5mg) of LOV is weighed into a metal DSC pan and sealed. A heating rate of 10 K/min from 298K up to 498K was used. In order to obtain accurate results, a large number of samples were used (N = 30) with each sample subjected to a heating cycle. For each sample, the T_m was taken as the melting onset during heating, and the ΔH_f was taken from the area of the resultant endotherm. The resulting ΔH_f and T_m were averaged and the standard deviation was determined as a measure for the accuracy.

XRPD. X-ray powder diffraction (Bruker D8 Advance II, USA) was used to identify the solid form of Lovastatin. A 98 mg/g suspension of Lovastatin in acetone (6 mL) was subjected to 3 heating and cooling cycles in the Crystalline Multiple Reactor setup (Technobis Crystallization Systems, Netherlands). The solids were then vacuum filtered and placed in an in-house oven set at 50 °C for 24 hours to ensure complete evaporation of solvent. The dried crystals and supplied material were then loaded onto a sample plate (polyamide film supported) and placed into the machine setup. The XRPD spectra was analysed over a 2θ range of 4 to 35° with a rate of 0.017°/sec.

5.4 Results

5.4.1 Lovastatin Solid-State Characterization

Lovastatin crystallizes in the $P2_12_12_1$ space group as confirmed by Sato et al[106], with it retaining this space group at lower temperatures[107]. To the best of our knowledge there are no other solid forms reported for lovastatin. The sharp peaks from the XRPD pattern in Figure 5-2 signify the pure crystalline form of lovastatin after recrystallization. This pattern was compared to that of the supplied lovastatin as well as reported patterns in literature[108], with no significant differences, signifying identical solid forms of the recrystallized, supplied and reported lovastatin[93].

Table 5-1: The experimental heats of fusion ΔH_f and melting temperature T_m for literature sources for LOV.

Source	N [-]	ΔH_f [kJmol^{-1}]	T_m [K]
This work	30	38.8 ± 2.1	443.7 ± 0.3
Nti-Gyabaah[71]	1	43.1	445.5
Tung[7]	1	36.5	444.3

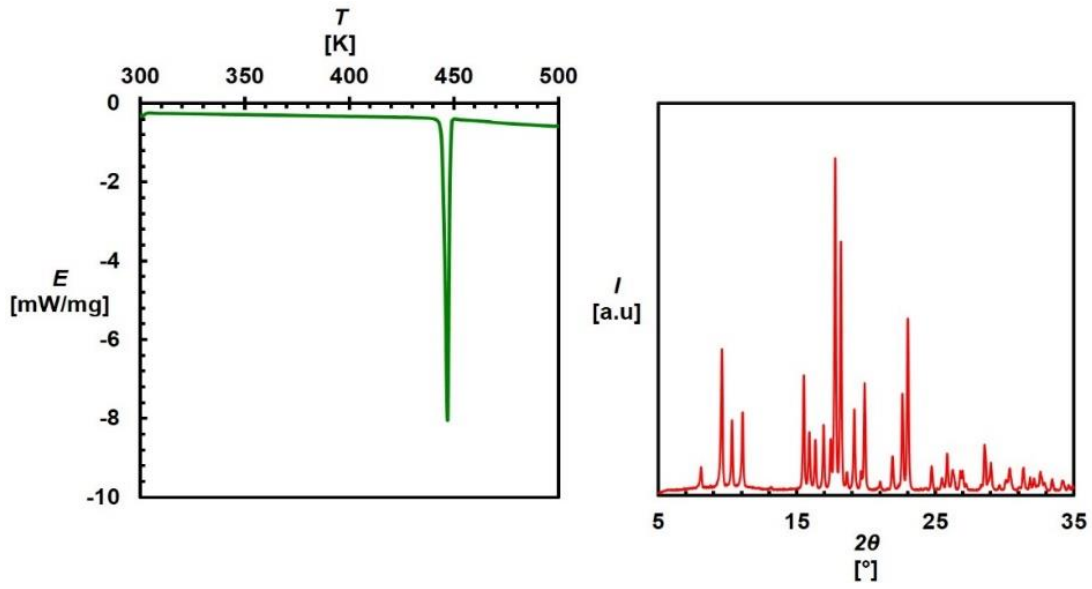

Figure 5-2: Typical DSC thermogram (left) and XRPD pattern (right) of LOV crystallized from acetone.

A typical thermal analysis by Differential Scanning Calorimetry (DSC) of lovastatin recrystallized from acetone is presented in Figure 5-2. The analysis of the 30 DSC analysis for LOV shows for all a single endotherm with a melting temperature T_m = 443.7 ± 0.3 K and a heat of fusion ΔH_f = 38.8 ± 2.1 kJ/mol. The values obtained from this analysis are slightly deviating from other sources using similar techniques (Table 5-1). This could be due to the point at which is used for the melting point, with the onset used in this analysis. Similarly, the purity of the sources could have impacted the heat of fusion measured.

5.4.2 Lovastatin Solubilities in Pure and Solvent-Water Systems

The experimental solubilities of LOV in different single solvent systems are provided in Figure 5-3(left). The solubility of LOV in AcO is much larger than that measured in the other solvents, with a c^* = 97 mg/g ($\ln x_3$ = -4.3) at 30 °C. Indeed, in solvents containing a ketone functional group, LOV is known to be much more soluble than in alcohols, with a similar solubility observed in this and previous studies[88,78].

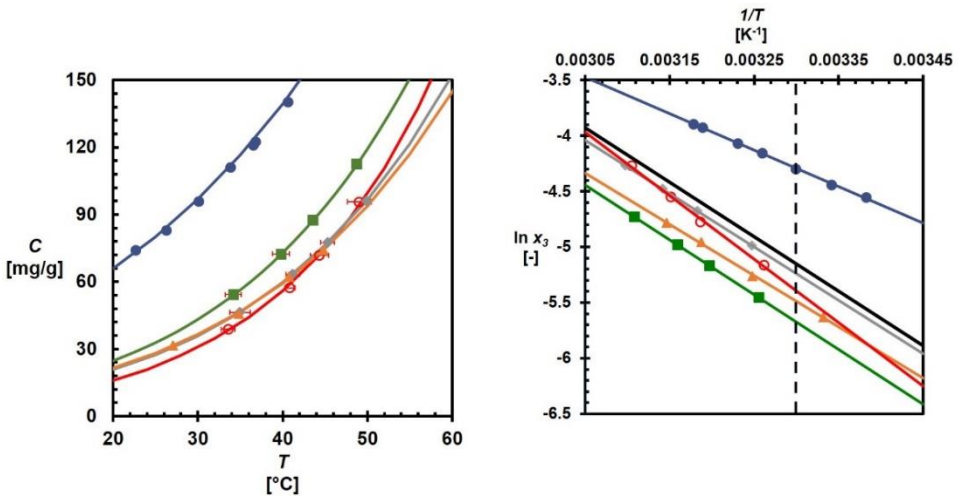

Figure 5-3: Single solvent lovastatin solubilities (left) and the van't Hoff plots (right) of Lovastatin in MeOH (■), EtOH (▲), PrOH (♦), IPA (○) and AcO (●). The vertical dashed line represents a temperature of 30°C (0.0033K^{-1}). The black line presented in the Van't Hoff plot represents the ideal solubility of LOV within the measured temperature range of all solvents. This was determined using equation 12 and the measured ΔH_f and T_m in Table 5-1. Red caps mark the error bars for each concentration. For some concentrations, the error bar is below the marker.

LOV in MeOH presents as the next highest solubility out of the measured solvents with c^*= 43 mg/g (ln x_3 = -5.7), although according to its respective Van't Hoff plot it is presented as having the lowest mol fraction out of all the measured solvents.

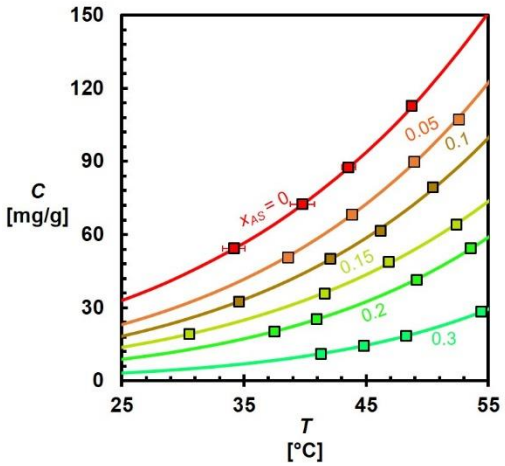
C
[mg/g]
T
[°C]
xAS = 0
0.05
0.1
0.15
0.2
0.3

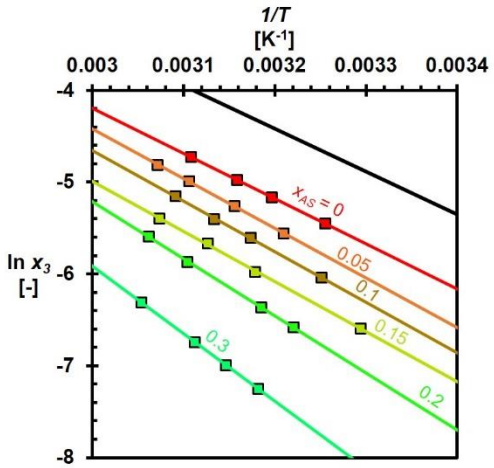
1/T
[K-1]
ln x3
[-]
xAS = 0
0.05
0.1
0.15
0.2
0.3

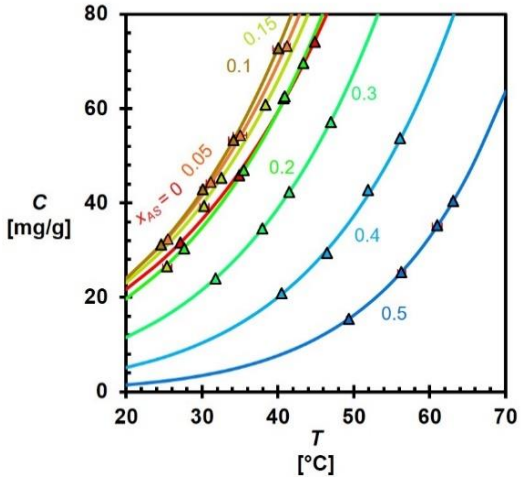
C
[mg/g]
T
[°C]
xAS = 0
0.05
0.1
0.15
0.2
0.3
0.4
0.5

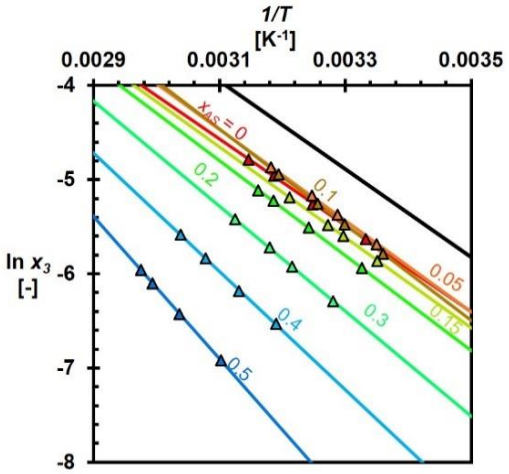
1/T
[K-1]
ln x3
[-]
xAS = 0
0.05
0.1
0.15
0.2
0.3
0.4
0.5

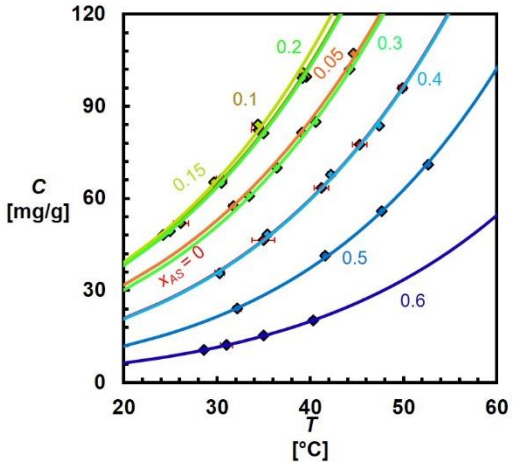
C
[mg/g]
T
[°C]
xAS = 0
0.05
0.1
0.15
0.2
0.3
0.4
0.5
0.6

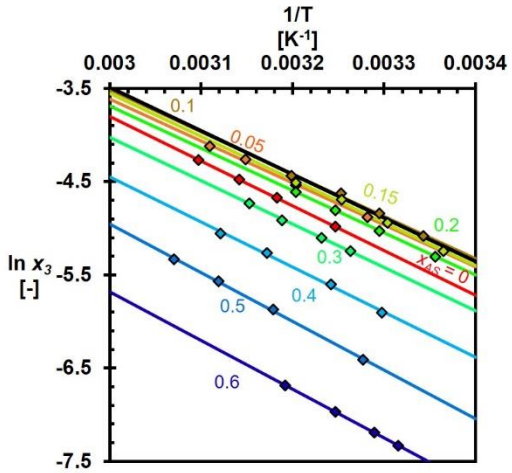
1/T
[K-1]
ln x3
[-]
xAS = 0
0.05
0.1
0.15
0.2
0.3
0.4
0.5
0.6

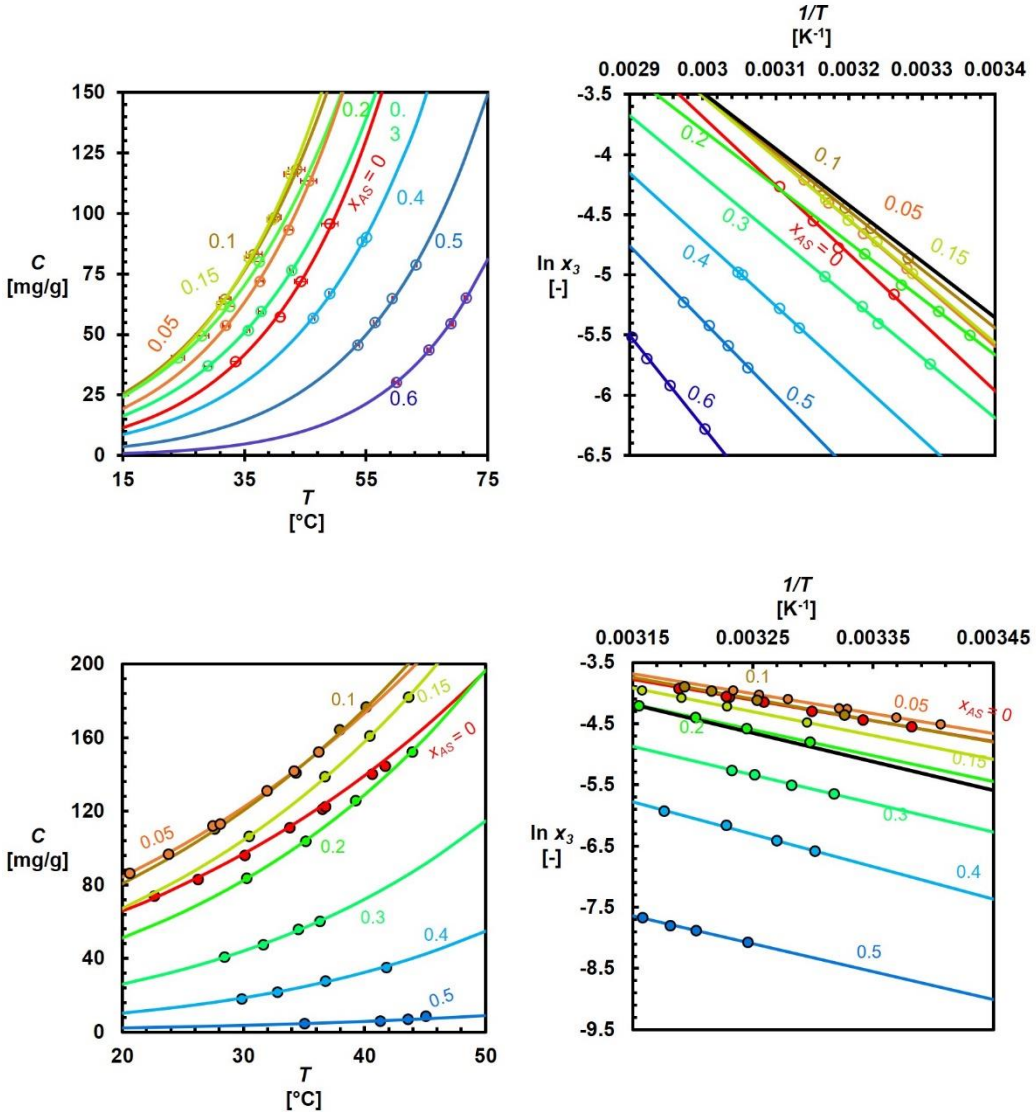

Figure 5-4: From top to bottom: the mixed solvent solubilities (left) and respective van 't Hoff plots (right) of LOV in MeOH-water (■), EtOH-water PrOH-water (♦), IPA-water (○) and AcO-water (●). The labels indicate the specific antisolvent mass fraction in the solvent mixture. The solid lines are the van't Hoff best fits. The solid black line represents the ideal solubility of LOV within the measured temperature range. Red caps mark the error bars for each concentration. For some concentrations, the error bar is below the marker.

The difference in m_w between each solvent causes this discrepancy with it also shown for LOV in EtOH and IPA, which present solubilities of c^* =37 mg/g (ln x_3 = -5.5) and c^* =30 mg/g (ln x_3 = -5.4) respectively at 30°C. The temperature dependence of LOV in these solvents (the slope in the van 't Hoff plot) stays

relatively consistent to one another, with the temperature independent part of the solubility of LOV in EtOH shown to be lower than the other solvents. For LOV in IPA, similar solubilities are obtained to that of PrOH within the same temperature range although its temperature dependence is clearly distinct from the other solvents.

Figure 5-4 shows the temperature dependent solubility using different water antisolvent fractions. The antisolvent mass fractions x_{AS} for each system were obtained from the following:

$$x_{AS} = \frac{m_{AS}}{m_s + m_{AS}} \qquad 79$$

Where the m_{AS} and m_s represent the mass of antisolvent and solvent within the mixture respectively. For all systems, the solubility increases with temperature at a constant antisolvent fraction (Figure 5-4, left). At increasing antisolvent fractions, the solubility of LOV in MeOH-water decreases significantly. This is similar behaviour commonly seen in literature for antisolvent crystallization phase diagrams[104,46]. The system shows a 28% decrease in solubility from x_{AS} = 0 to x_{AS} = 0.05 at 30 °C, with this degree in solubility reduction staying relatively consistent at increasing fractions with only a 25% further decrease between x_{AS} = 0.1 to x_{AS} = 0.15. At the highest antisolvent fraction measured, the saturation temperatures are higher than they are for the previous fractions with lower overall concentrations. It is because of this phenomenon that higher antisolvent fractions were not able to be measured due to the extremely low concentrations required to obtain reliable saturation temperatures within the limits of the solvent system restrictions such as boiling point.

The other measured systems show more complex behaviour as a function of the antisolvent fraction. Unlike in MeOH-water, LOV in EtOH-water shows a slight solubility increase with antisolvent fraction at low fractions. This phenomena also is reported to occur in other systems where water has been used as the antisolvent[95,81]. For LOV in EtOH-water at 30°C, the solubility increases by 16% going from x_{AS} = 0 to 0.1, with it reaching a maximum before reducing similarly to that of LOV in MeOH at increasing water fractions. As the antisolvent fraction

increases past x_{AS} = 0.1, the solubility decreases by 12% at x_{AS} = 0.15 with the degree of reduction moving to 19% up to x_{AS} = 0.2. Past this antisolvent fraction, the system responds with a sharp decrease in solubility, similarly to other systems throughout literature[58] at increasing antisolvent fractions.

This solubility increase with antisolvent fraction at low fractions is again presented with LOV in PrOH-water mixtures with it also presenting a maximum, with a much more significant degree. At T = 30°C from x_{AS} = 0, the solubility increases by 83% to a maximum at x_{AS} = 0.15. This is a much higher degree of influence caused by the antisolvent than that shown for both LOV in MeOH-water and EtOH-water mixtures. Once at this maxima, the solubility stays elevated in comparison to its solubility in pure PrOH, with a solubility of c^* = 64 mg/g (T = 30°C) at x_{AS} = 0.2 in compared to c^* = 36 mg/g at x_{AS} = 0. From this point the solubility non-linearly decreases towards zero, reaching its antisolvent free solubility at around x_{AS} = 0.4. Like previously, the solubility of LOV at higher antisolvent fractions could not be measured although due to the large increase in solubility observed at the lower antisolvent fractions this phenomenon does not occur until a much higher antisolvent fraction.

Following the trend of the primary alcohols, LOV in the secondary alcohol IPA-water presents a maximum in solubility as a function of the antisolvent fraction at constant temperature. The solubility of LOV in IPA-water significantly increases by 90% towards a maximum at an x_{AS} = 0.1 and solubility of c^* = 44 mg/g (T = 30°C). This system presents a much sharper increase in solubility than for the other systems. Similar to LOV in PrOH-water, the solubility stays relatively similar with a c^* = 42 mg/g (T = 30°C) at x_{AS} = 0.2, until beginning to significantly drop decrease at x_{AS} > 0.2. For LOV in IPA-water, the decrease in solubility past the maximum is similar to that of the other alcohols, with the solubility reaching the same value of the pure LOV-IPA mixture at $x_{AS} \approx 0.3$.

Although a significantly different system to the others, LOV in AcO-water presents a very similar antisolvent pattern with it experiencing a sharp increase in solubility at the low antisolvent fractions. At only a x_{AS} = 0.05, the system presents a maximum with a 20% increase to c^* = 122 mg/g (T = 30°C) from the

antisolvent free solubility of LOV. Although similar the sharp increase is only present in this system in comparison to the others with it quickly dropping off non-linearly towards x_{AS} = 1. As the antisolvent fraction increases, the solubility significantly reduces with it reaching its antisolvent free solubility at 0.15 < x_{AS} < 0.2. Going from an x_{AS} = 0.15, the solubility of LOV reduces by 23% at an x_{AS} = 0.2 to C = 82 mg/g (T = 30°C), followed by a more significant drop of 50% to an x_{AS} = 0.3. This sharp reduction influences the solubility so significantly that at the higher antisolvent fractions, accurate saturation temperatures and so solubilities are not able to be determined within the measureable region with the highest antisolvent measurement being x_{AS} = 0.5.

The solubility data is in the supplementary info (Section 5.9.1)

5.4.3 Modelling Activity Coefficients using the Wilson model

By determining the activity coefficient of these systems using the Van't Hoff equation, a perspective of the intermolecular interactions is provided. The activity coefficient quantifies the deviation from ideality due to molecular interactions present in the system. The activity coefficient γ_3 for each system respective of the solvent used is determined:

$$\gamma_3 = \frac{x}{x_{id}} \qquad 80$$

Where x is the experimentally determined solubility for LOV. Therefore for systems with known ideal solubility x_{id} along with measured solubilities x at a specific T, the activity coefficient $\gamma_3(x,T)$ of the system at concentration x=$x^*(T)$ and temperature T can be determined. As interactions between molecules influence the activity coefficient of a system, the Wilson equation is able to predict the magnitude of these interactions from these measured activity coefficients and provide quantifiable method to investigate the impact of the presence of antisolvent in each system.

The activity coefficient γ_3 at the saturation concentration as a function of temperature for LOV in each single solvent is presented in Figure 5-6. Within the measured temperature range, ln γ_3 has a close to linear relationship to T. Some systems in literature experience a similar nature to what is presented although

at temperatures closer to their melting point a more curved activity coefficient trend is perceived[18]. In Figure 5-6, the LOV-MeOH system shows the highest positive deviation from ideality (ln $\gamma_3 = 0$) in comparison to the other primary alcohols measured. LOV-EtOH shows a slightly lower positive deviation from ideality in comparison to MeOH, followed by LOV-PrOH. The γ_3 for LOV-IPA shows the largest change with temperature of the alcohol solvents.

The binary Wilson equation is expressed through the following:

$$\ln \gamma_3 = -\ln(x_3 + \Lambda_{13}x_3) - x_1\left(\frac{\Lambda_{13}}{x_1 + \Lambda_{13}x_2} - \frac{\Lambda_{31}}{x_3 + \Lambda_{31}x_1}\right) \quad 81$$

x_3 and x_1 represent the mole fraction of LOV and solvent in the solution respectively with Λ_{13} and Λ_{31} representing the interaction coefficients between the LOV and solvent molecules, with these constants being able to be further broken down into the form:

$$\Lambda_{13} = \frac{v_3}{v_1}\exp\left(-\frac{\lambda_{13}}{RT}\right) \quad 82$$

$$\Lambda_{31} = \frac{v_1}{v_3}\exp\left(-\frac{\lambda_{31}}{RT}\right) \quad 83$$

With v_1 and v_3 representing the molar volumes of the solvent and the solute LOV respectively in m^3/mol. The Wilson parameters λ_{13} and λ_{31} relate directly to the interaction energies between solute and solvent molecules.

The interaction parameters obtained through Wilson regression with the experimental data give two different situations and the magnitude of these interactions: λ_{13} refers to the energy exerted on a LOV molecule (3) by surrounding solvent molecules (1) and λ_{31} refers to the energy extrered on a solvent molecule (1) by surrounding LOV molecules (3) as shown in Figure 5-5. The magnitude and sign of these parameters influence the activity coefficients.

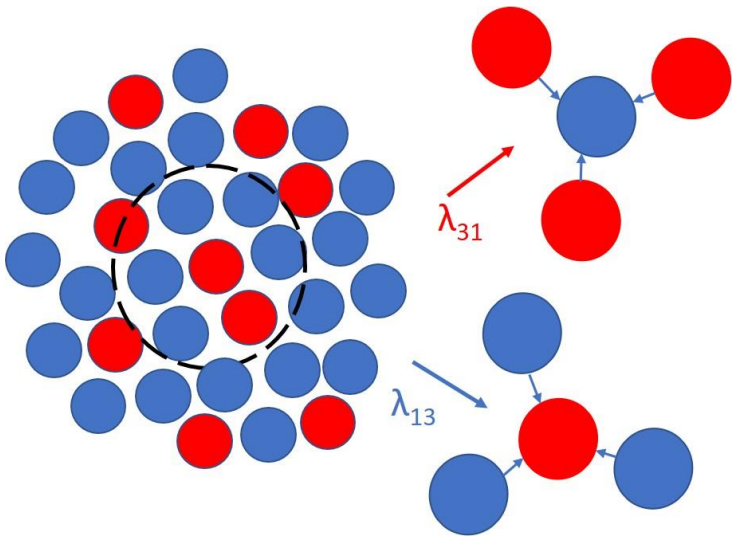

Figure 5-5: Visual representation of the application of Local Composition Theory between two dissimilar molecules within a system. The blue dots represent the solvent molecules whereas the red dots represent LOV molecules.

The experimental activity coefficients for each system are provided in Figure 5-6, comparing them to the predicted activity coefficients from the Wilson equation regression. The interaction parameters obtained from the regression are provided alongside the activity coefficient for each system. From equation 83, with $\lambda = 0$ there would be no interaction between respective molecules and so would present as an $\gamma_3 = 1$.

Figure 5-6(left) shows that the experimental activity coefficients are described well by the Wilson model for every system except LOV-AcO, with this strong correlation also represented through its relative standard deviation (σ). The σ represents whether the reported standard deviation provided alongside the absolute values for each system is small or large when comparing to the absolute value.

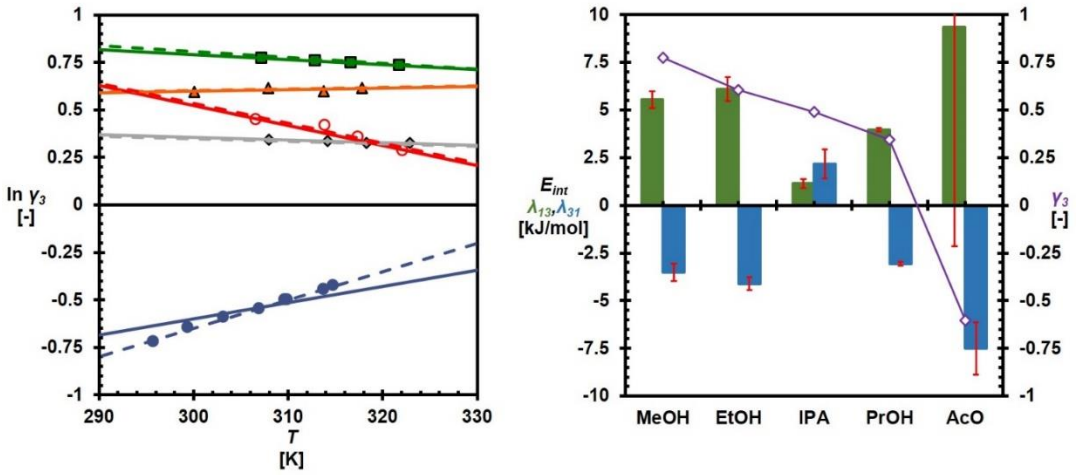

Figure 5-6: Experimentally determined activity coefficient for LOV in MeOH (■), EtOH (▲), PrOH (♦), IPA (○) and AcO (●), alongside the respective Wilson parameters obtained from fitting equation 81 to the experimental data. The solid lines cutting through each system (LHS) describe the predicted activity coefficient using the fitted Wilson parameters in Table 5-2 and the ideal solubility from equation 81. The dashed line cutting through the experimental data (LHS) indicates the calculated activity coefficient from equation 80. The solid bars on the right represent the temperature-independent Wilson parameters obtained from the regression of the experimental data with Equation 81. Also the γ_3 at 303K (—) is given at the right.

The σ gives a better impression on the precision of the dataset. The σ can be calculated from the equation:

$$\sigma\,(\%) = 100 * \sqrt{\frac{1}{(N-1)}\sum_{i=1}^{N}\left(\frac{x_3 - x_3^{pred}}{x_3}\right)^2} \qquad 84$$

With *N* representing the number of experimental mol fraction solubilities x_3, with the difference between itself and the Wilson predicted mol fraction x_3^{pred} used to determine the variation of results. The values of λ_{13} and λ_{31} for each solvent is presented in Figure 5-6(right) and the σ for each system is presented in Table 5-2. There is no clear trend in λ_{13} and λ_{31} between the individual systems. When going from LOV-MeOH to LOV-EtOH, λ_{13} and λ_{31} increase and decrease

respectively, alongside a reduction in activity coefficient towards ideality. This indicates an increased interaction between the molecules. For LOV-IPA, the interaction coefficients move closer to zero so aligning with a reduced γ_3 towards ideality. This is different from previous systems where the parameters showed an increase, which is consistent with increasing interactions between the molecules. This is the only system with both interaction parameters being positive. The low σ for LOV-PrOH as well as their error bars not overlapping with the previous systems, allow for high confidence in their values. The larger temperature dependence of the system could be the cause of these interaction differences from previous systems. For LOV-PrOH, the interaction parameters show a reduction when compared to the previous primary alcohols, moving towards ideality. This movement to ideality is also shown from γ_3. LOV-AcO shows the largest interaction parameters than any other system. The highly negative value of λ_{31} aligns with a highly non-ideal γ_3. This is consistent with strong interactions between the molecules. The σ for this system is much larger than previous systems, with λ_{13} having a very large error bar than the actual value so it is hard to infer interaction values from this parameter. It is likely the highly negative activity coefficient is affecting the effectiveness of the fitting.

Table 5-2: The interaction energy constants λ_{13} and λ_{31} obtained from the binary Wilson model for each solvent-solute system, alongside their respective %σ.

Single Solvent	λ_{13} [kJ/mol]	λ_{31} [kJ/mol]	σ [%]
Methanol	5.5 ± 0.4	-3.5 ± 0.5	0.5
Ethanol	6.1 ± 0.6	-4.1 ± 0.3	0.6
Propanol	4.0 ± 0.1	-3.1 ± 0.1	0.01
IPA	1.1 ± 0.2	2.2 ± 0.8	0.05
Acetone	9.3 ± 11	-7.5 ± 1.4	4.3

As expected from equation 79, in most cases the activity coefficient decreases with increasing temperature as at the melting temperature T_m, we have a pure single component system and the activity coefficient is $\gamma_3 = 1$ ($\ln \gamma_3 = 0$). Only for

measurement series with activity coefficients close to ideality the temperature dependence of the activity coefficient is less clear.

5.4.4 Lovastatin-Solvent-Water Wilson Modelling

For multicomponent systems, Wilson proposed the following equation:

$$\ln \gamma_k = 1 - \ln\left(\sum_{j=1}^{N} x_j \Lambda_{kj}\right) - \sum_{i=1}^{N}\left(\frac{x_i \Lambda_{ik}}{\sum_{j=1}^{N} x_j \Lambda_{ij}}\right) \qquad 85$$

With the subscripts i, j and k representing the notation for the individual components and Λ_{ik}, Λ_{ij} and Λ_{kj} representing the unit less interaction parameters between the component molecules, with these terms further broken down into the forms shown in equation 83 and 84 in order to obtain the interaction parameters in J/mol between the component molecules. To apply equation 86, the interaction parameters between all components must be known.

By expanding on the previous interpretation of local composition of similar and dissimilar molecules around a central molecule, the addition and increasing presence of another component is interpreted in Figure 5-7.

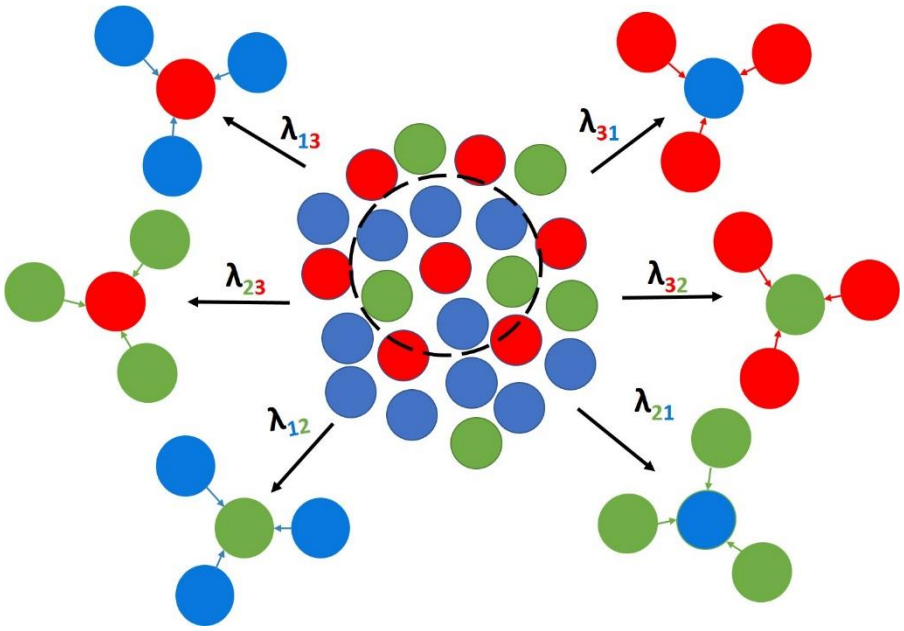

Figure 5-7: Visual representation of the concept of multicomponent local composition theory, with LOV (●) molecules surrounded by both solvent (●) and water (●) molecules. The interaction parameters between each molecule are represented by their associated caption, along with how these molecules

are theorized to interact with one another. The interaction energy between similar molecule λ_{11}/ λ_{22}/ λ_{33} = 0. The arrow direction indicates the direction of the molecular interactions.

For the LOV-solvent parameters, λ_{13} and λ_{31}, the previously obtained values are used from the binary Wilson regression with experimental data in Table 5-2. The solvent-antisolvent interaction parameters, λ_{12} and λ_{21}, are available through the Dortmund Data Bank in which the Wilson equation has been applied to it as a binary system for distillation column design. Due to the extremely low solubility of LOV in pure water, the interaction parameters, λ_{23} and λ_{32}, between the two are not able to be distinguished using the methodology applied previously. Regression analysis utilizing equation 86 was attempted in order to obtain the individual interaction parameters as a function of the antisolvent content. To do this the previously obtained interaction parameters where used as constants for the regression, with the two remaining unknowns being the LOV-water interactions.

Using the binary interaction parameters, the multicomponent Wilson equation did not give a good fit and so could not capture the interplay between all three components present with the system. Other regression methods like trying to extrapolate other parameters such as the solvent-antisolvent parameters although this only exacerbated the error. Therefore, another method had to be tried to better understand how the systems are interacting with increasing antisolvent fractions. The inability of the model to provide quantitative data does provide quantitate information that the interaction values change, and so no set value can properly be applied without extremely large errors as observed.

5.4.5 Solvent Mixture as a Continuum

To get a better description of the interplay between the three molecules present within each system, a solvent-antisolvent continuum-based approach was applied to observe the change in interaction parameters between components at subsequent antisolvent fraction. Subsequently looking to identify if the interaction values change as the antisolvent fraction changes. By applying equation 82 to the experimentally obtained γ_3 for each system, the interaction

parameters between LOV and the surrounding molecules are determined at increasing antisolvent fractions. This is shown in Figure 5-8, alongside the measured and predicted activity coefficient. For each system, the molecular volume of each mixture was calculated using Equation 87:

$$V_m = \frac{x_1 MW_1 + x_2 MW_2}{\rho} \qquad 86$$

With x and MW representing the mole fraction and the molecular weight of the solvent. In all cases, the subscript 2 represented water. The density ρ in g/m^3 for each system at increasing solvent-water ratios were provided by literature[109–112]. Using the measured densities from these sources, a line of best fit used to obtain an equation to describe the density and so providing accurate values for each solvent-water fraction. These graphs and respective lines of best fit are provided in the SI.

As the antisolvent fraction increases, both λ_{13} and λ_{31} show uniquely different changes for all systems as presented in Figure 5-8 (right). For presenting the interaction parameters in Figure 5-8 (right), a mol fraction basis was used instead of the mass fraction used. As local composition theory and the resulting Wilson equation refer to the mol fraction of individual components in the system, using mol fraction to represent the data gives a better overall perspective of the composition of antisolvent in each system. The solute free mol fraction $x_{AS,mol}$ of the solvent system is determined from the following:

$$x_{AS,mol} = \frac{x_w}{x_s + x_w} \qquad 87$$

Where x_w and x_s are the mol fractions of water and solvent respectively present in the system.

For the LOV-MeOH-water system, the Wilson equation produced a good fit at each antisolvent fraction. At x_{AS} = 0, λ_{13} and λ_{31} show a positive and negative value respectively and as the antisolvent fraction increases, λ_{13} shows a slightly decreasing trend whereas λ_{31} shows a larger increase. For λ_{13}, the errors for all but one antisolvent fraction is smaller than the presented marker. For LOV in MeOH-water, the small error bars for the majority of measured interaction

parameters produced a good fit for each Wilson prediction. The large error bar at the highest antisolvent fraction for λ_{31} also presents a large discrepancy between the experimental and predicted γ, with the predicted values cutting through the middle of the experimental values and producing a much steeper negative gradient to that of the experimental values. In contrast to this, the large error presented for x_{AS} = 0.05 in both interaction parameters does not seem to influence the prediction comparison so signifying further the combinational effect of these interaction parameters.

For LOV in EtOH-water, from x_{AS} = 0 the interaction energy parameters again show a combinational effect between one another, with either a positive or negative direction for one producing the opposite direction for the other. Like for MeOH-water, λ_{13} shows a somewhat linear dependence at increasing antisolvent fractions with a slight negative gradient but not to the same degree as previously seen for MeOH-water. Whereas λ_{31} instead shows a polynomial relationship at increasing antisolvent fractions, with λ_{31} at the lower antisolvent fractions staying relatively constant around -4 kJ/mol before increasing significantly towards more positive values at higher antisolvent fractions.

LOV in both PrOH-water and IPA-water systems show similar trends in their interaction parameters when comparing to EtOH-water, with λ_{13} and λ_{31} again presenting a linear and parabolic relationship respectively for increasing antisolvent fractions. From their antisolvent free interaction values, λ_{31} decreases becoming increasingly negative as the x_{AS} increases with it reaching maxima before increasing significantly at the higher antisolvent fractions measured. LOV-IPA-water observes a much larger decrease in λ_{31} with its λ_{13} also showing a more significant gradient than that for LOV-PrOH-water. The predicted activity coefficients also show good agreement with the experimental γ_3 as in Figure 5-8 (Left).

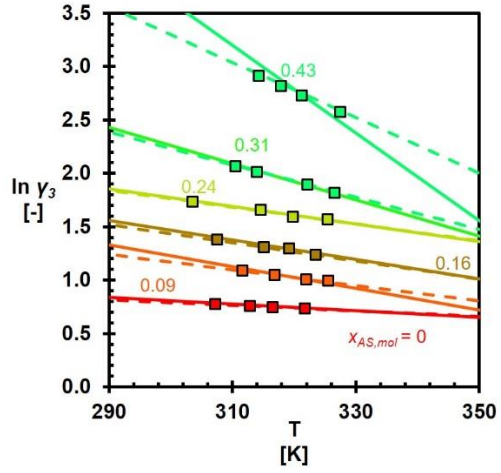
ln γ_3 [-]
T [K]
0.43
0.31
0.24
0.16
0.09
$x_{AS,mol}$ = 0

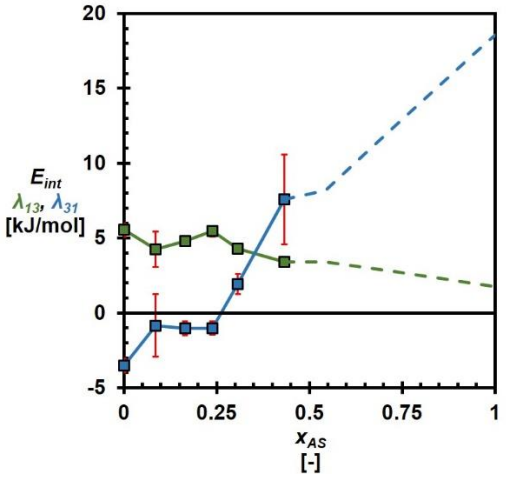
E_{int} λ_{13}, λ_{31} [kJ/mol]
x_{AS} [-]

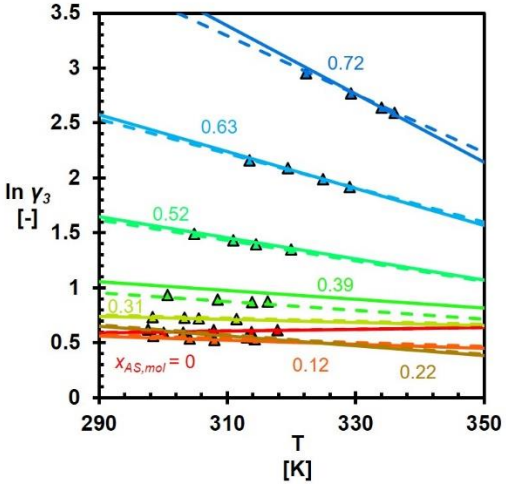
ln γ_3 [-]
T [K]
0.72
0.63
0.52
0.39
0.31
$x_{AS,mol}$ = 0
0.12
0.22

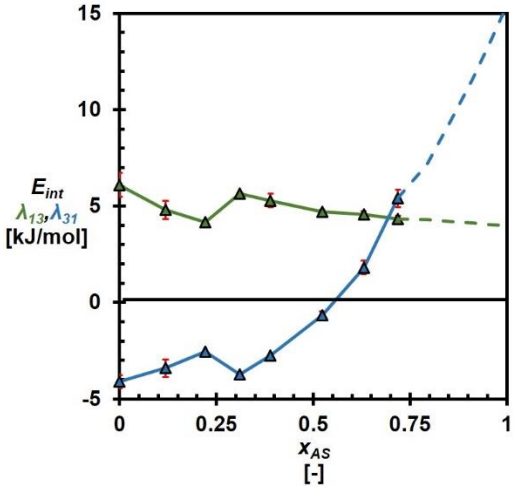
E_{int} λ_{13},λ_{31} [kJ/mol]
x_{AS} [-]

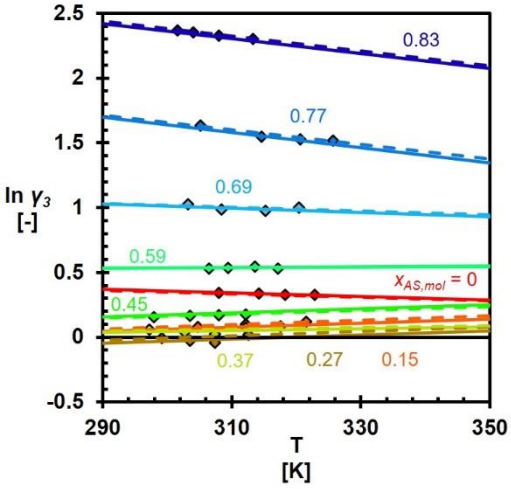
ln γ_3 [-]
T [K]
0.83
0.77
0.69
0.59
$x_{AS,mol}$ = 0
0.45
0.37
0.27
0.15

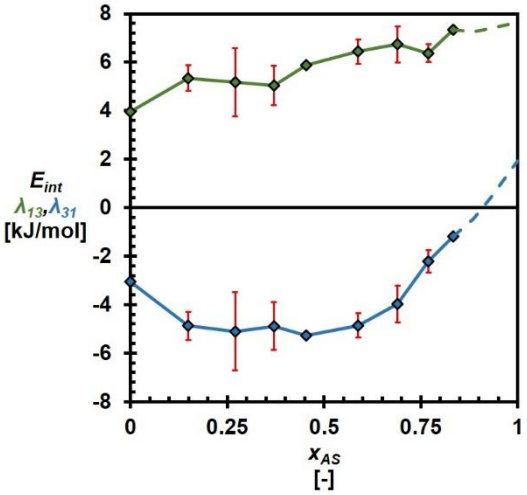
E_{int} λ_{13},λ_{31} [kJ/mol]
x_{AS} [-]

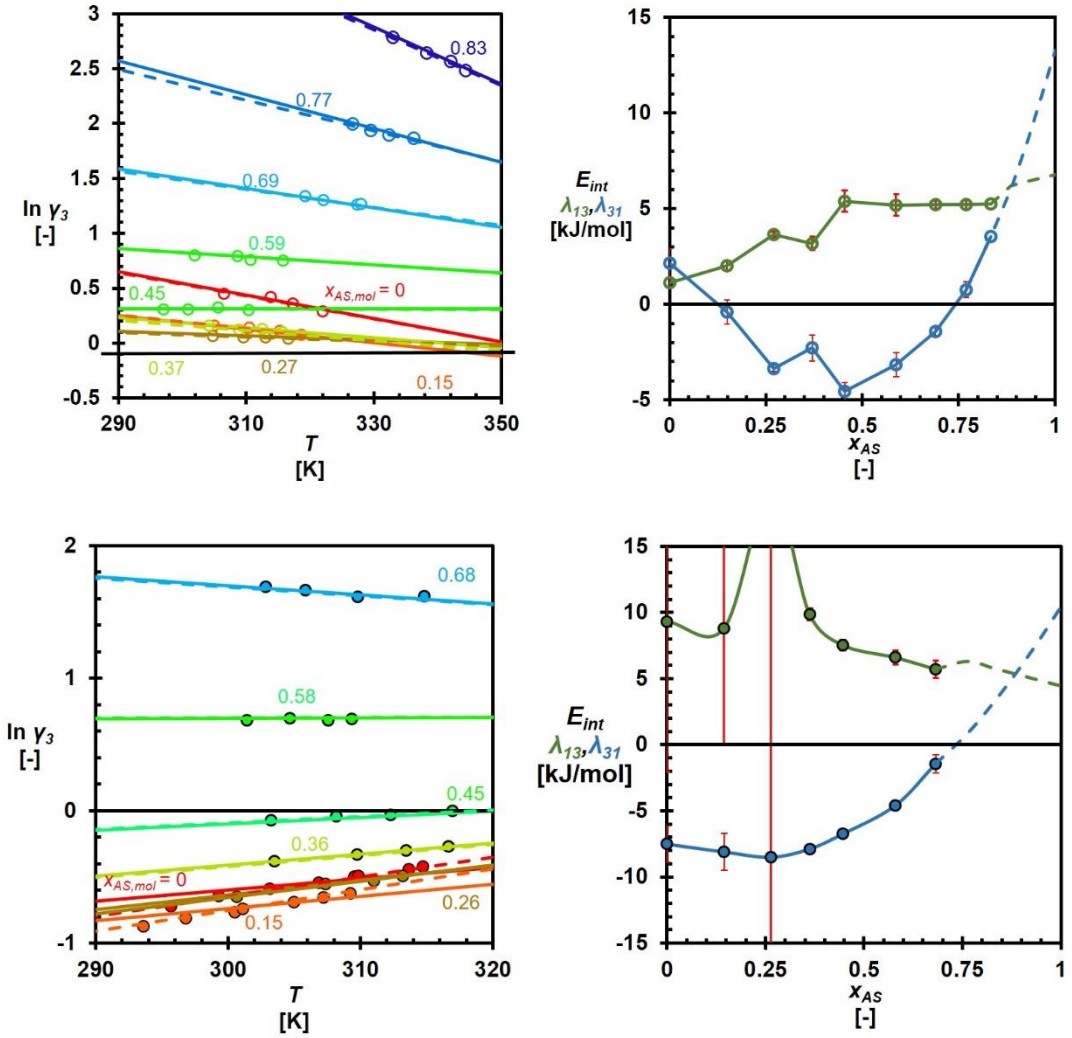

Figure 5-8: The experimentally determined activity coefficients γ_3 and their respective Wilson binary interaction parameters (λ_{13} and λ_{31}) for LOV in MeOH-water (■), EtOH-water (▲), PrOH-water (♦), IPA-water (○) and AcO-water (●), with the labels beside each dataset the specific antisolvent mass fraction. The solid lines cutting through each set of experimental γ_3 (left) is the predicted γ_3 from the binary Wilson model to correlate against the experimental values. The dashed lines on the LHS represents the activity coefficient determined from the line of best fit from the experimental interaction values on the RHS. The solid lines between each experimentally determined interaction parameter (right) shows direction between each data point, with the dashed lines representing an extension of these lines from a line of best fit. The red lines represent the 95% confidence intervals determined

from the Wilson regression. The antisolvent mass fraction for each system is provided in the left figure, with the mole fraction of the antisolvent present used on the right figures.

LOV-AcO-water shows similarities with the other systems as well as significant differences. Similar to MeOH and EtOH systems, the λ_{13} shows a linear change at increasing antisolvent fractions. λ_{31} again shows a parabolic shape with it becoming increasingly negative up to a maximum at x_{AS} = 0.1, before increasing significantly at the higher fractions. Although excellent agreement is shown between the predicted and experimental activities for the majority of antisolvent fractions measured for LOV-AcO-water, the predicted Wilson γ_3 of the lower fractions show relatively large differences to the experimental. The large error bars for these lower fractions, especially for x_{AS} = 0.1, show the inability of the Wilson model to accurately predict the interaction parameters at these low factions, with the highly negative activities at these lower fractions being the issue. This could be due to the inability of the Wilson to predict highly negative activity coefficient systems. At the higher fractions and more positive γ_3 the error bars are much smaller and so show a much better prediction in comparison to the experimental values.

5.4.6 Wilson Interaction Landscape

From Figure 5-9, the Wilson interaction landscape shows that for all combinations of interaction parameters within the specific lines for each system, a representative σ would be obtained against the experimental results. This allows a better interpretation of the interaction parmeters and how they can change to provide the same activity coefficient for a certain system. For LOV-MeOH-water, the experimental interaction parameters are within the 5% σ for each antisolvent fraction. At x_{as} = 0, the experimental value is within the centre of the interaction well, with this also being the case for all other experimental values in relation to their predicted landscape except x_{AS} = 0.3. At increasing antisolvent fraction, the regions in which 5% σ is observed increases towards larger λ_{31} values. These landscapes show how the error associated with the experimental

values are actually representative to the actual value. As the antisolvent fraction increases, the width of the λ31 between the 5% σ limits increasing producing a larger region where the experimental lambda value would be relevant. For λ_{13}, the region within the 5% σ does not significantly change due to the direction of the Wilson region at changing fractions.

For LOV-EtOH-water, the trend of increasing 5% σ boundary between antisolvent fractions is similar to LOV-MeOH-water, with the experimental interaction values within these boundaries. Unlike previously, the regions in which the 5% σ is maintained reduces towards more negative λ_{31} regions at an x_{AS} = 0.05. From this point at increasing x_{AS} it follows the same trend to the LOV-MeOH-water system. The experimental lambda values once again lie within the predicted regions showing the experimental values are significant. The overlap observed between regions is again shown at the lower fractions although is lost at increasing fractions.

LOV in the PrOH-water, IPA-water and AcO-water systems observe the same shift as that of the EtOH-water regions to more significantly negative λ_{31} values at the lower antisolvent fractions, with it then increasing towards positive λ_{31} values as the antisolvent fractions increase. Regions of overlap exist between systems close to one another in terms of λ_{31} although at the higher fractions, overlap with the lower fractions is not observed showing significance of the difference. Regions where there are shifts to lower λ_{31} regions show no overlap with x_{AS} = 0 so showing observable significance in their values. The regions of 5% σ once again increase significantly at the higher fractions, with the steepness in the 5% σ well reducing as observed by the thinner individual lines like for x_{AS} = 0.5 for IPA-water.

From the landscapes, we see that the λ_{31} interaction parameter is most affected by the change in antisolvent fraction, with the λ_{13} parameter not being as significantly influenced.

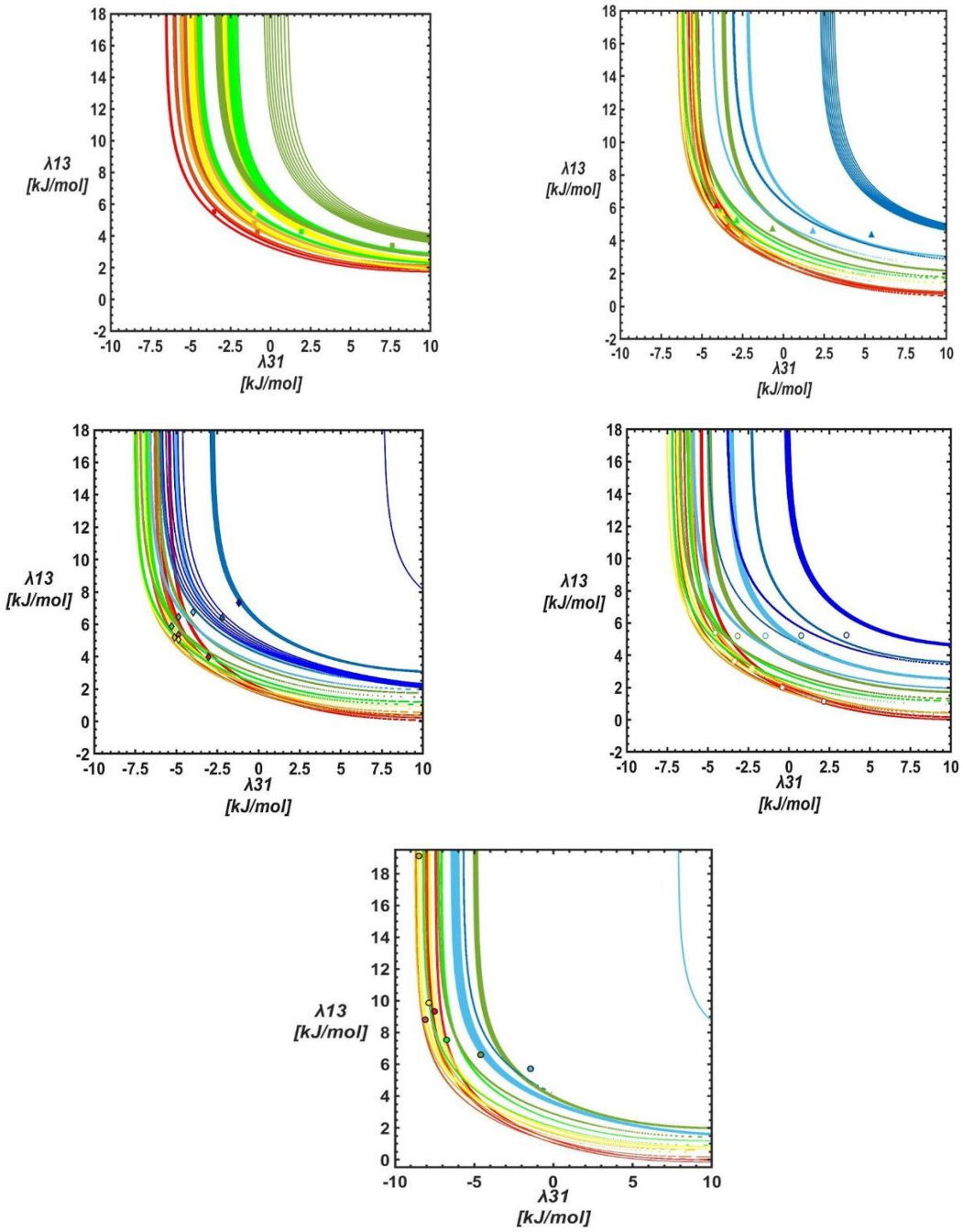

Figure 5-9: The predicted Wilson interaction landscape of LOV in MeOH-water (■), EtOH-water (▲), PrOH-water (♦), IPA-water (○) and AcO-water (●) from -10 kJ/mol to 10 kJ/mol for both λ_{13} and λ_{31}. Each marker represents the fitted interaction parameter for all systems at each antisolvent fraction. The space between each line for all systems represent the interaction parameters producing an $\sigma < 5\%$ between the predicted and experimental mol fractions. The colours designate the antisolvent mass fraction: 0 (—), 0.05 (—), 0.1 (—), 0.15 (—), 0.2 (—), 0.3 (—), 0.4 (—), 0.5 (—) and 0.6 (—).

5.5 Discussion

The multicomponent Wilson equation (equation 85) is not able to accurately fit the experimental data and so could not capture the molecular interplay. From literature, the incidence of a maxima present in the activity coefficients of mixed solvent systems is common for both VLE[69] and SLE[113]. The inability of the multicomponent Wilson to predict VLE maxima is known[16]. To our knowledge this is the first instance to show its applicability on solid-liquid-liquid systems. Wilson presented his multicomponent equation essentially on empirical grounds, so its ability to predict systems out-with the similarities to his empirical data is limited as has been presented here[114]. From our observations, the assumption that there are constant binary interaction parameters for ternary system is not correct. The increasing presence of the third component influences the interaction parameter between the other two components. Therefore, for antisolvent systems, the interaction between the solute and solvent molecules are changed when the antisolvent is added. This influence can be seen from the maxima that arises from small antisolvent presences in both the measured systems and others in literature. As the antisolvent presence increases, the local composition around the solute molecules, causing greater attraction between the solute-solvent molecules. As the antisolvent presence increases further, the local composition around the solute molecule changes, with the antisolvent becoming more dominant causing greater repulsion between the solute molecules and the surrounding solvent molecules.

The interaction landscape for the binary Wilson parameters (Figure 5-9) shows that the adjustable parameters from the Wilson equation are not singular values but a combination of a range of interaction values. Instead, they provide the best fit over a large region of values of interaction parameter combinations. Between LOV-solvent-water systems, the landscape changes moving to lower λ_{31} values initially for systems where a decrease in γ_3 is also observed, with λ_{13} not changing to as much of a degree. As the antisolvent fraction increases and the activity coefficient changes moving positively away from ideality, the <5% σ region of the interaction parameters broadens with its biggest coming at the highest

antisolvent fraction for each system. If a lower limit of σ was used, the size of the wells would decrease towards the interaction value. This larger well explains the larger σ observed by the systems at the highest fraction when compared to the preceding fractions. As λ_{31} is the parameter being impacted due the increasing presence of antisolvent this parameter would be the main one to infer the change in interactions of the molecules within the system. We therefore chose to consider the solvent-antisolvent mixture as a continuum so that the ternary system can be described with only two interaction parameters instead of 6. The region of σ < 5% for these two interaction parameters is elongated which causes a wide range of interaction parameter combinations to reasonably accurately describe the experimental data.

From Raoult's law, γ < 1 are distinctive of negative deviations from ideality, highlighting in a binary system the dominance of interaction between solute and solvent molecules over solute-solute or solvent-solvent. From the observations it can be thought that the larger the interaction between dissimilar molecules, the more negative λ_{31}. It is more negative interaction parameter that shows a greater solubility, as with LOV-AcO when comparing to the other systems. As the antisolvent fraction increases, interactions with dissimilar molecules increases. The landscape of these increasing fractions moves slightly to the left for all systems except MeOH. This shift shows increased interaction between molecules, corresponding to the slightly higher solubility of the system at this fraction compared to the antisolvent-free mixture. As the fractions increase, the region of σ < 5% shifts to the right at increasing x_{AS} fractions showing reduced interactions of dissimilar molecules and so reduced solubility. LOV-IPA is the only system to show a both interaction parameters to be positive initially meaning the system is experiencing more like-like interactions between molecules. Unlike the other alcohols, IPA cannot interact with itself so can only interact LOV. The introduction of the water at low fractions produces a significantly more dissimilar interactions between molecules (IPA-water) to occur allowing a significant increase in solubility to occur as observed. Then like the MeOH system, further increase of water increases the water-water interactions, increasing like-like interactions in a system and so reducing the solubility of LOV.

In terms of why this is occurring, water molecules are able to form hydrogen bonds with itself as well as other solvents, with solvents also able to form H-bonds with itself from the oxygen[115]. How well a molecule can be dissolved in a solvent is down to how easy it is for the solute to break the bonds between solvents and incorporate itself into this bonding. When water is added into a solution, the small water content is able to break the solvent H-bonding between the solvent molecules and instead form a new H-bonding network[116] with all components which causes synergistic effects. This synergistic effect was observed from the interaction parameters, with λ_{31} become increasingly negative and so causing an increase in solubility. As the water content increases, water would rather bond with itself creating a continuous 3D structure than with other solvents. So when non-polar regions of LOV comes in to contact with the water molecules, it is unable integrate itself and so reducing the solubility at increasing water contents. MeOH-water is a strange case as it is able to form H-bond with itself and water although no maxima is observed. It has been found that below a volume fraction > 0.4 for MeOH, there is no shift in hydrogen bonding at increasing water content, although the addition of water does destroy the binding of MeOH to one another[117]. The lack of interaction between the mixed solvents at increasing amounts could mean that the increasing water reduces the LOV ability to dissolve so reducing the solubility. The increasingly positive value of λ_{31} relates to a reducing interaction between dissimilar molecules according to Raoult's law. This lack of interaction is consistent with decreased solubility of the solute molecule.

From these interactions, it could be possible to highlight preferred antisolvent types where solute-solvent interactions are maximized due to the presence of a third component. The third component being one which can interact with both the solute and solvent. Solvent systems exhibiting increasingly negative λ_{31} values can be prioritized. In doing so optimizing the selection of solvent-antisolvent systems.

From this study the design of antisolvent crystallization processes can be scrutinized. The use of solvents which are likely to provide a synergistic effect

with the current solute-solvent system are prioritized, with it allowing a greater amount of solute to be initially dissolved. Also, the dramatic change that would be observed with solvents like water impacting the solute-solvent interactions significantly should also be prioritized for antisolvent systems over other common antisolvent like heptane. As heptane will not interact with either itself or the solute molecules, its role as an antisolvent would only be to reduce the solubility for mixed solvent cooling crystallization. Whereas water or other solvents which will interact against solute are more optimal for antisolvent addition crystallization.

5.6 Conclusion

The solubility and respective activity coefficient of LOV in the single solvents MeOH, EtOH, PrOH, IPA and AcO as well as varying solvent-water fractions were determined. The obtained activity coefficients for the single systems were regressed using the binary Wilson equation, obtaining the interaction parameters λ_{13} and λ_{31} between the solvent and solute. From these interaction parameters at increasing fractions, the LOV-water interaction parameters were able to be obtained due to the trends observed. The multicomponent Wilson model was not able to adequately model the synergistic behavior of the systems. By considering the solvent-antisolvent mixture as a continuum, the number of parameters required to describe the system was reduced to only two. From the behavior of these binary interaction parameters as a function of antisolvent fraction, the λ_{31} parameter shows the biggest influence from the increasing antisolvent content. This parameter seems to show how solubility is being affected by molecular interactions.

5.7 Acknowledgements

The authors would like to acknowledge financial support from the Strathclyde Institute of Physical Biomedical and Sciences and the Doctoral Training Centre in Continuous Manufacturing and Crystallization (CMAC).

5.8 References

1. Wouters OJ, McKee M, Luyten J. Estimated Research and Development Investment Needed to Bring a New Medicine to Market, 2009-2018. *JAMA*

- *J Am Med Assoc*. 2020;323(9):844-853. doi:10.1001/jama.2020.1166

2. Savjani KT, Gajjar AK, Savjani JK. Drug Solubility: Importance and Enhancement Techniques. *ISRN Pharm*. 2012;2012(100 mL):1-10. doi:10.5402/2012/195727

3. Committee for Human Medicinal Products. ICH guideline Q3C (R5) on impurities: Guideline for Residual Solvents. *Int Conf Harmon Tech Requir Regist Pharm Hum Use*. 2015;44(October 2002):24.

4. Lewis A, Seckler M, Kramer H, Rosmalen G. Melt Crystallisation. In: *Industrial Crystallization: Fundamentals and Applications*. ; 2015:261-281.

5. Lewis A, Kramer H, Seckler M. Thermodynamics, Crystallzation Methods and Supersaturation. In: *Industrial Crystallization: Fundamentals and Applications*. ; 2015:1-25.

6. Spyriouni T, Krokidis X, Economou IG. Thermodynamics of pharmaceuticals: Prediction of solubility in pure and mixed solvents with PC-SAFT. *Fluid Phase Equilib*. 2011;302(1-2):331-337. doi:10.1016/j.fluid.2010.08.029

7. Loschen C, Klamt A. Solubility prediction, solvate and cocrystal screening as tools for rational crystal engineering. *J Pharm Pharmacol*. 2015;67(6):803-811. doi:10.1111/jphp.12376

8. Tung HH, Tabora J, Variankaval N, Bakken D, Chen CC. Prediction of pharmaceutical solubility via NRTL-SAC and COSMO-SAC. *J Pharm Sci*. 2008;97(5):1813-1820. doi:10.1002/jps.21032

9. Myerson AS, Erdemir D, Lee AY. Thermodynamic Concepts and Ideal Solubility. In: *Handbook of Industrial Crystallization*. ; 2019:1-31.

10. Zumdahl S. The Equilibrium Constant. In: *Chemistry*. 5th ed. Houghton Mifflin; 1999:578-620.

11. Xu R, Huang C. Solubility Modeling and Solution Thermodynamics of 4-Amino-2,6-Dimethoxypyrimidine in Cosolvent Mixtures of Methanol, Ethanol, Isopropanol, and N, N-Dimethylformamide + Water. *J Chem Eng Data*. 2018;63(11):4234-4240. doi:10.1021/acs.jced.8b00719

12. Zhao H, Xu H, Yang Z, Li R. Solubility of 3,4-dichloronitrobenzene in methanol, ethanol, and liquid mixtures (methanol + water, ethanol + water): Experimental measurement and thermodynamic modeling. *J Chem Eng Data*. 2013;58(11):3061-3068. doi:10.1021/je400507u

13. Jia L, Yin Q. Insights into the mechanism of concomitant nucleation of form II and ethanol solvate of spironolactone in cooling crystallization †. 2018:9697-9706. doi:10.1039/c7ra13094e

14. Yang Y, Tang W, Li X, et al. Solubility of Benzoin in Six Monosolvents and in Some Binary Solvent Mixtures at Various Temperatures. *J Chem Eng Data*. 2017;62(10):3071-3083. doi:10.1021/acs.jced.7b00238

15. Gmehling J, Kleiber M. *Vapor-Liquid Equilibrium and Physical Properties for Distillation*.; 2014. doi:10.1016/B978-0-12-386547-2.00002-8

16. Seader JD, Henley E, Roper DK. *Seperation Process Principles-Chemical and Biochemical Operations*. 3rd ed. John Wiley & Sons, Inc.; 2011.

17. Smith JM, Ness HC Van, Abbot MM, Swihart MT. *Introduction to Chemical Engineering Thermodynamics Eight Edition*.; 2018.

18. Abbot M, Berthold J, de Loos T. *Models for Thermodynamic and Phase Equilibria Calculations*. 1st ed. (Sandler S, ed.).; 1994.

19. Vagenas GK, Marinos-Kouris D. Use of the Wilson equation for the prediction of the sorptional equilibrium of sugar-based foodstuffs. *Fluid Phase Equilib*. 1992;78(C):191-207. doi:10.1016/0378-3812(92)87034-K

20. Dojcanský J, Bafrncová S, Surový J. Application of the Wilson Equation with Binary Parameters to the Prediction of the Isothermal Vapour-Liquid Equilibrium Data of Ternary and Quaternary Systems in the Assessment of the Polar Solvent in Extractive Distillation. 2001;55(2):71-74.

21. Sadeghi R. Extension of the Wilson model to multicomponent polymer solutions: Applications to polymer-polymer aqueous two-phase systems. *J Chem Thermodyn*. 2005;37(1):55-60. doi:10.1016/j.jct.2004.08.007

22. von Raumer M, Hilfiker R. A Short Introduction to Polymorphism and Solid-State Development. In: *Polymorphism in the Pharmaceutuical Industr: Solid*

Form and Drug Development. 1st ed. ; 2019:1-23.

23. Vrani E. Amorphous Pharmaeutical Solids. *Bosn J Basic Med Sci*. 2004;4(3):35-39.

24. Aitipamula S, Banerjee R, Bansal AK, et al. Polymorphs, salts, and cocrystals: What's in a name? *Cryst Growth Des*. 2012;12(5):2147-2152. doi:10.1021/cg3002948

25. Lewis A, Seckler M, Kramer H, Rosmalen G. Polymorphism. In: *Industrial Crystallization: Fundamentals and Applications*. ; 2015:303-319.

26. Cruz-Cabeza AJ, Reutzel-Edens SM, Bernstein J. Facts and fictions about polymorphism. *Chem Soc Rev*. 2015;44(23):8619-8635. doi:10.1039/c5cs00227c

27. Lee EH. A practical guide to pharmaceutical polymorph screening & selection. *Asian J Pharm Sci*. 2014;9(4):163-175. doi:10.1016/j.ajps.2014.05.002

28. Cesur S, Gokbel S. Crystallization of mefenamic acid and polymorphs. *Cryst Res Technol*. 2008;43(7):720-728. doi:10.1002/crat.200711119

29. Ferrari ES, Davey RJ, Cross WI, Gillon AL, Towler CS. Crystallization in polymorphic systems: The solution-mediated transformation of β to α glycine. *Cryst Growth Des*. 2003;3(1):53-60. doi:10.1021/cg025561b

30. Padrela L, Zeglinski J, Ryan KM. Insight into the Role of Additives in Controlling Polymorphic Outcome: A CO2-Antisolvent Crystallization Process of Carbamazepine. *Cryst Growth Des*. 2017;17(9):4544-4553. doi:10.1021/acs.cgd.7b00163

31. Kulkarni SA, McGarrity ES, Meekes H, Ter Horst JH. Isonicotinamide self-association: The link between solvent and polymorph nucleation. *Chem Commun*. 2012;48(41):4983-4985. doi:10.1039/c2cc18025a

32. Joel Bernstein, Roger J. Davey, Jan-Olav Henck. Concomitant Polymorphs. *Angew Chemie Int Ed*. 1999;38(23):2440-3461. doi:10.1002/(SICI)1521-3773(19991203)38:23<3440::AID-ANIE3440>3.0.CO;2

33. Teychené S, Biscans B. Nucleation kinetics of polymorphs: Induction period

and interfacial energy measurements. *Cryst Growth Des*. 2008;8(4):1133-1139. doi:10.1021/cg0609320

34. Jiang S, Horst JH, Jansens PJ. Concomitant Polymorphism of o-Aminobenzoic Acid in Antisolvent Crystallization. *Cryst Growth Des*. 2008;8(1):37-43.

35. ter Horst JH, Kramer HJM, Jansens PJ. A New Molecular Modeling Approach To Predict Concomitant Nucleation of Polymorphs. *Cryst Growth Des*. 2002;2(5):351-356.

36. Black S, Muller F, Fielding M. A Practical Approach for Using Solubility to Design Cooling Crystallisations. *Org Process Res Dev*. 2009;13:1315-1321.

37. Lewis A, Seckler M, Kramer H. Batch Crystallisation. In: *Industrial Crystallization*. ; 2015:178-191.

38. Zhang D, Liu L, Xu S, Du S, Dong W, Gong J. Optimization of cooling strategy and seeding by FBRM analysis of batch crystallization. *J Cryst Growth*. 2018;486:1-9. doi:10.1016/j.jcrysgro.2017.12.046

39. Zhang F, Liu T, Chen W, Ma CY, Wang XZ. Seed Recipe Design for Batch Cooling Crystallization with Application to l -Glutamic Acid. *Ind Eng Chem Res*. 2019;58(8):3175-3187. doi:10.1021/acs.iecr.8b06006

40. Pinho SP, Macedo EA. Solubility of NaCl, NaBr, and KCl in water, methanol, ethanol, and their mixed solvents. *J Chem Eng Data*. 2005;50(1):29-32. doi:10.1021/je049922y

41. Svärd M, Nordström FL, Jasnobulka T, Rasmuson ÅC. Thermodynamics and nucleation kinetics of m-aminobenzoic acid polymorphs. *Cryst Growth Des*. 2010;10(1):195-204. doi:10.1021/cg900850u

42. Mullin J. Ideal and Non-ideal Solutions. In: *Nucleation*. 4th ed. ; 2001:98-100.

43. Bhamidi V, Kenis PJA, Zukoski CF. Probability of Nucleation in a Metastable Zone : Cooling Crystallization and Polythermal Method. doi:10.1021/acs.cgd.7b00875

44. Lenka M, Sarkar D. Determination of metastable zone width, induction

period and primary nucleation kinetics for cooling crystallization of L-asparaginenohydrate. *J Cryst Growth*. 2014;408:85-90. doi:10.1016/j.jcrysgro.2014.09.027

45. Karpinski P, Baldyga J. Precipitation Processes. In: *Handbook of Industrial Crystallization*. 3rd ed. ; 2019:217-265.

46. Macedo EA. Solubility of amino acids, sugars, and proteins. *Pure Appl Chem*. 2005;77(3):559-568. doi:10.1351/pac200577030559

47. Giulietti M, Bernardo A. Crystallization by Antisolvent Addition and Cooling. *Cryst - Sci Technol*. 2012. doi:10.5772/50328

48. Chang J, Wang J, Diao Y, Wang W, Chen Q, Yu Z. Study on the solubility characteristic of the antisolvent crystallization of RDX. *J Phase Equilibria Diffus*. 2011;32(3):206-211. doi:10.1007/s11669-011-9872-3

49. Hansen TB, Qu H. Formation of Piroxicam Polymorphism in Solution Crystallization : E ff ect and Interplay of Operation Parameters. 2015. doi:10.1021/acs.cgd.5b01016

50. Hilfiker R, Blatter F, Szelagiewicz M. Screening for Polymorphs,Hydrates and Solvates. In: Hilfiker R, von Raumer M, eds. *Polymorphism in the Pharmaceutuical Industr: Solid Form and Drug Development*. 1st ed. ; 2019:241-256.

51. Lee S, Lee CH, Kim WS. Anti-solvent crystallization of L-threonine in Taylor crystallizers and MSMPR crystallizer: Effect of fluid dynamic motions on crystal size, shape, and recovery. *J Cryst Growth*. 2017;469:119-127. doi:10.1016/j.jcrysgro.2016.08.021

52. Ferguson S, Morris G, Hao H, Barrett M, Glennon B. Characterization of the anti-solvent batch, plug flow and MSMPR crystallization of benzoic acid. *Chem Eng Sci*. 2013;104:44-54. doi:10.1016/j.ces.2013.09.006

53. Mostafa Nowee S, Abbas A, Romagnoli JA. Antisolvent crystallization: Model identification, experimental validation and dynamic simulation. *Chem Eng Sci*. 2008;63(22):5457-5467. doi:10.1016/j.ces.2008.08.003

54. Vellema J, Hunfeld NGM, Van Den Akker HEA, Ter Horst JH. Avoiding

crystallization of lorazepam during infusion. *Eur J Pharm Sci*. 2011;44(5):621-626. doi:10.1016/j.ejps.2011.10.010

55. Nagy ZK, Fujiwara M, Braatz RD. Modelling and control of combined cooling and antisolvent crystallization processes. *J Process Control*. 2008;18(9):856-864. doi:10.1016/j.jprocont.2008.06.002

56. Braatz RD. Advanced control of crystallization processes. *Annu Rev Control*. 2002;26 I:87-99. doi:10.1016/S1367-5788(02)80016-5

57. Barik K, Prusti P, Mohapatra SS. Single- and multi-objective optimisation for a combined cooling and antisolvent semi-batch crystallisation process with an ACADO toolkit. *Indian Chem Eng*. 2020;62(3):287-300. doi:10.1080/00194506.2019.1677511

58. Lindenberg C, Krättli M, Cornel J, Mazzoti M, Brozio J. Design and optimization of a combined cooling/antisolvent crystallization process. *Cryst Growth Des*. 2009;9(2):1124-1136. doi:10.1021/cg800934h

59. Holaň J, Skořepová E, Heraud L, et al. Polymorphic Crystallization and Structural Aspects of Agomelatine Metastable Form X Prepared by Combined Antisolvent/Cooling Process. *Org Process Res Dev*. 2016;20(1):33-43. doi:10.1021/acs.oprd.5b00241

60. Zhang D, Xu S, Du S, Wang J, Gong J. Progress of Pharmaceutical Continuous Crystallization. *Engineering*. 2017;3(3):354-364. doi:10.1016/J.ENG.2017.03.023

61. Galan K, Eicke MJ, Elsner MP, Lorenz H, Seidel-Morgenstern A. Continuous preferential crystallization of chiral molecules in single and coupled mixed-suspension mixed-product-removal crystallizers. *Cryst Growth Des*. 2015;15(4):1808-1818. doi:10.1021/cg501854g

62. Pawar N, Agrawal S, Methekar R. Continuous Antisolvent Crystallization of α-Lactose Monohydrate: Impact of Process Parameters, Kinetic Estimation, and Dynamic Analysis. *Org Process Res Dev*. 2019;23(11):2394-2404. doi:10.1021/acs.oprd.9b00301

63. Sultana M, Jensen KF. Microfluidic continuous seeded crystallization:

Extraction of growth kinetics and impact of impurity on morphology. *Cryst Growth Des*. 2012;12(12):6260-6266. doi:10.1021/cg301538y

64. Lawton S, Steele G, Shering P, Zhao L, Laird I, Ni XW. Continuous crystallization of pharmaceuticals using a continuous oscillatory baffled crystallizer. *Org Process Res Dev*. 2009;13(6):1357-1363. doi:10.1021/op900237x

65. Likozar B, Orehek J. Continuous Crystallization Processes in Pharmaceutical Manufacturing : A Review. 2021. doi:10.1021/acs.oprd.0c00398

66. Gong J, Tang W. Nucleation. *Pharm Cryst Sci Eng*. 2018:47-88. doi:10.1002/9781119046233.ch2

67. Sheikholeslamzadeh E, Rohani S. Solubility prediction of pharmaceutical and chemical compounds in pure and mixed solvents using predictive models. *Ind Eng Chem Res*. 2012;51(1):464-473. doi:10.1021/ie201344k

68. Lewis R, Evans W. Solutions and Solubility. *Chemistry (Easton)*. 2018:173-193. doi:10.1057/978-1-137-61037-9_11

69. Mane MB, Shinde SN. Vapor Liquid Equilibria: a Review. *Sci Revs Chem Commun*. 2012;2(2):158-171. www.sadgurupublications.com.

70. De Souza B, Keshavarz L, Steendam RRE, et al. Solubility Measurement and Thermodynamic Modeling of N-(4-Methylphenyl- Z-3-chloro-2-(phenylthio)propenamide in 12 Pure Solvents at Temperatures Ranging from 278.15 to 318.15 K. *J Chem Eng Data*. 2018;63(5):1419-1428. doi:10.1021/acs.jced.7b01011

71. Reus MA, Van Der Heijden AEDM, Ter Horst JH. Solubility Determination from Clear Points upon Solvent Addition. *Org Process Res Dev*. 2015;19(8):1004-1011. doi:10.1021/acs.oprd.5b00156

72. Brittain HG. Vibrational spectroscopic studies of cocrystals and salts. 2. The benzylamine-benzoic acid system. *Cryst Growth Des*. 2009;9(8):3497-3503. doi:10.1021/cg9001972

73. Surov AO, Terekhova I V., Bauer-Brandl A, Perlovich GL. Thermodynamic

and structural aspects of some fenamate molecular crystals. *Cryst Growth Des*. 2009;9(7):3265-3272. doi:10.1021/cg900002q

74. Temperini MLA, Petrilli HM, Constantino VRL. Mefenamic Acid Anti-In fl ammatory Drug: Probing Its Polymorphs by Vibrational (IR and Raman) and Solid-State NMR Spectroscopies. 2014. doi:10.1021/jp500988k

75. Kato F, Otsuka M, Matsuda Y. Kinetic study of the transformation of mefenamic acid polymorphs in various solvents and under high humidity conditions. 2006;321:18-26. doi:10.1016/j.ijpharm.2006.04.020

76. Febra SA, Bernet T, Mack C, et al. Extending the SAFT-γ Mie approach to model benzoic acid, diphenylamine, and mefenamic acid: Solubility prediction and experimental measurement. *Fluid Phase Equilib*. 2021;540:113002. doi:10.1016/j.fluid.2021.113002

77. Granberg RA, Rasmuson ÅC. Solubility of paracetamol in pure solvents. *J Chem Eng Data*. 1999;44(6):1391-1395. doi:10.1021/je990124v

78. Sun H, Gong JB, Wang JK. Solubility of Lovastatin in acetone, methanol, ethanol, ethyl acetate, and butyl acetate between 283 K and 323 K. *J Chem Eng Data*. 2005;50(4):1389-1391. doi:10.1021/je0500781

79. Mudalip SKA, Bakar MRA, Jamal P, Adam F. Prediction of Mefenamic Acid Solubility and Molecular Interaction Energies in Di ff erent Classes of Organic Solvents and Water. *Ind Eng Chem Res*. 2018. doi:10.1021/acs.iecr.8b02722

80. Wan Y, He H, Zhang P, et al. Solid-liquid equilibrium solubility and thermodynamic properties of cis-5-norbornene-endo-2,3-dicarboxylic anhydride in fourteen pure solvents and three binary solvents at various temperatures. *J Mol Liq*. 2020;297:111396. doi:10.1016/j.molliq.2019.111396

81. Shayanfar A, Velaga S, Jouyban A. Fluid Phase Equilibria Solubility of carbamazepine , nicotinamide and carbamazepine – nicotinamide cocrystal in ethanol – water mixtures. *Fluid Phase Equilib*. 2014;363:97-105. doi:10.1016/j.fluid.2013.11.024

82. Elliot JR, Lira CT. Introduction to Multicomponent Systems. In: *Introductory Chemical Engineering Thermodynamics*. ; 2012:369-411.

83. Gothard FA, Codrea Clobanu MF, Breban DG, Bucur CI, Sorescu G V. Predicting the Parameters in the Wilson Equations for Activity Coefficients in Binary Hydrocarbon Systems. *Ind Eng Chem Process Des Dev*. 1976;15(2):333-337. doi:10.1021/i260058a020

84. Hristova M, Donchev T, Kolev D, Baloch I, Georgiev H. Parameter'S Estimate in Wilson Equation. *Int Electron J Pure Appl Math*. 2015;7(3). doi:10.12732/iejpam.v9i1.4

85. Nti-Gyabaah J, Chmielowski R, Chan V, Chiew YC. Solubility of lovastatin in a family of six alcohols: Ethanol, 1-propanol, 1-butanol, 1-pentanol, 1-hexanol, and 1-octanol. *Int J Pharm*. 2008;359(1-2):111-117. doi:10.1016/j.ijpharm.2008.03.046

86. ter Horst JH, Schmidt C, Ulrich J. Fundamentals of Industrial Crystallization. In: *Handbook of Crystal Growth*. ; 2015:1317-1346.

87. Wichianphong N, Charoenchaitrakool M. Journal of Industrial and Engineering Chemistry Statistical optimization for production of mefenamic acid – nicotinamide cocrystals using gas anti-solvent (GAS) process. *J Ind Eng Chem*. 2018;62:375-382. doi:10.1016/j.jiec.2018.01.017

88. Sun H, Wang J. Solubility of lovastatin in acetone + water solvent mixtures. *J Chem Eng Data*. 2008;53(6):1335-1337. doi:10.1021/je800063d

89. Acree WE. Comments on "Solubility and Dissolution Thermodynamic Data of Cefpiramide in Pure Solvents and Binary Solvents." *J Solution Chem*. 2018;47(1):198-200. doi:10.1007/s10953-018-0714-3

90. Pramanik R, Bagchi S. Studies on solvation interaction: Solubility of a betaine dye and a ketocyanine dye in homogeneous and heterogeneous media. *Indian J Chem - Sect A Inorganic, Phys Theor Anal Chem*. 2002;41(8):1580-1587.

91. Ruidiaz MA, Delgado DR, Martínez F, Marcus Y. Solubility and preferential solvation of sulfadiazine in 1,4-dioxane+water solvent mixtures. *Fluid*

Phase Equilib. 2010;299(2):259-265. doi:10.1016/j.fluid.2010.09.027

92. Ter Horst JH, Deij MA, Cains PW. Discovering New Co-Crystals. *Cryst Growth Des*. 2009;9(3):1531-1537.

93. Yoshida MI, Oliveira MA, Gomes ECL, Mussel WN, Castro W V., Soares CD V. Thermal characterization of lovastatin in pharmaceutical formulations. *J Therm Anal Calorim*. 2011;106(3):657-664. doi:10.1007/s10973-011-1510-0

94. Sullivan RA, Davey RJ, Sadiq G, et al. Revealing the roles of desolvation and molecular self-assembly in crystal nucleation from solution: Benzoic and p -aminobenzoic acids. *Cryst Growth Des*. 2014;14(5):2689-2696. doi:10.1021/cg500441g

95. Shayanfar A, Fakhree MAA, Acree WE, Jouyban A. Solubility of lamotrigine, diazepam, and clonazepam in ethanol + water mixtures at 298.15 K. *J Chem Eng Data*. 2009;54(3):1107-1109. doi:10.1021/je8007827

96. Kongsamai P. Seperation of DL-Asparagine Enantiomers Using Crystallization Inhibitors. 2017.

97. Romero S, Escalera B, Bustamante P. Solubility behavior of polymorphs I and II of mefenamic acid in solvent mixtures. 1999;178:193-202.

98. Mack C, Hoffmann J, Sefcik J, ter Horst JH. Phase Diagram Determination and Process Development for Continuous Antisolvent Crystallizations. *Crystals*. 2022;12(8).

99. Black S, Dang L, Liu C, Wei H. On the measurement of solubility. *Org Process Res Dev*. 2013;17(3):486-492. doi:10.1021/op300336n

100. Zhang D, Xu S, Du S, Wang J, Gong J. Progress of Pharmaceutical Continuous Crystallization. *Engineering*. 2017;3(3):354-364. doi:10.1016/J.ENG.2017.03.023

101. Bustamante P, Navarro J, Romero S, Escalera B. Thermodynamic origin of the solubility profile of drugs showing one or two maxima against the polarity of aqueous and nonaqueous mixtures: Niflumic acid and caffeine. *J Pharm Sci*. 2002;91(3):874-883. doi:10.1002/jps.10076

102. Granberg RA, Rasmuson AC. Solubility of paracetamol in binary and ternary mixtures of water plus acetone plus toluene. *J Chem Eng Data*. 2000;45(3):478-483. doi:10.1021/je990272l

103. Pacheco DP, Martínez F. Thermodynamic analysis of the solubility of naproxen in ethanol + water cosolvent mixtures. *Phys Chem Liq*. 2007;45(5):581-595. doi:10.1080/00319100701313862

104. Wang L, Yang W, Song Y, Gu Y. Solubility Measurement, Correlation, and Molecular Interactions of 3-Methyl-6-nitroindazole in Different Neat Solvents and Mixed Solvents from T = 278.15 to 328.15 K. *J Chem Eng Data*. 2019;64(8):3260-3269. doi:10.1021/acs.jced.8b01256

105. Li X, Chen J, Chen G, Zhao H. Solubility modelling, solution thermodynamics and preferential solvation of hymecromone in binary solvent mixtures of: N, N -dimethylformamide + methanol, ethanol or n -propanol. *RSC Adv*. 2017;7(73):46378-46387. doi:10.1039/c7ra07587a

106. Sato S, Hata T, Tsujita Y. The structure of monacolin K, C24H36O5. *Acta Cryst*. 1984;40(1):195-198.

107. Turner TD, Hatcher LE, Wilson CC, Roberts KJ. Habit Modification of the Active Pharmaceutical Ingredient Lovastatin Through a Predictive Solvent Selection Approach. *J Pharm Sci*. 2019;108(5):1779-1787. doi:10.1016/j.xphs.2018.12.012

108. Naik JB, Mokale V. Preparation of Freeze-dried Solid Dispersion Powder using Mannitol to Enhance Solubility of Lovastatin and Development of Sustained Release Tablet Dosage Form. *Columbia Int Publ Am J Pharm Sci Nanotechnol*. 2014;1(1):11-26. doi:10.13140/2.1.4312.5769

109. Mikhail SZ, Kimel WR. Densities and Viscosities of Methanol-Water Mixtures. *J Chem Eng Data*. 1961;6(4):533-537. doi:10.1021/je60011a015

110. Perry RH, Green D. Densities of Aquous Organic Mixtures. In: *Perry's Chemical Engineers Handbook*. 7th ed. ; 1997:109-117. https://www.handymath.com/cgi-bin/isopropanolwghtvoltble5.cgi?submit=Entry.

111. Washburn EW. *International Critical Tables of Numerical Data of Physics, Chemistry, and Technology*. Vol 3. 1st ed. New York; 1930.

112. Thomas KT, McAllister RA. Densities of liquid-acetone-water solutions up to their normal boiling points. *AIChE J*. 1957;3(2):161-164. doi:10.1002/aic.690030206

113. Asghar SZ, Jouyban A, Martinez F, Rahimpour E. Solubility of naproxen in ternary mixtures of {ethanol + propylene glycol + water} at various temperatures: Data correlation and thermodynamic analysis. *J Mol Liq*. 2018;268:517-522. doi:10.1016/j.molliq.2018.07.082

114. Abbott M, Prausnitz J. Modelling the Excess Gibbs Energy. In: *Models for Thermodynamic and Phase Equilibria Calculations*. ; 1994:1-87.

115. Anslyn E, Dougherty D. Binding Forces. In: Murzdek J, ed. *Modern Physical Organic Chemistry*. 1st ed. ; 2006:168-177.

116. Editor G, Mccoustra M, Vendrell O, et al. Water–methanol mixtures: topology of hydrogen bonded network. *Phys Chem Chem Phys*. 2008;(10):5004-5011. doi:10.1039/b812223g

117. Yang B, Cao X, Lang H, Wang S, Sun C. Study on hydrogen bonding network in aqueous methanol solution by Raman spectroscopy. *Spectrochim Acta Part A Mol Biomol Spectrosc*. 2020;225:117488. doi:10.1016/j.saa.2019.117488

118. Valavi M, Svärd M, Rasmuson ÅC. Improving Estimates of the Crystallization Driving Force: Investigation into the Dependence on Temperature and Composition of Activity Coefficients in Solution. *Cryst Growth Des*. 2016;16(12):6951-6960. doi:10.1021/acs.cgd.6b01137

5.9 Supporting information

5.9.1 Raw Solubility Data

5.9.1.1 Methanol-Water

x_{AS} [-]	C [mg/g]	T [°C]
0	54.3	34.2
	72.5	39.8
	87.6	43.6
	112.7	48.7
0.05	50.8	38.6
	68.2	43.8
	90.0	48.9
	107.3	52.6
0.1	32.5	34.6
	50.0	42.1
	61.6	46.2
	79.3	50.5
0.15	19.3	30.5
	35.7	41.6
	48.8	46.8
	64.0	52.4
0.2	25.2	41.0
	41.3	49.1
	54.4	53.6
	20.2	37.5
0.3	11.1	41.3
	14.3	44.8
	18.4	48.3
	28.3	54.4

5.9.1.2 Ethanol-Water

x_{AS} [-]	C [mg/g]	T [°C]
0	31.6	27.1
	45.8	34.9
	62.1	40.8
	74.1	44.8
0.05	32.4	25.5
	44.4	31.1
	54.4	35.0
	73.3	41.2
0.1	31.2	24.6
	42.9	30.1
	53.4	34.1
	72.7	40.0
0.15	26.6	25.4
	39.3	30.3
	45.2	32.6
	60.8	38.4
0.2	30.4	27.7
	46.9	35.5
	62.6	40.9
	69.6	43.3
0.3	24.0	31.8
	34.6	38.0
	42.3	41.5
	57.1	47.0
0.4	20.8	40.5
	29.4	46.4
	42.7	55.2
	53.8	56.1
0.5	15.4	49.3
	25.3	56.3
	35.2	61.0
	50.8	63.8

5.9.1.3 Propanol-Water

x_{AS} [-]	C [mg/g]	T [°C]
0	46.4	35.0
	63.4	41.2
	77.5	45.3
	96.0	49.9
0.05	57.5	31.7
	81.5	39.1
	107.2	44.6
	124.5	48.6
0.1	51.9	26.1
	66.3	30.5
	82.2	34.4
	99.6	39.6
0.15	48.1	24.2
	65.3	29.7
	84.0	34.4
	101.1	39.2
0.2	49.4	25.0
	65.1	30.5
	81.2	35.0
	99.2	39.2
0.3	60.8	33.5
	69.9	36.4
	85.0	40.6
	102.0	44.2
0.4	35.7	30.3
	48.2	35.4
	67.8	42.2
	83.7	47.4
0.5	24.0	32.2
	41.4	41.6
	55.9	47.6
	70.9	52.7
0.6	12.2	31.0
	10.6	28.6
	15.2	35.0
	20.3	40.3

5.9.1.4 IPA-Water

x_{AS} [-]	C [mg/g]	T [°C]
0	38.8	33.6
	57.3	40.9
	71.8	44.3
	95.7	49.0
0.05	53.6	32.0
	72.0	37.5
	93.2	42.3
	113.4	45.6
0.1	64.6	31.8
	83.1	36.6
	98.4	40.0
	118.1	43.6
0.15	62.4	31.2
	81.6	35.8
	97.4	39.6
	116.3	42.6
0.2	40.4	24.1
	49.4	28.0
	61.5	32.6
	80.1	37.4
0.3	36.9	29.0
	51.8	35.6
	59.6	37.7
	76.5	42.8
0.4	56.7	46.3
	66.8	49.1
	88.4	54.4
	90.1	55.0
0.5	45.6	53.6
	54.9	56.5
	64.7	59.3
	78.7	63.2
0.6	43.6	65.3
	54.6	69.0
	65.1	71.4
	30.3	60.0

5.9.1.5 Acetone-Water

	C [mg/g]	T [°C]
0	74.0	22.7
	83.0	26.3
	95.9	30.1
	111.2	33.8
	121.1	36.5
	122.6	36.8
	140.2	40.6
	144.6	41.7
0.05	86.4	20.6
	96.7	23.8
	112.0	27.5
	112.9	28.1
	131.0	31.9
	141.8	34.2
	152.2	36.2
0.1	110.2	27.6
	140.8	34.3
	164.1	38.0
	176.7	40.2
0.15	106.3	30.5
	138.7	36.7
	160.8	40.4
	182.1	43.7
0.2	83.5	30.3
	103.8	35.2
	125.7	39.3
	152.2	43.9
0.3	40.9	28.4
	47.5	31.7
	55.9	34.6
	60.3	36.3
0.4	18.2	29.9
	21.7	32.8
	27.7	36.8
	35.2	41.8
0.5	4.6	35.1
	6.0	41.3

	6.9	43.6
	5.6	39.2

5.9.2 Solvent – Water Densities

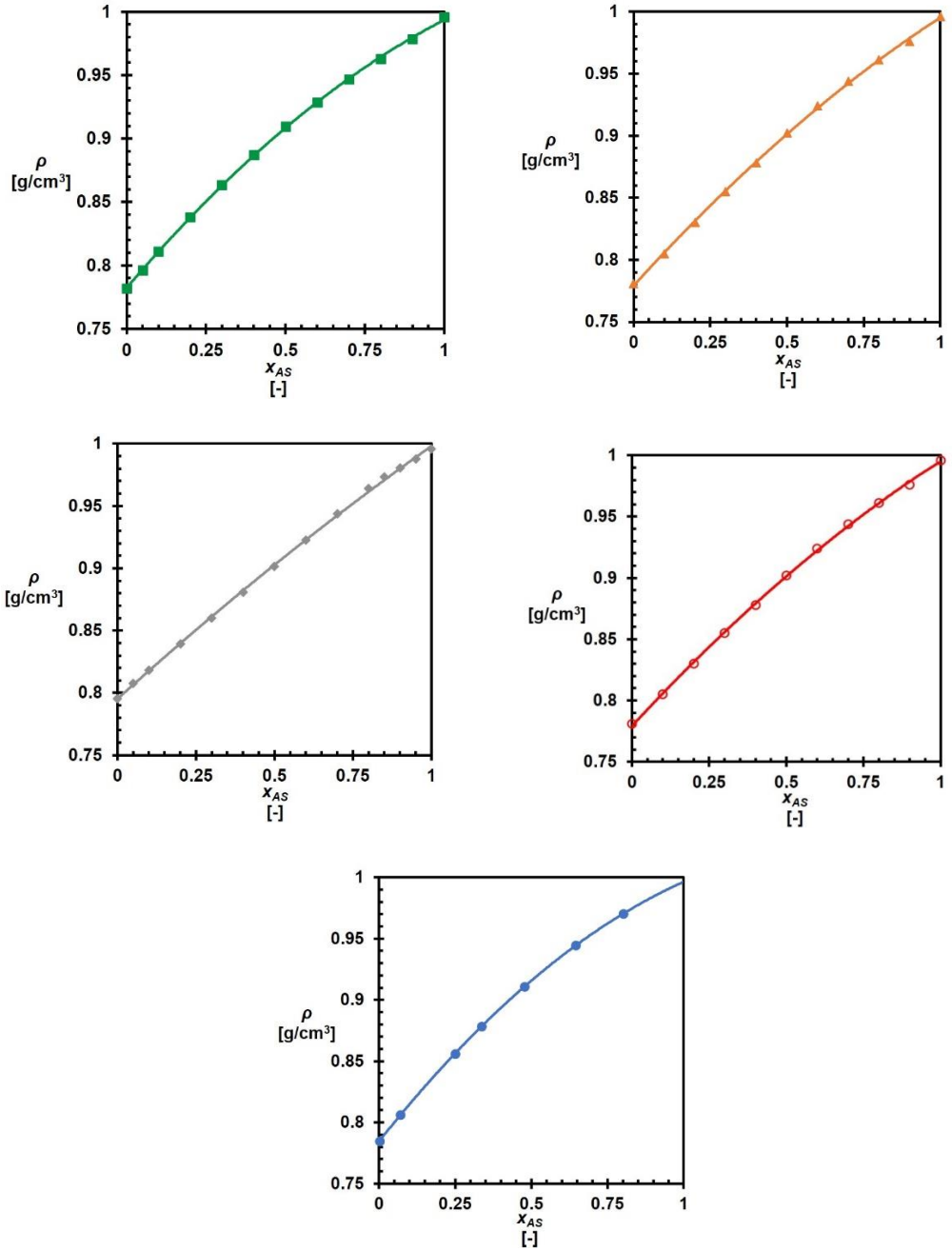

Figure 5-10: The density of solvent-water systems from top to bottom: MeOH (■, 30 °C), EtOH (▲, 30 °C), PrOH (♦, 30 °C), IPA (○, 30 °C) and AcO (●, 25 °C). The markers represent the experimental data with the solid line representing the line of best fit.

The density $\rho_{x_{AS}}$ equations are in the form of Equation 88, with the respective coefficients for each system provided in Table 5-3:

$$\rho_{x_{AS}} = Ax_{AS}^2 + Bx_{AS} + C \qquad 88$$

With x_{AS} representing the mass fraction of the antisolvent (water) .

Table 5-3: Regression coefficients for each solvent water system, along with their respective R^2.

Solvent	*A* [-]	*B* [-]	*C* [-]	R^2
MeOH	-0.082	0.29	0.782	0.99
EtOH	-0.056	0.27	0.779	0.99
PrOH	-0.024	0.23	0.765	0.99
IPA	-0.056	0.27	0.779	0.99
AcO	-0.101	0.31	0.784	1

Chapter 6: Conclusions and Future Work

6.1 Conclusion

This work aimed at developing new approaches to provide a better understanding and optimization of crystallisation processes, with the focus on complex multicomponent systems. From the chapters presented in this work, the key research questions related back to this overarching aim were answered, outlining how best to tackle problems encountered in complex multicomponent systems to improve methodologies.

In Chapter 3, respective activity coefficient measurements for four different model compounds in a number of solvent types were described using semi-empirical models. From these the Wilson model provided the lowest standard deviation compared to the other models used while it also resulted in relevant information on solute-solvent interactions. In a crystallization process design, suitable solubility behaviors could be quantified in specific model parameter quantities, which might aid in the solvent selection procedure by prioritizing different solvent types. From looking at the DSC data required for these regressions, for systems with melting points further away from the measured solubilities, a larger error related to the heat of fusion is expected and so will affect the accuracy of interaction parameters.

Moving into multicomponent systems, Chapter 4 outlined an approach to obtain phase diagrams for antisolvent crystallization using the temperature variation method. The design of a simple empirical equation to model experimental results for various antisolvent crystallization phase diagrams was made which could be fitted to other systems out with those measured due to only solubility data being required. Although depending on the severity of the synergistic relationship, larger errors could be observed. This method was used to identify the most optimal combination of antisolvent fraction and temperature to achieve the best productivity, yield and suspension density within system bounds. This work showed that although continuous antisolvent crystallization is thermodynamically feasible at lower fractions, optimal regions for these types of processes are not achieved until much higher antisolvent fractions.

Chapter 5 combines the observations and techniques observed in previous chapters, as it investigates how well the Wilson equations can be applied to model ternary systems with synergistic relationships. In doing so it also provides an insight into the molecular interactions dictating the development of phase diagram constructions. The inability of the multicomponent Wilson model to model synergistic relationships enabled the approach of considering the solvent-antisolvent as a continuum. From regression of these binary interaction parameters, the λ_{31} parameter shows the biggest influence from the increasing antisolvent content. This parameter shows as the antisolvent fraction changes, the local concentration around the molecule's changes which favors better solubility. The information gained from this approach identifies how antisolvent crystallization processes can be approached in terms of specific solvent-antisolvent combinations to allow optimal configurations.

Overall the main objective of the thesis has been achieved. Utilizing the thermodynamic models for a large solvent screen, we identified how the Wilson model specifically can be utilized to optimize solvent screens. A methodology to better design antisolvent phase diagrams and optimize based on key process parameters was achieved using a small amount of experimental data. Then combining the observations, we outlined a way to better understand how molecular interactions shape phase diagrams and so could allow better optimization for antisolvent selection for crystallization processes.

6.2 Future Work

As with any project, time is a limiting factor and so priorities must be made to ensure key objectives are obtained. Several future pieces of work that could be done to improve the development of design methodologies to compliment the findings presented here are listed:

6.2.1 Model Predictions Versus Reality

From Chapter 4, we devised a model equation and predicted regions of optimization for a continuous antisolvent crystallization. By applying the same methodology to an actual continuous antisolvent crystallisation and comparing the same process characteristics of yield and productivity for both, a true value

of how well the model and design procedure is obtained. Although the method proposed is based on the thermodynamic property of solubility, kinetic properties could impact comparisons.

6.2.2 Relating Crystallization Kinetics to Solution Behaviour

Chapter 5 highlighted how molecular interactions between solute-solvent-antisolvent systems impact antisolvent phase diagrams. Once phase diagrams are obtained crystallisation process can be carried out with a known concentration and so driving force. Determining how well the Wilson molecular interactions parameters can be used for predicting crystallization driving force in a system would be another step towards nucleation prediction. Some previous work by Rasmuson et al. showed that activity coefficient analysis could be used to predict estimates of a crystallisation driving force by neglecting the temperature dependence of the activity coefficient[118]. As the Wilson interaction parameters describe the temperature independent solute-solvent interactions, they could be used to provide a quantitative method for predicting nucleation based on molecular interactions.

6.2.3 Improving the Wilson Multicomponent Equation for API-Solvent-Antisolvent systems

Chapter 5 also highlighted the poor fitting produced from the multicomponent equation. By looking at the excess Gibbs free energy that the Wilson model is built on, an improvement to this model could be investigated to better fit to API-solvent-antisolvent systems. We showed that the interactions between molecules changes the interaction parameter as different amounts of each component is present. This is consistent with a highly non-ideal system. So for there to be a single parameter value as expressed by the multicomponent Wilson model is not possible. This change will look to be incorporated into a model in order to give values at different component fractions to better represent the change in solubility and s describe it better.